PIEZOELECTRIC MULTILAYER BENDING ACTUATED OSCILLOMETRY PROTOTYPE

by

Lucas Posada

Submitted in partial fulfillment of the requirements

for the degree of Master of Applied Science

at

Dalhousie University

Halifax, Nova Scotia

April 2015

Table of Contents

List of Tables

List of Figures

Abstract

Oscillometry (OS), also known as the forced oscillation technique (FOT) is used to measure lung mechanics and can be used to assess airflow obstruction in diseases such as asthma and chronic obstructive pulmonary disease. OS is primarily used in research, but increasingly has found a place in clinical practice. OS applies low amplitude pressure oscillations during normal breathing and it doesn't require challenging respiratory manoeuvres.

Most OS technology is bulky using a loudspeaker, although one uses electromagnetic actuators enabling a smaller accurate device. However, all devices are expensive and together these features significantly slow adoption. To advance the technique and help solve this issue, this thesis presents an innovative method that uses an inexpensive, lightweight beam bending piezoelectric based actuator system potentially greatly reducing costs, and simplifying the mechanical requirements.

Two different versions of the system were developed; a single-actuator and a multi-actuator prototype.

The compact and lightweight single actuator device is presented as the most compelling approach. It applies a single frequency oscillatory pressure at 6 Hz or 19 Hz by moving a mesh-disk of known resistance within a chamber through which the patient also breathes. The prototype measures airflow resistance of test loads (TL) consistently and the signal to noise ratios of the pressure and flow signals were satisfactory compare to a similar FOT available in the market. The similar but larger multi actuator device, developed with the goal of applying FOT with composite frequency oscillations, was able to produce oscillations over a range of frequencies, but exhibited too low signal to noise ratio, due to too great a leak in the gap around the mesh disk. With improvements in design this method could also potentially measure respiratory impedance.

This thesis gave proof of concept and demonstrated the feasibility of using piezoelectric beam bending actuators for the application of the FOT. The single frequency device has the highest potential to be implemented as a clinical diagnostic device, for home use in monitoring applications or included within the breathing circuit during mechanical ventilation. The device has the potential to have an impact in the respiratory market.

List of Abbreviations and Symbols Used

a	Amplitude of oscillation
$\dot{V}$	Flow
$\dot{V}$	Volumetric gas acceleration
®	Registered mark
c	Damping coefficient
c_c	Critical damping
CNC	Computer numerical control
COPD	Chronic obstructive lung disease
CPAP	Continuous positive airway pressure
E	Young's Modulus of Elasticity
Ers	Elastance
F	Force
FEV1	Forced exhaled volume in 1 second
FO	Forced oscillation
FOT	Oscillation technique
FVC	Forced vital capacity
g	Grams
I	Bending moment of inertia

I_{rs}	Inertance
k	Stiffness
kg	Kilogram
L	Length of the cantilever beam
l	Liter
m	Mass
m_a	Mass of the actuator
mm	Millimetres
N	Newton
OS	Oscillometry
P	Pressure
PFT	Pulmonary function tests
P_p	Pressure pneumotach
Q	Quality factor
r	Radius
R	Resistance
r_i	Inner radius
R_{int}	Interrupter Technique Resistance
R_{leak}	Resistance of the leak
R_{mesh}	Resistance of the mesh
r_o	Outer radius

R_p	resistance pneumotach
R_{rs}	Resistance
R_t	Equivalent resistance
s	seconds
SNR	Signal to noise ratio
TL	Test loads
™	Trade mark
V	Volume
x	tip displacement
X_{rs}	Reactance
Z_{rs}	Impedance
γ	Percentage of open area
δ	Decrement ratio
ζ	Damping ration
ξ	Displacement
ω_d	Damped natural frequency
ω_n	Natural frequency

Acknowledgements

My most sincere appreciation to my supervisor Dr. Geoffrey Maksym for his guidance and patience. My special thanks to my committee for their support and advice: Dr. Yuan Ma and Dr. Robert Adamson.

My completion of this thesis could not have been accomplished without the help of my colleagues and good friends Hamed Hanafi, Swati Bhatawadekar, Guy Drapeau and Juan Sebastian Munera.

I would like to thank Thorasys Inc. for providing reference data.

Finally, I wish to thank my parents Dr. Dario Posada and Olga Cecilia Estefan, and my sister Dr. Olga Maria Posada for their constant encouragement and understanding.

This project was funded by the Nova Scotia Lung Association, Natural Science and Engineering Research Council of Canada (NSERC).

CHAPTER 1: INTRODUCTION

1.1. Thesis structure

This thesis is divided into five chapters. Chapter 1 presents a review of background information and explains the principles, context, and purpose of the project including the list of aims and rationales. Chapter 2 describes and explains the design process leading to the construction of two different prototypes created to meet separate FOT requirements and comprise the approaches to reach the aims of the thesis. Chapter 3 contains the testing and validation conducted of the prototypes. Finally, Chapter 4 includes the conclusions, strength and weaknesses of the prototypes, design recommendations, and a statement of contributions.

1.2. Pulmonary physiology and airway mechanics

1.2.1. Respiratory anatomy

The respiratory system consists of the conducting airways, lungs, pulmonary, respiratory muscles, vasculature, and surrounding structures. Each plays a part in the mechanical properties of the respiratory system and influence the process of ventilation, work of breathing and respiratory responses.

Humans have two lungs; the right lung is composed of three divisions called lobes, and the left lung of two as it leaves room for the heart. The lung tissue is

filled with very small gas-filled cavities called alveoli, which are the ultimate structures for gas exchange.

In the process known as ventilation, the air in the atmosphere is transported (in and out) from the oral and nasal cavities to the alveoli through the pharynx, glottal opening, trachea and all remaining conducting airways. At the carina, the trachea divides into the left and right bronchi. The bronchi then subdivide into subbronchi, which subdivide into bronchioli terminating at the alveolar level.

Smooth muscle fibers capable of controlling or pathologically narrowing airway diameter surround the discontinuous cartilaginous segments of the walls of the bronchi, and the smaller non-cartilaginous airways. Smooth muscle is present throughout the respiratory bronchioles and alveolar airways except the last segment which terminates in the alveoli. The alveolar walls are very thin in order to increase efficiency of gas exchange. The number of total alveoli in the human lung falls within the range of 274 to 790 million [1].

1.2.2. Breathing Mechanism

The physiology of breathing involves gas exchange, neurological control and mechanics. The mechanics of the respiratory system determine the work of breathing, and in disease the work of breathing can increase to the point that breathing becomes difficult and therefore gas exchange limited. It is the mechanics of the respiratory system that is assessed by oscillometry (also known as the forced oscillation technique), that is the purpose of the device being developed in this thesis.

This section will describe the mechanics involved in the process of breathing and define the variables involve in it. Breathing is divided into inspiration and expiration. Inspiration takes place during the contraction of the respiratory muscles, while expiration occurs normally as the result of the elastic recoil of the lungs and chest cage, and during exercise, chest wall muscles can aid exhalation through lung compression. The total work in the breathing process can be modelled as comprising three distinct parts: The compliance work to expand the lungs against the elastic forces, the tissue resistance work to overcome the viscosity of the lung and chest wall, and the airway resistance work to overcome airway resistance to movement of air into the lungs. Inertive forces are usually negligible at breathing frequencies, but as we will see are not negligible at frequencies used for FOT.

The mechanics of lung ventilation require understanding the different pressures within the system. The alveolar pressure is the pressure of the air inside the alveoli. This pressure must drop below atmospheric pressure in order to generate inward flow of gas into the alveoli during inspiration. Transpulmonary pressure is the pressure difference between the surface of the lungs and the pressure inside the alveoli. At very slow flows, or with no airflow obstruction caused by narrowed airways, the mechanics of the lung are dominated by the compliance of the lungs which is the ratio between transpulmonary pressure and lung volume. The total compliance of both lungs together in the normal adult human averages about 200 milliliters of air per centimeter of water transpulmonary pressure [2].

1.2.3. The single linear compartment model

Under normal conditions, the mechanics of the respiratory system can be modelled as an elastic balloon at the end of a rigid walled tube. In that model, the pipe would represent the resistive pressure drop and inertial forces from the flow of air through the airways and the balloon would represent the elasticity of the parenchymal tissue, as they are stretched. This is the standard model of the lung and is known as the single-compartment model. The model is described by Equation 1 [3]:

$$P = E_{rs} \cdot V + R_{rs} \cdot \dot{V} + I_{rs} \cdot \ddot{V}$$

Equation 1.

where *P* is the difference in pressure between the airway opening and the pleural surface, *Ers* is the respiratory elastance, *Rrs* is the respiratory resistance *Irs* is the gas inertance, and V is volume, $\dot{V}$ is flow and $\ddot{V}$ is the volumetric gas acceleration.

In the single linear compartment model the respiratory system mechanical properties are characterized by the parameters *Rrs, Ers* and *Irs*. These three parameters can be evaluated and interpreted into physiological terms.

The *Rrs* is mainly determined by flow resistance of the airways (*Raw)* and tissue resistance (*Rt*). *Raw* is considered the combined resistances of the parallel and series resistance of each branch in the airway tree, and is normally the dominant source of airway resistance which increases as airway diameters decrease with constriction [4].

At low frequencies, a frequency dependent portion of the resistance comes from the lung tissues, *Rt* and can also arise from the effects of any heterogeneity in the airways or tissues leading to heterogeneity in flows amongst parallel paths within the lung. *Rt* is both the result of friction between the lung tissue as fibers, cells, and fluids move, and the result of energy dissipation due to uneven flows within the respiratory system. While friction in the tissue can change, this is likely a very modest contribution to disease related changes to lung mechanics while heterogeneity is likely more dominant. [4]. Otis et al. (1956) showed that even in a simple two compartment model of the lung that differences in mechanical properties leads to frequency dependence in resistance arising from the two time constants defined by the resistance and compliance (inverse of elastance) of each compartment [5]. In the more complex multibranch lungs, this leads effectively to a distribution of time constants, and with increased heterogeneity frequency dependence of *Rrs* is increased [6][7].

The *Ers* is a measure of how difficult it is to stretch the lung tissue in order to increase the volume around it. *Ers* is dependent on the lung tissue properties but is dominated by the surface tension of the liquid that covers the alveoli. Since the volume of air in the airways is so much smaller than the volume in the parenchyma, the *Ers* is dominated by the elasticity of the alveoli and the airways are substantially stiffer. The main determinant of *Ers* is the available lung volume for breathing, and trapped gas regions or collapsed regions that are not ventilated reduce lung volume and dramatically increase Ers. Loss of lung volume due to derecruitment of airspaces occurs in asthma or chronic obstructive lung disease (COPD) caused by emphysema described further below, but can also occur with edema, which is fluid filling of alveolar spaces

Ers can also change in pathologies leading to an increase in stiffness of the lung as it happens in pulmonary fibrosis [4].

It is important to note that the mechanics of the lung does not include the mechanics of the chest wall, and depending on the measurement conditions, may not include the upper airways (mouth, cheeks, larynx, etc.), however all contributing together determine the mechanics of the respiratory system.

1.3. Pulmonary diseases

There are many kinds of respiratory diseases. Most diseases of the lung generate changes in the mechanical properties of the lungs and their diagnosis and treatment could be developed from interpreting the airway *Rrs* and *Ers*. Currently changes in I_{rs} are not usually used for interpretation of disease, as the other parameters are considered more sensitive. Respiratory diseases are commonly divided into either obstructive or restrictive diseases. Obstructive diseases are characterized by airflow limitation due to narrowing of the airways or an excess in mucus production. Asthma, COPD and obstructive sleep apnea syndrome (OSAS) are examples of the most common obstructive lung diseases. On the other hand, restrictive respiratory diseases are characterized by a decrease in lung volume (consequently, a decrease in lung compliance) or stiffer lung structure. Pulmonary fibrosis, extrapulmonary restrictive lung diseases and pneumonia are examples of restrictive lung diseases [8].

1.3.1. Asthma

Asthma is a chronic obstructive lung disorder characterized by reversible airway obstruction, airway inflammation and airway hyperresponsiveness (AHR). Some of the symptoms include frequent episodes of wheezing, breathlessness, chest tightness and coughing. It affects more than 235 million around the world and it's the most common chronic di [9]. In Canada, 8.1% of the population over 12 years old has been diagnosed as well as 13% of children from 0 to 11 years old [10][11]. Moreover, as reported by the Canadian lung association, it is the cause of death of approximately 20 children and 500 adults [12].

While asthma cannot be cured, control of the disease can be achieved by regular diagnosis, proper medication, and avoiding the triggers that cause asthma attacks [13].

1.3.2. Chronic Obstructive Pulmonary Disease

Chronic obstructive pulmonary disease (COPD) is a life-threatening lung pathology characterized by a limitation of airflow due to loss of parenchymal tissue elasticity which is commonly under diagnosed. This airflow limitation restricts airflow during forced exhalation, as airways collapse through loss of elastic recoil that keeps the airways open. Thus it can limit exercise, and when severe can limit normal breathing [14].

It was estimated that in 2004 64 million people had COPD and in 2005 more than 3 million people died of COPD around the world [15]. The total deaths from COPD are estimated to keep rising over 30% in the next decade [14]. COPD is mainly caused by inhalation of substances such as tobacco smoke or polluted air and it develops gradually over many years as a significant and chronic inflammatory response to the inhaled irritants [8]. Even though it is not possible to cure, proper diagnosis and treatment can slow the progress of the disease. Importantly, COPD is confirmed (diagnosed) by measuring the mechanical properties of the lungs [16].

1.3.3. Obstructive Sleep Apnea Syndrome

Obstructive sleep apnea syndrome (OSAS) is a disorder characterized by frequent pauses in breathing during sleep usually involving snoring. These pauses stop the oxygen supply causing the brain to briefly wake up the person in order to re-open the airways and breathe again. This sequence can happen many times in the same sleep season, therefore depriving the person of proper rest.

OSAS is diagnosed through pulse oximetry, which measures the oxygen level in the blood over time, and polysomnography, which measures the body movements during sleep. a method of recording body activity during sleep. OSAS, even though not a life-threatening condition, can lead to cardiovascular and cerebrovascular diseases.

One of the treatments to this syndrome is continuous positive airway pressure (CPAP), which forces air into the lungs through a mask. In this method, the CPAP can be continuously adjusted by monitoring the airways resistance. A way of doing so within the same system is by using the forced oscillation technique (FOT). The RESMED® S9 is an example of a device that uses CPAP and FOT to treat OSAS [17].

1.4. Pulmonary function testing & diagnosis

Pulmonary function tests (PFT's) provide an objective measure of the capability of the respiratory system to ventilate its lungs. Some of these tests are:

1.4.1. Spirometry

Spirometry is currently the gold standard for measuring pulmonary function [3]. The device used to perform this method, the spirometer, measures airflow during different manoeuvres the subjects must perform. The most common of the various measurements taken with spirometer are the forced exhaled volume in 1 second (FEV1) and forced vital capacity (FVC). FVC is the total volume of gas that can be expired after maximal inspiration. The procedure to measure FVC and FEV1 requires the subject to inhale to total lung capacity and exhale as fast as possible. FEV1 and FEV1 normalized by FVC are used to determine airway obstruction. In healthy adult subjects a ratio for FEV/FVC greater than 80% is defined to be the threshold for normal [18]. The values measured from spirometry are compared to published standardized values based on age,

height, gender and ethnicity to produce relative percent predicted values for aid in diagnosing and monitoring disease [3].

A commonly implemented test used when diagnosing or monitoring asthma (but can also be used in COPD or complex patients) involves the use of a short acting B2 agonist to induce the dilation of the airways before measuring FEV1 in order to determine the reversibility of airway obstruction. An increase in FEV1 greater than 12% from baseline is considered as a significant reversible airway obstruction, and is an indication of asthma [18].

Spirometry requires the subject to be trained and coached in order to perform the test manoeuvres successfully. Therefore, the results of the tests are highly dependent on the subjects performance, and can vary due to subject effort and cooperation, and the technician's (coach) experience and skill [3].

1.4.2. Exhaled Nitric Oxide

Nitric Oxide (NO) is recognized as a biological mediator in animals and humans [19][20]. It is produced by the human lung and it is present in the exhaled breath and it works as a mediator for vasodilatation, bronchodilation and inflammation as well as being a neurotransmitter [21].

NO has been found to be implicated in the pathophysiology of lung diseases, including diseases like asthma [22]. Subjects with asthma show higher levels of NO in their exhaled breath suggesting NO's linkage to asthma pathogenesis [23]. It can also be considered as an indirect marker of airway inflammation [24].

NO measurement technology has become highly developed over the last two decades. Since 1991, the use of chemiluminescence analyzers allowed for the detection of NO [25]. After that, the evaluation of FENO grew as a potential non-invasive method to monitor the response to pulmonary anti-inflammatory therapy as well as the diagnosis of asthma While the equipment has advanced, and even became standardized, its use as a clinically useful tool is still developing [26].

Compared to spirometry for the diagnosis of asthma, the measurement of NO offers several advantages such as the non-invasive nature of the test, the repeatability of the measurements, and the ease of use for the subject, but its utility is still being assessed [24].

1.4.3. The Interrupter Technique

The interrupter resistance technique is a non-invasive measure of respiratory resistance during tidal breathing first described in 1927 [27]. This method can be easier to perform than spirometry since it requires very little cooperation from the patient [28]. The technique consists on briefly occluding the airway opening for periods of less than 100 milliseconds. Resistance (Rint) is then calculated from the ratio of pressure change to flow at the airway opening before to after the occlusion. This technique works under the assumptions that the occlusion occurs rapidly and that the pressure change at the airway opening matches the pressure changes within the alveoli, as flow is stopped, and the time is too short for pressure to be influenced by respiratory efforts from the patient.

This technique has been used in many studies, especially in children and older subjects. Studies have found that it is feasible and clinically usefulness in preschool children with bronchopulmonary dysplasia [29][30]. One study found correlation between Rint and other lung function indices like FEV1 [31]. On the other hand, it has showed poor performance in older patients [32].

This technique is able to detect changes in airway caliber. However, evidence to support its clinical practice is needed as well as overcoming technical (hardware) challenges [28].

1.4.4. Forced Oscillation Technique (FOT)

The FOT is a non-invasive method for characterizing respiratory mechanics that was introduced by Dubois et al. in 1956 [33]. The technique consists in superimposing low amplitude pressure oscillations on the subject's spontaneous breathing and, at the same time, record flow (V) and pressure (P) at the airway opening. With the recorded information, the respiratory system impedance (*Zrs*) can be calculated at the determined forced oscillation (FO) frequency by taking the ratio of Fourier transforms of P and V.

$$Z(f) = P(f)/(\dot{V}(f))$$

Equation 2

Zrs represents the mechanical load that the resistive, elastic and inertial components of respiratory system apply over the forced oscillatory flow. *Zrs* is a complex quantity where the real part indicates the resistance (*Rrs*) and the imaginary part indicates the reactance (*Xrs*).

Zrs, can also be described in the Cartesian coordinates as:

$$Zrs(f) = Rrs(f) + jXrs(f)$$

Equation 3

where $j = \sqrt{-1}$. Xrs is the measure of the elastic and inertial properties and if fit to the standard linear model of the respiratory system (Equation 1) can be expressed as:

$$Xrs(f) = 2\pi f I_{rs} - E_{rs}/2\pi f$$

Equation 4

In order to obtain more information about the condition of the respiratory system of patients, and in the case of the standard linear model to identify estimates of *Rrs*, *Ers*, and *Irs*, FOs are preferably used over a range of frequencies rather than just one. However, the impedance can differ from the standard linear model and demonstrate interesting frequency dependence. This is because the lung mechanics arise from a complex structure with distributed and possibly time varying time constants. Distributed time constants leads to a frequency response that can be correlated to the physiology of the respiratory system. Figure 1 shows the typical behaviour of resistance and reactance over a range of frequencies in a healthy subject and an ill patient (with COPD):

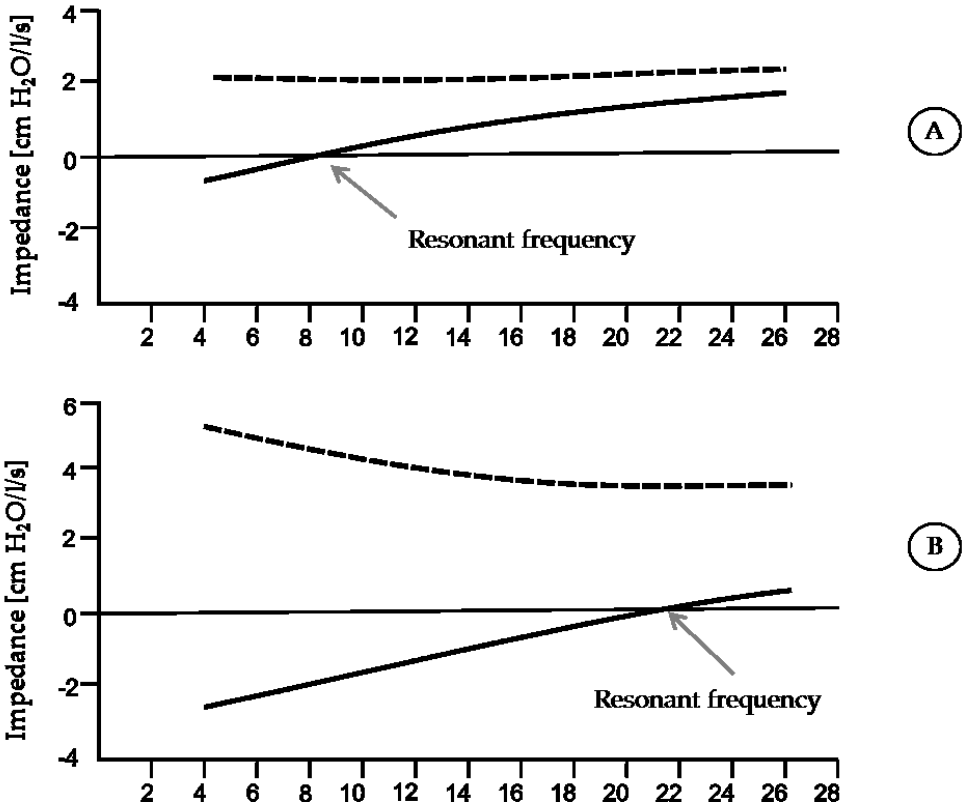

Figure 1. Typical resistance and reactance frequency response in a normal subject (A) and a patient with COPD (B). Dotted lines represent Resistance and solid lines represent Reactance. Graph adapted from Pride et al [34].

As the figure shows, *Rrs* in health is largely independent of frequency, although a very slight upward trend is normal. On the other hand, *Rrs* from the patient with a COD shows a negative frequency dependence attributed mainly to inhomogeneities of the lungs as described above. Xrs is dominated by lung stiffness at low frequencies as inertia is negligible, and is often approximated as:

$$Ers = 2\pi fXrs$$

Equation 5

The shift upwards in *Xrs* (Figure 1 B) leading to an increase in *Ers,* is thought to be caused by constricted or closed peripheral airways [33]. The shift upwards also causes a shift rightwards in the resonant frequency when Zrs crosses the axis. At the resonant frequency, elastic forces balance the inertive forces and impedance is only determined by the resistance.

The FOT, although it is still not widely used, has been applied successfully in many studies. For example, it has been validated for tracking changes in respiratory mechanics during mechanical ventilation [35], chronic obstructive pulmonary disease (COPD) [36][37], sleep studies [38][39] and for the study of airway response to bronchomotor drugs for the diagnosis and monitoring of asthma [40][41][42][24].

FOT compared to Spirometry

The FOT is as non-invasive as the measurement of exhaled gases such as nitric oxide and can be used as a diagnostic tool in subjects who cannot perform spirometry [13]. In contrast to spirometry, FOT can be reliably used in the assessment of children less than 6 years old, elderly, paralysed, unconscious or mechanically ventilated patients. Moreover, it doesn't require deep inspirations, which can be effort dependent, and it also known that the stretch on the airways can alter airway smooth muscle tone, affecting the measurement of spirometry [43].

Additionally, when performing airway hyperresponsive (AHR) testing, which uses increasing doses of a bronchoconstrictors such as methacholine until a 20% decrease in FEV1 is achieved, it has been shown that subjects require lower concentrations of methacholine and histamine to elicit a clinically useful response as opposed to the traditional forced expiratory manoeuvres needed with spirometry [44]. The FOT also doesn't require significant training of the subject by the respiratory technologist and less time is typically needed to perform a measurement, which can ultimately lead to reduced health care expenses.

1.5. FOT Devices

Depending on its design, each type of FOT device is capable of generating a characteristic oscillation signal. These external forcing signals can be mono-frequency or multi-frequency, and can also be applied either continuously or impulse. Most FOT devices make use of a loudspeaker to generate the oscillations at the airway opening and measure the relation of pressure-flow at the airway opening [34][37][39]; this measurement configuration measures the respiratory system input impedance. Their typical schematic arrangement is shown in Figure 2.

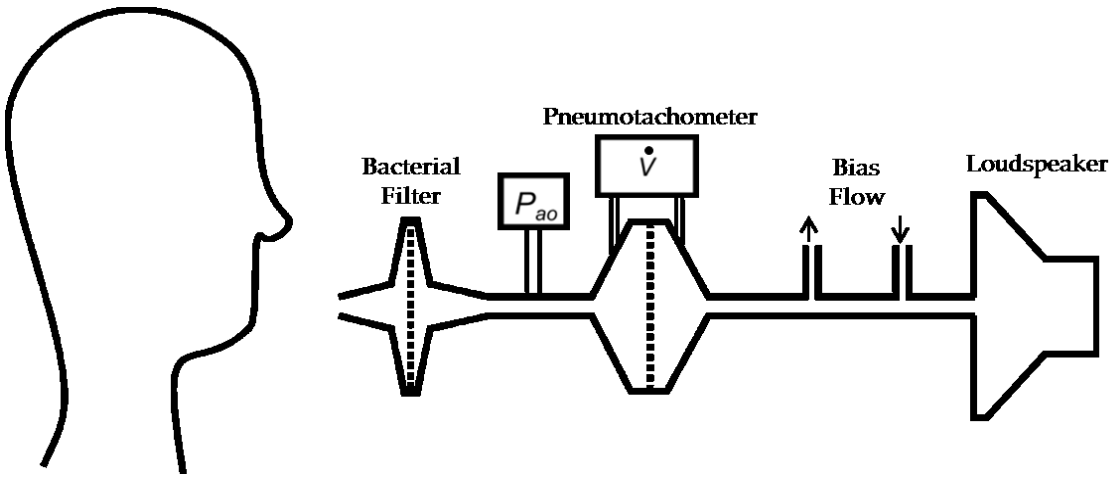

Figure 2. Typical schematic arrangement of FOT device. Where $\dot{V}$ volume rate and *Pao* is pressure at airway opening.

An alternative technique applies an oscillatory pressure signal to the airway opening and measures the motion of the chest wall, obtaining transfer impedance of the respiratory system. This can be reversed, and oscillations can be applied to the chest wall and measure the relation pressure-flow at the airway opening [45]. This kind of devices requires large chambers to fit the upper body of the subject.

Many FOT devices used in research studies are developed and incorporated with a mechanical ventilator or respiratory support system [46][47][48]. There are other devices that have proven the potential use of FOT in home monitoring and telemedicine in portable form [49][50].

1.5.1. Commercially available

There are only a handful of FOT devices currently available in the market including the MasterScreen-IOS device from CareFusion [51], the MostGraph-01 from Chest [52], Quark PFT from Cosmed [53], and the tremoFlo which is the only hand-held portable device.

The tremoFlo®

Since my thesis is to develop novel technologies for handheld FOT, I will describe the features of the tremoFlo in more detail:

The tremoFlo Airwave Oscillometry System is a portable lung function-testing device developed by Thorasys Inc. with the collaboration of Dr. Geoffrey N. Maksym. The tremoFlo is used to assess human lung disease such as asthma and COPD in adults and children. In order to do so, the tremoFlo uses the FOT to assess lung function during normal breathing.

Figure 3. The TremoFlo device.

The system comprises a handheld device attached to a cradle unit (Figure 3). Patients breathe directly into the handheld during measurements via a disposable anti-bacterial/viral filter. As the handheld can be moved, it allows for measurements in standing, seated or supine patients. A short calibration is required on a daily basis and test data are captured with measures of quiet breathing.

The TremoFlo uses the patented method (patent CA2613547A1) to apply the FOT that allows the patient to breathe through a moving mesh that produces the oscillation. The prototypes created for this thesis are also based on this method of oscillation generation and therefore the systems performance can be compared. Parameters such as signal to noise ratio (SNR) and impedance measurements acquired with the tremoFlo were used as a reference during the performance testing of the prototypes on Chapter 3.

1.6. Standards and Recommendations for FOT devices

1.6.1. Oscillation frequencies

For clinical applications of FOT it is usual to apply a frequency range that starts as low as 2–5 Hz, about 10 times higher than the spontaneous breathing rate, to an upper frequency sometimes as low as 11 Hz, but more commonly in the range of 30-40 Hz. However both single-frequency and composite signals are used in clinical practice, with single frequency devices operated near 5 or 6 Hz. As more detailed respiratory diagnostic information can be obtained from the simultaneous application of several frequencies at the same time, composite

signals are preferred by researchers. Therefore, the ability of delivering multiple component signals is highly important as a characteristic of the device [43].

1.6.2. Resistance to air flow and pressure

The FOT device should be able to impose a load against spontaneous breathing of less than 1.02 $cmH_2O/L/s$ below 5 Hz. The reason for the limit of 1.02 cmH20/L/s is the guideline document originally specifies the limit in hPa/L/s. When using composite signals, the moving mesh should develop a peak-to-peak pressure variation of 2 cmH_2O at the airway opening. The largest pressure developed in the system shouldn't exceed 5 cmH_2O [43].

1.6.3. Transducers

The pressure transducers and the connecting tubing to the pneumotachometer should be symmetrical and of low compliance, providing a common mode rejection ratio of at least 40 dB at 30 Hz [54], or preferably, 60 dB up to the highest frequency used [43]. The pneumotachometer and the pressure transducers should be linear within 2% up to 1 L/sec and 5.09 cmH2O respectively [43].

1.6.4. Room for improvement

One critical problem for adoption of FOT clinically may be that the current FOT devices available in market are large and expensive. Implementing another, more compact and lighter, method to generate the oscillations would make it possible to produce a device with a similar weight and cost as a portable hand

held spirometer which would be a revolutionary advance in FOT technology. The approach proposed in this thesis, as will be further explained in section 1.8, attempts to bring these features by the use of a novel application of piezoelectric actuator technology.

1.7. Piezoelectric actuators

Piezoelectric actuators use the inverse piezoelectric effect. This effect consists of the expansion and compression of the material by applying an external electric field to the piezoelectric material.

Important advances have been made in piezoelectric actuation architectures in the last 2 decades. Piezoelectric actuators are smart material actuators with high mechanical energy density. Such smart material actuators can have up to 1000 times more deliverable mechanical work per unit volume (energy change) and 10 times as much energy per mass compared to other type of actuators such electromagnetic motors [55]. However, as with other smart materials, piezoelectric actuators have limitations regarding their mechanical displacement, force, and frequency response.

Among smart materials, the piezoelectrics are a very good option for applications involving high speeds and high oscillation frequencies. However, the achievable strains in response to an applied electric field are on the order of 0.1 % to 0.2% [56]. Considering that these strains are so small, improvements are a topic of continuous research. An example of a successful advance in this area are the relaxor ferroelectric single crystals (PZN-PT and PMN-PT) which

can develop strains greater than 1 % and have up to 5 times more strain energy density as conventional piezoceramics (lead zirconate titanate [PZT])[56].

Another focus of research for piezoelectric actuators is in the amplification of displacement. This area is of particular interest for this thesis since displacement amplification is needed in order to achieve aim 2.

Numerous concepts have been developed for the purpose of displacement amplification. The leading architectures to overcome the stroke limitation can be categorized into externally leveraged, internally leveraged, or frequency leveraged.

1.7.1. Internally leveraged actuators

1.7.1.1. Stacks

This most simple form of amplification consists of piezo-ceramic sections stacked linearly to increase their total deflection. The displacement and force of a stack actuator are linearly proportional to the length and cross-sectional area of the sections stacked.

1.7.1.2. Bender Actuators

This architecture uses the internal piezoelectric strain to induce the actuator motion. Benders consist of one or more layers of piezoelectric material that are poled and activated so that the layers on opposite sides of the neutral axis generate opposite strain. This difference in strain from one side to the other of the neutral axis creates the internal bending moment that causes the actuator to flex. This method results in a quadratic amplification of displacement [57].

One case of bender actuator architecture is known as unimorph or monomorph. A monomorph piezoelectric actuator is made of one active piezoceramic layer and one passive elastic layer (Figure 4). The movement of the piezoceramic component resulting from its expansion or compression is restricted by the passive elastic layer. As a consequence, an internal piezoelectric moment arises deforming (curving) the monomorph. The total deflection in z direction is much larger than the internal x direction strain even at low voltages [58].

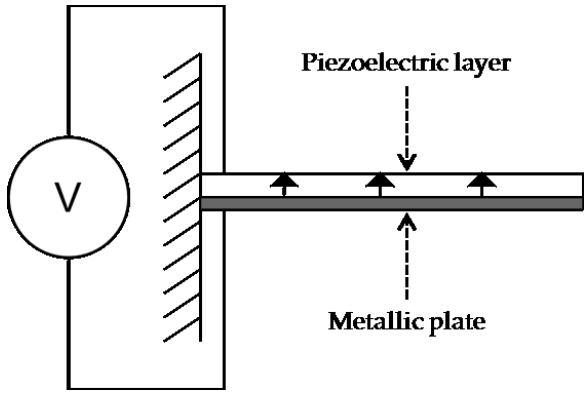

Figure 4. Monomorph piezoelectric actuator structure. The arrows in the piezoelectric layer point towards the direction of the polarization.

In order to increase the deflection of the beam bending actuator, the passive elastic component can be replaced by a second active piezoceramic layer to create what is called a bimorph piezoelectric actuator (BPA). In a BPA, deflections are larger, but forces are lower, compared to the forces developed by stack piezoelectric actuators [58]. BPA's are simple, low-cost and are available off the shelf and indeed as will be described, this type of actuator was the design chosen in this thesis.

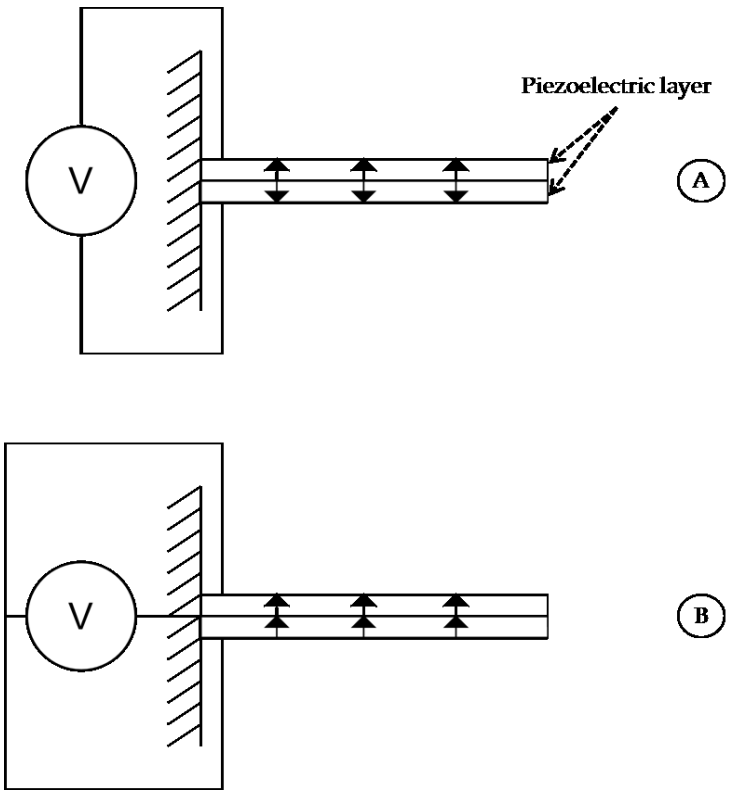

Figure 5. Bimorph structure. A) Series drive, B) Parallel drive. Arrows in the piezoelectric layer point towards the direction of the polarization

Another type of internally levered actuators is the building-block actuators. In this architecture, numerous small actuation units (or building blocks) are attached together in series, much like the stack actuators, and/or in parallel to form a larger actuation system. An example of this scheme is the C-block actuators (Figure 6.).

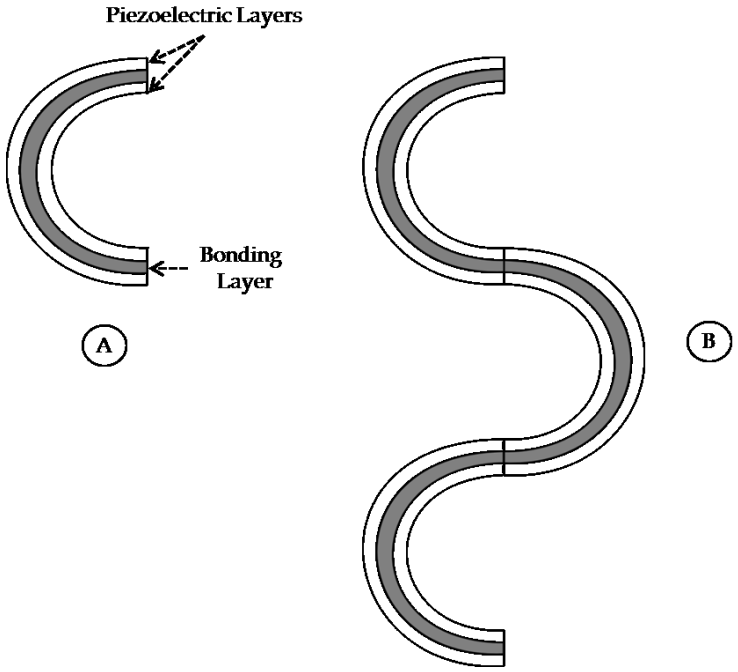

Figure 6. Simple C-block actuator structure. A) Single unit or building block. B) Array connected in series.

The C-block type of actuator can produce 8% more work than an equivalent straight bender [59], although they can't bend as much as the bimorph type of bending actuators.

1.7.2. Externally Leveraged Actuators

Externally leveraged actuators, as their name indicates, use an external mechanism to produce an amplified deflection but sacrifice force output. New methods of displacement amplification are in constant development as there can be many approaches that make use mechanic, hydraulic, or other kinematic systems. Some of the most common are lever arm actuators, hydraulic amplified actuators, and flextensional actuators. Lever arm actuators use a

mechanical lever arm. The mechanism increases the displacement output and it is inversely proportional to the force output [60]. An example of this kind of architecture used in the aerospace industry can be seen in Figure 7.

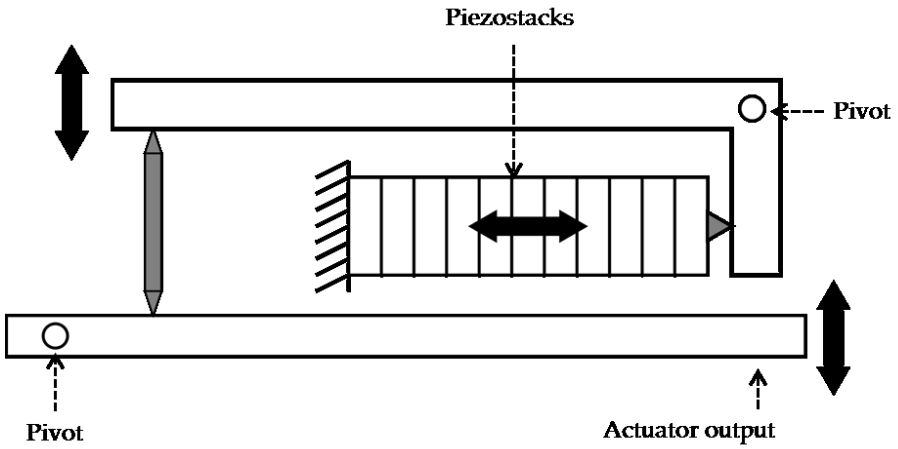

Figure 7. L–L amplification mechanism. Adapted from Lee et al. [61]

For the actuators using hydraulic amplification, the most common system consists of a piezoceramic stack, a piston, and hydraulic fluid. The transmission ratios are up to 100 in these kind of systems using hydraulic amplifiers [62]. An example can be seen in Figure 8.

Figure 8. Basic design of a hydraulic amplified actuator.

The flextensional type of actuators uses a piezoceramic stack and an external mechanism to amplify the displacement in the transversal direction. An example of this approach is the Moonie piezoelectric transducer (Figure 9).

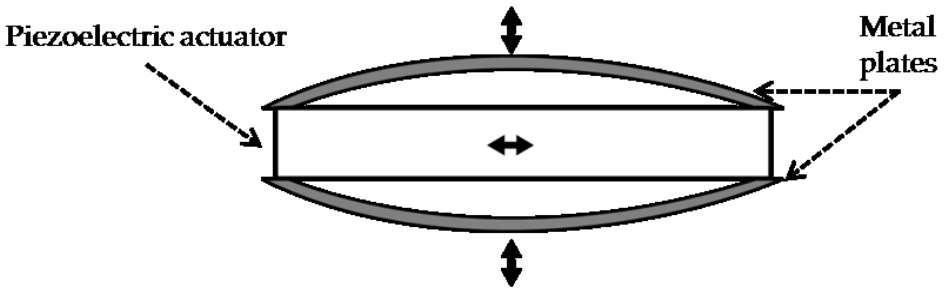

Figure 9. Cross-sectional view of a Moonie transducer. Adapted from Onitsuka et al. [63].

1.7.3. Frequency-Leveraged Actuators

A different approach to achieve amplified motion is to use frequency leveraged amplification. This increases the potential strain output of the actuator by using the rapid vibrations of the piezoelectric material to translate the actuator in one direction along a rod or stationary part as if taking small steps. The first actuator of this type developed and patented is the Inchworm, by Burleigh Instruments [64]. In this actuator, three piezo-ceramic sections (leading, extending and trailing sections as seen in Figure 10) contract and expand in specific sequences to create the small stepping movement.

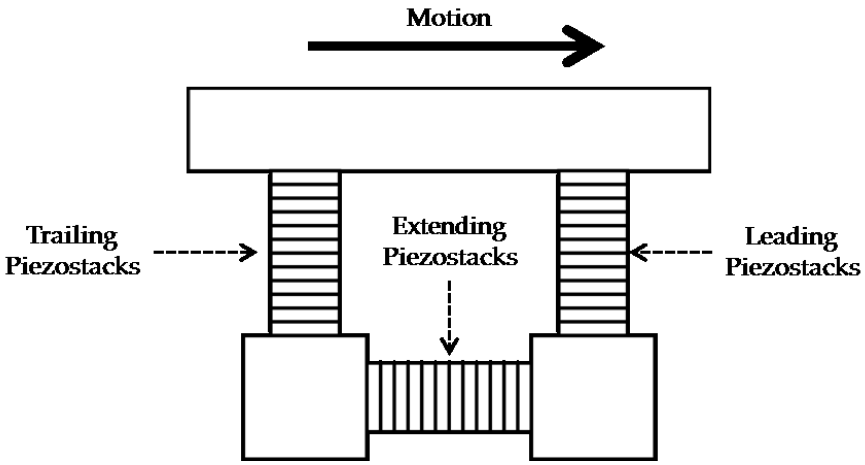

Figure 10. Inchworm actuator. Adapted from Niezrecki et al. [64].

These examples comprise just a few ways of how piezoelectric actuators can be used in combination to achieve differing mechanical objectives.

1.8. Thesis Aims

The general hypothesis being explored in this thesis is that piezoelectric transducers can be implemented in a prototype FOT device and achieve performance set out by current guidelines. The thesis focuses on the kinematic analysis and mechanical design of this concept and the scope doesn't include electronics design (and construction) for the prototypes developed.

The aim of this project consists of two main objectives explained as follows.

One of the objectives is low-cost, which is best achieved with as simple as possible a design. To achieve this, it may be reasonable to operate a single bimorph actuator at resonance, where the largest displacements at the lowest power can be achieved. This is explored in Aim 1. However this is not

appropriate for achieving a wide range of frequencies which most research and commercial devices achieve, thus this thesis will also consider the design for a multi-frequency actuator in aim 2.

1.8.1. Aim 1

Aim 1 is to develop a simple, single frequency, and thus potentially cost-effective design for a forced oscillation device using piezoelectric actuators compliant with the guidelines for FOT devices and test its performance. This aim includes the assessment of the performance of the piezoelectric actuators chosen for the use in the actuator unit (motor) of the prototype designs. It also includes determining design components such as the mechanism to deliver the oscillations.

Rationale

Piezoelectric actuators are economical in large quantities and can deliver large displacements in appropriate configurations. Taking advantage of that fact, the development of a piezoelectric actuated device has the potential for reduced costs, perhaps comparable to spirometers thus making the FOT more accessible and to become more widely used in clinical practice. While a single frequency device cannot compute impedance over a range of frequencies, it can have a high signal-to-noise ratio, benefiting from concentrating all its power at a single frequency, and thus may be able to better track temporal impedance changes over time, which may be clinically useful. The question to answer here is if the concept of a simple, resonant piezoelectric actuated device is capable of performing FOT reliably and repeatably.

1.8.2. Aim 2

Aim 2 is to develop a design for another forced oscillation device capable of applying multi-frequency oscillations capable of achieving current FOT recommendations and to test its performance.

Rationale

More detailed respiratory diagnostic information can be obtained from the simultaneous application of several frequencies at the same time. Therefore, the ability of delivering multiple component signals is potentially very important as a characteristic of the device.

Like in aim 1, the questions to be answer with this aim is whether the designed prototype is able to perform FOT with acceptable results that meet FOT guidelines or not.

CHAPTER 2: PROTOTYPE DESIGN & CONSTRUCTION

2.1. Introduction

This chapter offers the description of the design and development of the prototypes to test the hypothesis and achieve the aims of the thesis.

Some of the design decisions such the type of actuators to use are based on the initial background research and low cost objective. Other design choices required calculations and testing in order to follow the recommendations for FOT described in section 1.6.

Three prototypes were made. The first one was very basic, and was made as part of the performance evaluation of the piezoelectric actuators. Another one, the single frequency, single bimorph actuated device, was designed aiming for the minimum possible components and cost, and the last one, the multi-actuated device, was designed aiming for the ability to provide multi-frequency information and thus provide more information simultaneously.

2.2. The moving mesh

The concept of using a moving mesh to deliver the oscillations for the FOT is an important improvement over the more standard FOT device (presented in section 1.5). The moving mesh performs the function of the loud speaker at the same time allowing the patient to breathe through it. This feature greatly reduces the dead space of the device, eliminates the need for a bias flow to provide fresh air, and allows the overall form factor of the device to be much

more compact. This concept is used by the tremoFlo as mentioned in section 1.5.1.

2.3. The piezoelectric actuators

The main challenge regarding the piezoelectric actuators used for this application is to deliver the large displacement necessary for the motion of the moving mesh and apply the FOT. The actuators chosen for the application are BPA clamped on one end. This type of actuators offers the highest deflection to size (and weight) ratio.

Initially, since the length of bending actuators is proportional to their tip displacement, attempts to manufacture long, custom made BPAs in the lab were made. However it proved to be too expensive. The piezoelectric ceramic sheets of large size were very expensive in small quantities, and also very fragile, breaking easily while handling, leading to higher cost. While this problem may be solved by providing a suitably flexible but supportive elastic backing layer to adhere to the fragile piezoelectric for strength, I chose to work with readily available off-the-shelf actuators with backing layers already affixed to the piezoelectric material for the purposes of the prototype. If the concept proved workable with these, then perhaps the future design could use custom piezoelectric actuators, which in volume may be an inexpensive approach.

The off-the-shelf BPA with the longest available active length and low cost (available in the market at the time) were the stripe actuators #40-2010 from APC International.

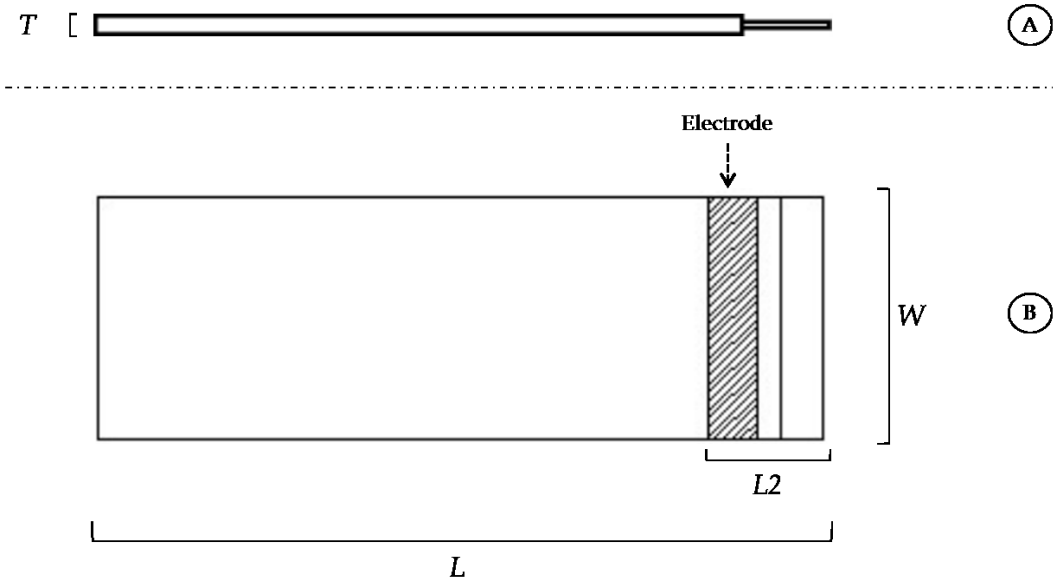

Figure 11. Strip actuator. A) Side view B) Front view.

The actuator dimensions were L = 60mm, W = 20mm and T = 0.70mm, with a manufacturer reported deflection (without mass at the tip) of 2.6 mm at 150 DC Volts with a blocking force of 0.5 N. In the case of AC, the maximum voltage recommended by the manufacturer was 50 Volts peak-to-peak. These actuators can be connected in a parallel electrical configuration, as in Figure 5 (B), that ensures high sensitivity to input drive and helps prolong the life of the actuator by eliminating the potential for depolarizing the ceramic layers as it uses a bias voltage circuitry [65].

2.3.1. Assessing the performance of a single actuator

From the bimorph structure depicted in Figure 5 it can be observed that one approach to model the dynamics of the actuator is the cantilever beam clamped

on one end (with and without mass at the free end) which can be applied to describe the strip actuator of Figure 11. This is a commonly described system in vibration engineering and can be approached as a translational vibrational system instead of a rotational vibrational system (where the beam is translating rather than rotating). This approach is an accurate approximation for small angles.

In order to use piezoelectric actuators in a design for an FOT device I needed to understand and verify its oscillatory amplitude response over the frequency range of oscillation with different applied mechanical loads at the tip. The characterization of the static and dynamic properties of a single beam bending actuator, most importantly its frequency response, provides helpful information for the development of the prototypes. I first consider using theory developed for static deflection of a beam clamped at one end, assuming massless beams, to estimate the beam stiffness. I will show that this is insufficient, and that it is necessary to use the stiffness obtained from the dynamic mechanical system that for the oscillating motion of the beam that considers the distributed mass of the beam and accounts for the rotational inertia of the beam and mass at the tip, which proves to adequately describe the dynamic mechanics of the system.

Figure 12 shows the graphical representation of the clamped on one end beam model of the actuator.

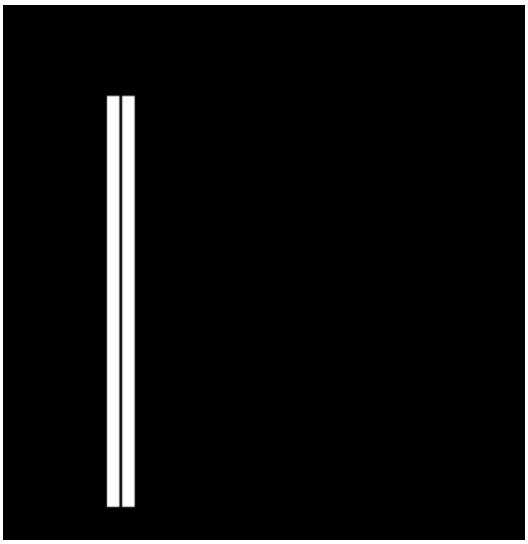

Figure 12. One end clamped cantilever beam. On the left the mechanical schematic, on the right the shape of the first mode - natural frequency.

The deflection, x, by a constant force at the tip of a massless cantilever beam approximating the motion as translational at the tip is given in as [66]:

$$x = \frac{FL^3}{3EI}$$

Equation 6

where x is the tip displacement, F is the applied load, L is the length of the cantilever beam, E is the Young's Modulus of Elasticity, and I the bending moment of inertia.

The stiffness and the deflection at the tip of the cantilever beam can also be expressed as:

$$k = \frac{3EI}{L^3}$$

Equation 7

$$F = kx$$

Equation 8

However, the stiffness of piezoelectric actuators is dependent on many factors due to the non-ideal nature of the piezoelectric material. It varies during static, dynamic, large-signal or small-signal operation and with open or connected electrodes. The piezo ceramics also produce an electrical response when mechanically stressed. In the case when the electrodes are not connected, for instance, the electric charge is not drained and the material generates a counterforce opposing the mechanical stress making it appear stiffer [67].

To investigate this effect, the stiffness of the actuators was measured quasi-statically and dynamically (from the resonance frequency).

A cantilever deflection versus force at the tip test (quasi-static test) was performed as in Figure 13 with the actuator's electrodes open (disconnected). Taking the displacement measured, the acceleration of gravity at sea level (g = 9.80665 m/s2 +/-0.00001 [68]), the concentrated mass of the actuator at its tip (1/4 of the actuator total mass [58]) and the mass hanging at the tip, calculations to find the stiffness were made using Equation 8.

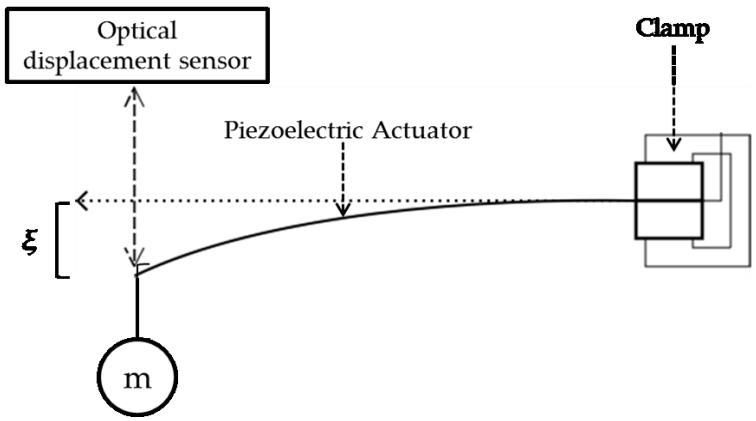

Figure 13. Deflection test. m is the mass hanging at the tip and ξ is the displacement.

This test was performed 3 times and the average results are shown in Table 1. The uncertainties come from the equipment specifications and, in the case of the calculated force and stiffness, and were obtained following the basic rules for the calculation of uncertainty [69].

Table 1. Quasi-static tests results

Parameter	Value	Uncertainty
Mass actuator m_a [g]	4.8	+/- 0.1
Mass at tip [g]	21.0	+/- 0.1
Total mass at the tip [g]	22.2	+/- 0.2
Force calculated [N]	0.217	+/- 0.7%
Displacement ξ [mm]	0.307	+/- 0.015
Stiffness k [N/m]	709.1	+/- 5.6%

Tests of continuous beam vibration frequency versus displacement at the tip of the cantilever were also performed as shown in Figure 14. The tests were performed on 2 different actuators and 3 times on each one. A small piece of white plastic (m = 2.5g) was placed at the tip of the actuators for improving the measurements with the displacement sensor.

In these tests the actuator was stimulated by sinusoidal waveforms at different frequencies, from 5 Hz to 100 Hz, for 5 seconds each time. The sinusoidal waveforms were generated by a function generator and then amplified to 50 volts peak to peak.

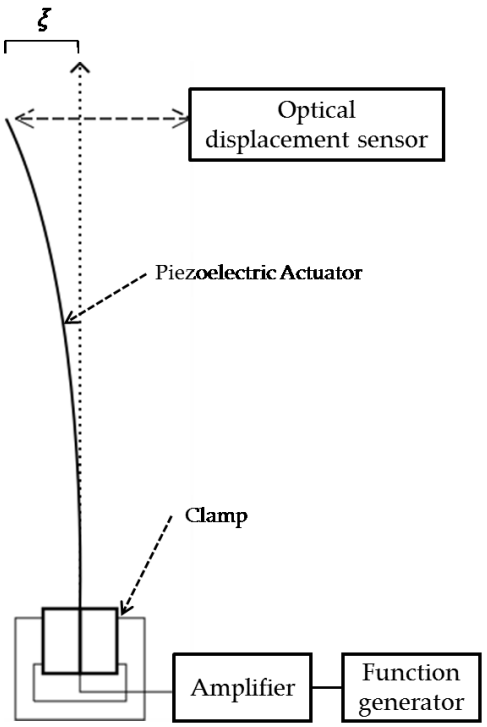

Figure 14. Continuous beam vibration frequency versus displacement at the tip test setup.

Amplitude was measured by the average peak-to-peak distance measured by the displacement sensor and divided by 2 during 3 seconds of stimulation from the total 5 seconds. This was done to avoid accounting for the first and last seconds of the stimulation which would contain misleading data. A graph of the average amplitudes of the oscillation measured against the frequencies is shown in Figure 15. The graph shows the frequency response of the system, where the resonance frequency was 48 Hz.

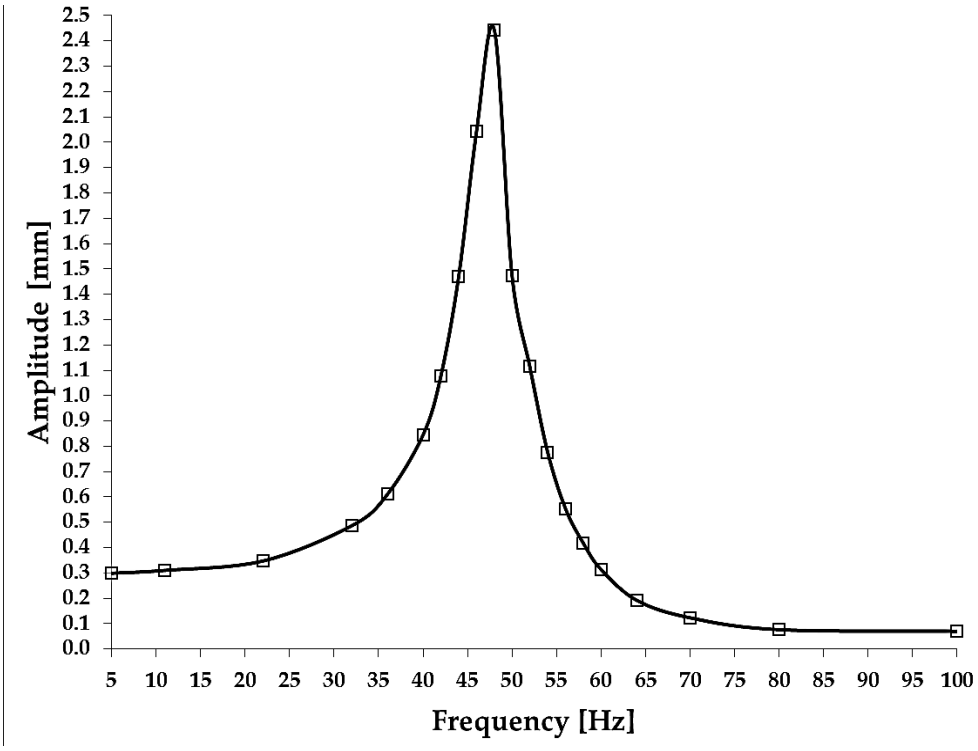

Figure 15. Frequency response test, 2.5g at the tip of the actuator.

To calculate the stiffness from the resonance frequency, as before, the system can be considered as a cantilever beam, but this time with distributed mass and a mass at the tip as shown in Figure 16.

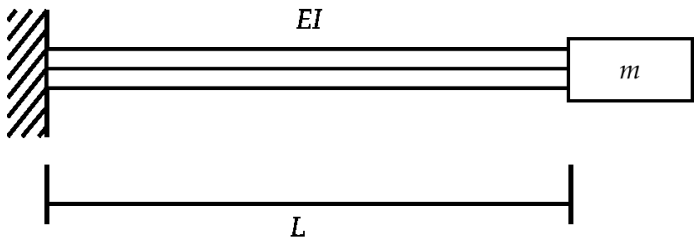

Figure 16. Cantilever beam with distributed mass and mass at the tip.

From modal analysis of a harmonic exited damped system, the natural frequency and the damped natural frequency for are expressed as [70]:

$$\omega_n = \sqrt{\frac{k}{(\frac{m_a}{4} + m)}} \quad \text{rad/sec}$$

Equation 9

$$\omega_d = \omega_n \sqrt{1 - \zeta^2}$$

Equation 10

where ω_n is the natural frequency, m_a is the mass of the actuator, ω_d the damped resonance frequency and ζ the damping ratio. This theory is the same as the massless cantilever behaviour, but provides an effective mass (m_a/4+m) considered to be at the tip. This effective mass of the beam is an good approximation for oscillating cantilever beams with mass, including additional mass at the tip, that is derived from the theoretical evaluation of the rotational distributed inertia of the cantilever and of the mass at the tip [71].

Thus instead of the earlier translational beam theory of Equation 7, and thus replacing Equation 7 in Equation 9:

$$\omega_n = \frac{1}{2\pi} \sqrt{\frac{3EI}{(\frac{m_a}{4} + m)L^3}} \quad \text{Hz}$$

Equation 11

Assuming a very low damping ratio, the dynamic stiffness and young modulus can be obtained by solving Equation 9 for *k* and then Equation 7 for *E*, see Table 2:

Table 2. *k* and *E* from resonance frequency.

Parameter	Value	Uncertainty
ω_n [rad/sec]	302	+/- 2 %
m [g]	2.5	+/- 0.1
m_a [g]	4.8	+/- 0.1
ρ [g/mm]	0.075	+/- 5 %
L [mm]	50	+/- 0.01
Dynamic *k* [N/m]	329.7	+/- 6 %
I [mm4]	0.55	+/- 0.08%
E [N/m2]	2.511x10^10	+/- 6.12%

As expected (by the factors mentioned in page 36), it was found that there was a large difference between the stiffness obtained by the quasi-static method with the electrodes disconnected and the dynamic method [67] (see *k* in Table 1 and Table 2), by a factor of 2.15. In this case, the dynamic stiffness is the relevant mechanical stiffness for this application. Thus the dynamic stiffness (Table 2) must be used for the calculation of the Young's modulus in Equation 11 for the estimation of natural resonance frequencies for the following tests.

More dynamic tests were made with the same method with the addition of using a range of masses at the tip (spheres of moulding clay) ranging from 2.5 to 33.5 grams in order to see the changes in the frequency response of the system.

The estimated natural resonance frequencies for each mass at the tip of the actuator were calculated using Equation 11. This was achieved using the values of *E* and *I* from Table 2 and adjusting *L* for the location of center of mass of the weights attached to the tip.

Table 3. Estimated natural frequencies.

Mass on tip [g]	Uncertainty [%]	*L* [mm]	Uncertainty [%]	Calculated resonance frequency [Hz]	Uncertainty [%]
2.5	+/- 8	53	> +/- 5	52.98	+/- 20.8
5.1	+/- 3.9	53	> +/- 5	37.47	+/- 18.7
7.3	+/- 3	53	> +/- 5	31.22	+/- 18.3
10.0	+/- 2.7	54	> +/- 5	24.39	+/- 18.1
17.3	+/- 1.1	54	> +/- 5	19.76	+/- 17.3
21.4	+/- 0.9	55	> +/- 5	17.29	+/- 17.2
33.5	+/- 0.1	58	> +/- 5	12.74	+/- 16.8

Figure 17 shows a graph of the results from these tests. The measured resonance frequencies are listed in Table 4.

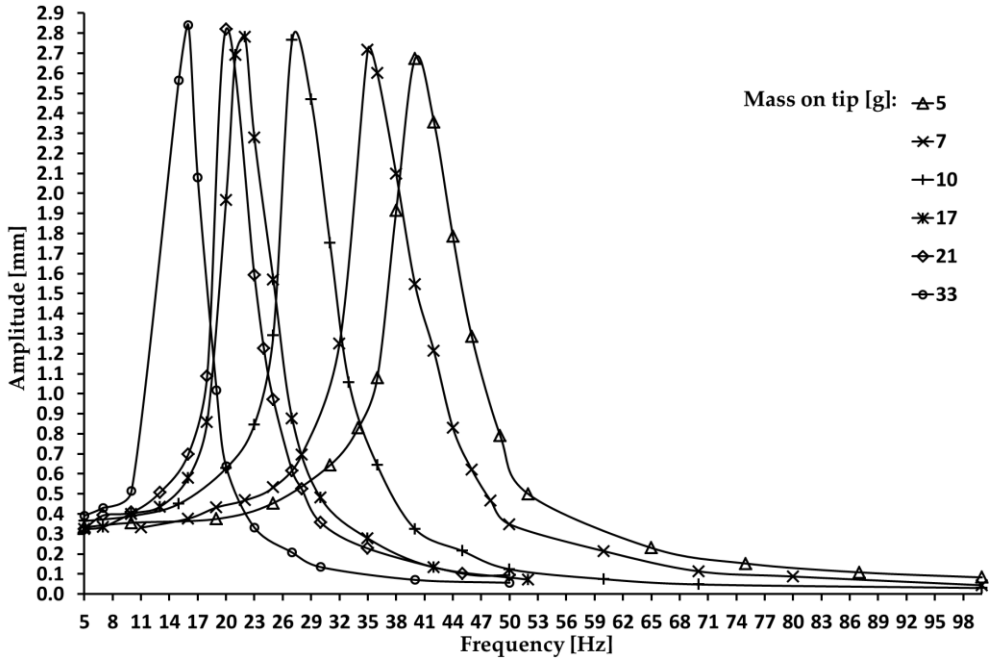

Figure 17. Frequency response tests with different masses at the tip of the actuator.

Table 4. Measured natural frequencies.

Mass on tip [g]	Uncertainty [g]	Measured resonance frequency [Hz]	Uncertainty [%]	Divergence from estimation [%]
2.5	+/- 0.2	48	+/- 2	10.4
5.1	+/- 0.2	40	+/- 2	6.3
7.3	+/- 0.2	34	+/- 2	6.9
10.0	+/- 0.2	27	+/- 2	4.6
17.3	+/- 0.2	22	+/- 2	10.2
21.4	+/- 0.2	20	+/- 2	13.5
33.5	+/- 0.2	15	+/- 2	15.1

It can be seen that the measured resonant frequencies predicted using Equation 11 accounting for rotational inertia in the dynamic system could only be predicted within 15% of error. This prediction error could be attributable to the error in measurement of the position of the centre of the masses placed at the tip. The masses were placed by hand, and the distance from the center of mass

of the weight to the base of the beam was a difficult measurement with a calliper. These factors could have increased the percentage of uncertainty, but the difference between measured resonance frequency and predicted resonance frequency were all within the predicted measurement error.

The damping ratio ζ for the system was determined as follows. A method to determine ζ from the measured frequency response of the single degree of freedom system is called the half power bandwidth method [72]. This method uses two forms that represent damping, the quality factor Q and damping ratio ζ (related by Equation 12) and the frequency width between the -3dB points on the frequency response curve (also known as the transfer magnitude curve). These two points, ω_1 and ω_2 in Equation 13, referred as the half power points can be used to find ζ. By convention, the points are located where the amplitude response is $1/\sqrt{2}$ times its maximum value.

$$Q = \frac{1}{2\zeta}$$

Equation 12

$$\frac{1}{2\zeta} = \frac{\omega_n}{\omega_2 - \omega_1}$$

Equation 13

Tests to determine the damping of the system were performed on 2 different actuators of the same size and 3 times on each one without any mass at the tip. The same setup as the previous tests (Figure 14) was used but in this case white

tape with no significant additional mass was used instead of the 2.5g plastic attachment. In these tests the actuator was stimulated by sinusoidal waveforms at different frequencies, from 5 Hz to 165 Hz, for 5 seconds each time to achieve the frequency response.

For a more accurate estimation of the half-power points from the frequency response, linear interpolation was used between the data points. An example graph of the average response vs. frequency indicating the two half power points is shown in Figure 18.

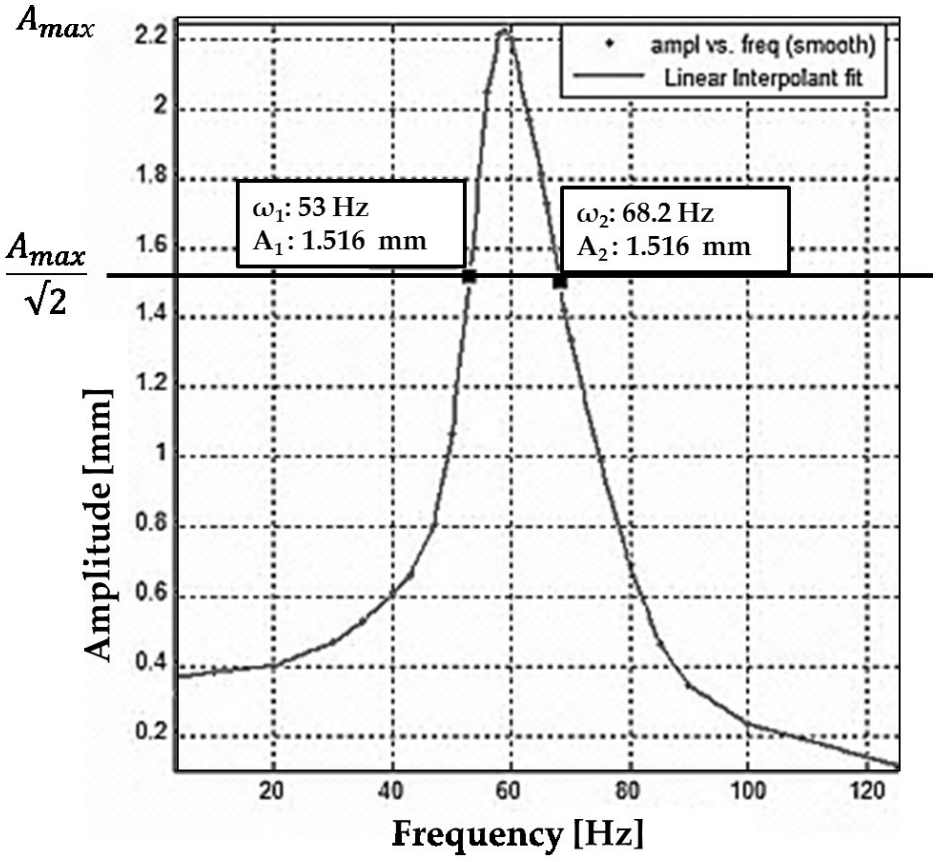

Figure 18. Frequency response test, determination of damping by the half power bandwidth method.

Using Equation 13 the damping ratio for a single actuator was calculated and is indicated in Table 5:

Table 5. Damping ratio by the half power bandwidth method.

Parameter	Value	Uncertainty
Measured resonance frequency ω_n [Hz]	59.40	+/- 2 %
ω_1 [Hz]	53.00	+/- 2 %
ω_2 [Hz]	68.20	+/- 2 %
Damping ratio ζ	0.076	+/- 6 %

As can be observed, the system can be considered to be highly under-damped.

With the value of the damping ratio calculated, it was possible to calculate the Damping Coefficient c by considering the condition for critical damping c_c expressed as

Equation 14 and the percentage of critical damping expressed as Equation 15 [70].

$$c_c = 2\sqrt{km}$$

Equation 14

$$\zeta = \frac{c}{c_c}$$

Equation 15

Using these two equations, the damping coefficient was calculated and is shown in Table 6:

Table 6. Damping coefficient

Parameter	Value	Uncertainty
Mass actuator [g]	4.8	+/- 0.1
Stiffness k [N/m]	667.7	+/- 5.6%
Critical damping c_c [Kg/s]	3.58	+/- 3.8%
Damping ratio ζ	0.076	+/- 5.6%
Damping coefficient c [Kg/s]	0.272	+/- 9.4%

In terms of endurance and durability, these piezoelectric actuators were not provided with a lifespan or performance over time specification. An experiment was made in order to test the reliability and durability of the actuators by stimulating it at resonance frequency for an extended period.

The tests consisted on two independent actuators with 2.5g plastic attachments on top of them in order to tune their resonance frequency to 60 Hz. An adjustable transformer was connected to the building electric network and set to 50 V peak to peak (the maximum AC voltage specified by the manufacturer) and was used to stimulate the actuators. The displacement laser sensor measured the displacement at the tip of each of the actuators for 24 hours of continuous operation.

The data from the displacement sensor showed that the actuators did not show any measureable decrement in displacement performance compared to data form previous short time tests. Displacement measured at the tip of the actuator was constant at 4.5 ± 0.044mm peak to peak throughout the tests. There were also no signs of macroscopic physical damage on the actuators.

The performance assessment tests revealed the basic characteristics of the piezoelectric actuators. The following can be concluded rom the results of these tests:

- As expected, the mass at the tip of the actuator decreased the resonance frequency although the theoretical approximation diverted from the measured up to 29%, see Table 4.
- There was a slight increase in amplitude with larger masses that could be attributed to inertia.
- The peak of the frequency response curves got narrower (increase in Q factor) with larger masses, and
- Regardless of mass at the tip, the low frequency behaviour below resonance produced similar amplitudes of oscillation (e.g. 0.3 – 0.4 mm at 5 Hz).
- The measured damping ratio on the actuator alone was very low, although not negligible.
- The frequency response curves showed the maximum displacement at the tip of the actuator (without any amplification) was roughly consistent for the frequencies of interest for FOT (see section 1.6.1).

Knowing the frequency response of the actuator enabled me to make design choices for the prototypes for the desired motion generation of the moving-mesh. Since the pressure generated by the oscillation requires higher displacement at low frequencies and the displacement decreases as the frequency increases (further explained in section 2.5.2), 3 potential types of

prototypes, regarding the actuators and the target frequencies for FOT, came in to consideration at this point: below the resonance frequency, at the resonance frequency, and over the resonance frequency.

A prototype running below the resonance frequency would have the actuator(s) tuned to have a resonance frequency beyond the desired range for FOT. The prototype would make use of the low but consistent displacement by mechanical amplification aimed to the highest displacement required at the lowest forced oscillation frequency and adjust the amplitude for higher frequency by voltage changes (signal amplitude). This configuration would be capable of delivering multiple frequencies combined in a composite signal.

A prototype running at resonance frequency would be tuned to deliver a single frequency forced oscillation equivalent to the resonance frequency. This configuration would be the most simplistic and energy efficient, although it would be limited to one frequency.

And a prototype running over the resonance frequency would take advantage of the resonance frequency as well as the large amplitudes obtained on the frequencies after it. This configuration would also be capable of delivering multiple frequencies combined in a composite signal. The system would be tuned to have its resonance frequency on the lowest forced oscillation frequency desired. Due to the rapid decline in amplitude after the resonance frequency, as seen in Figure 15 where the amplitude at 5 Hz after the resonance frequency decreases almost 10 fold, a combination of voltage amplitudes adjustments would be required. At the resonance frequency the required amplitude would have to be obtained with lower voltage amplitude than the

maximum recommended by the manufacturer so that more voltage can be applied for the higher frequencies as needed.

The equipment used for the actuators performance evaluation tests is listed below:

- Fluke 120 Series Industrial ScopeMeter® Portable Oscilloscope.
- AR200-50M Acuity's triangulating laser displacement sensor kit.
- High Voltage Amplifier/Piezo Driver - Model A-301HS.
- Tenma 72-7255 Digital Scale.
- Duratool D00377 Digital Calliper.
- B&K Precision 4001A Function Generator.
- The software used to analyze the data was MatLab version 7.11 and MS Excel.

2.4. Pneumotachometer module

A pneumotachometer (pneumotach) is a device that converts the flow of a gas passing through it into a signal of pressure difference (ΔP_p) across a mesh which has a fixed resistance R_p. The pressure is measured from two ports, one on each side of the mesh as shown in Figure 19.

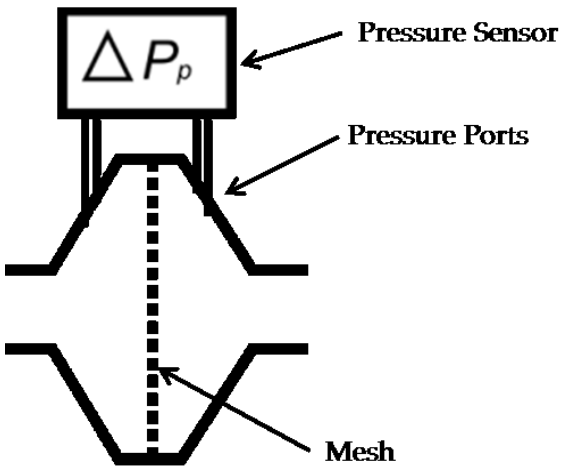

Figure 19. Pneumotach diagram.

The gas flow is obtained from Equation 16:

$$\Delta P_p = R_p \cdot \dot{V}$$

Equation 16

Two different pneumotachometers, one off-the-shelf and one custom-made, were used with the prototypes. The off-the-shelf one, a Hans Rudolph model 4719, was used with the first small prototype for easy implementation (see Figure 31). A custom-made pneumotach assembly was designed and build in order to use it as a removable module on the other prototypes, see Figure 20.

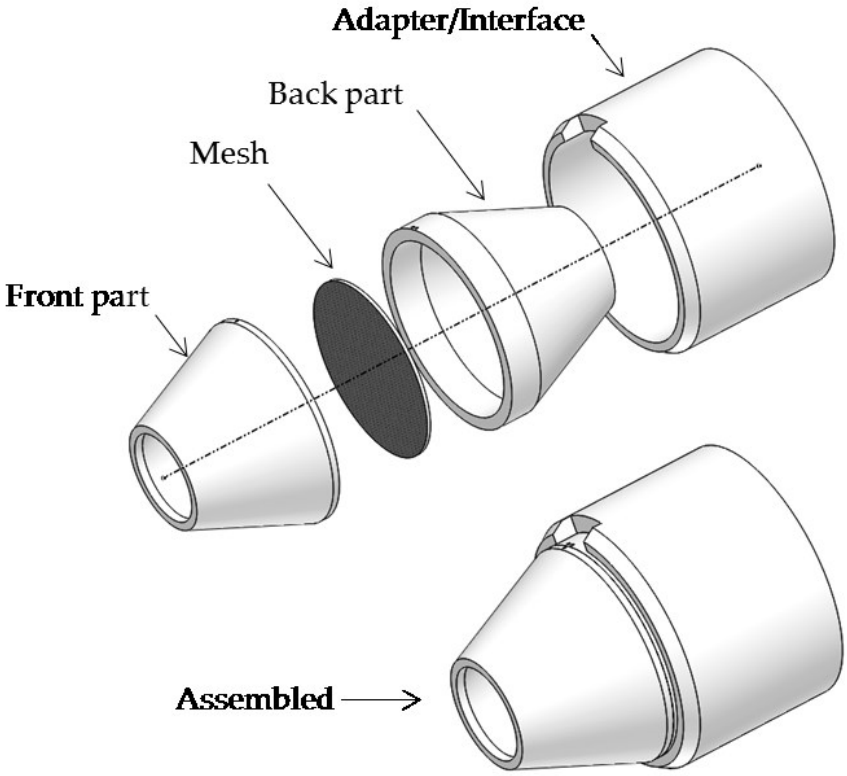

Figure 20. Custom made pneumotach module 3D model, isometric view, exploded and assembled.

The pneumotach was designed to be simple to assemble. Two parts, the front and the back, are press-fit with a 5cm diameter mesh in between. The mesh used was a corrosion resistant 304 stainless steel woven wire cloth of 500 threads per inch, 0.0008" wire diameter, 0.0012" opening size and an open area of 36%. The resistance of the mesh 5cm diameter mesh was measured to be 0.40 $cmH_2O/L/sec$ ±3%. The set-up used to do this measurement is shown in Figure 21 and it used the following equipment:

- TSI mass flowmeter model 40241.
- TSI micromanometer model DP-CALC 5815.

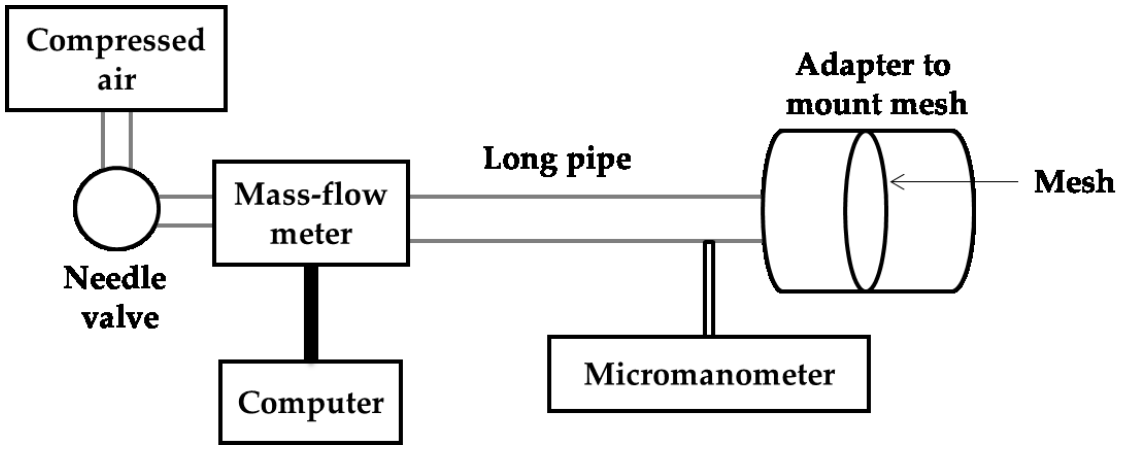

Figure 21. Set-up to measure resistance to air flow.

In this resistance to flow measurement set-up, the mesh is placed in line with the flow of air and the pressure drop is measured. The needle valve was open to the point where the mass-flow meter measured 1 l/sec and then the reading from the micromanometer was taken to get the resistance.

The adapter/interface part of the pneumotach was designed to act as the linkage with the other parts of the prototypes. It is press-fit on top of the pneumotach so that different versions/shapes of this part could be used if needed. The parts shown in Figure 20, except the mesh, were CNC machined.

The design of this custom-made pneumotach differs from the standard because an additional port was added to one side in order to measure P_{ao} as close to ΔP_p as possible so that the measurements are in phase. This feature is shown in Figure 22.

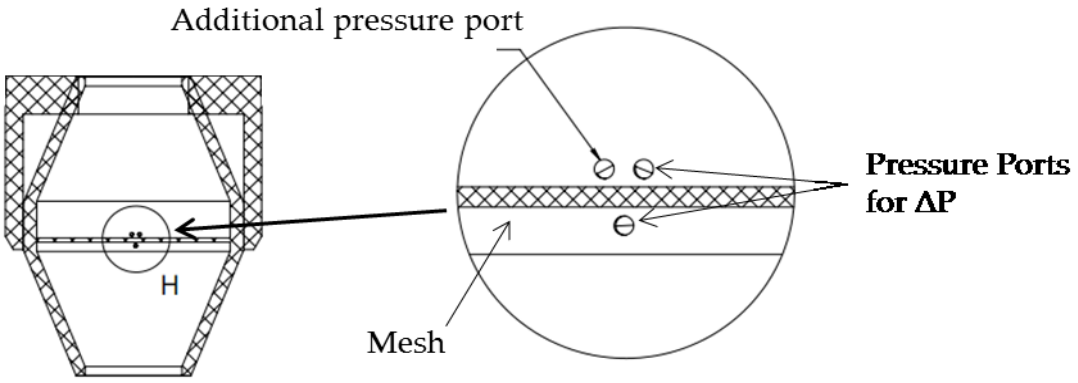

Figure 22. Custom made pneumotach module 3D model, top plane section view and detail view (circle).

The pressure channels consist on off-the-shelf tube fittings screwed in holes shown as "pressure ports" in Figure 22, and flexible tubes which are connected to a pair of symmetrical differential Scireq pressure transducers model UT-BDP-05 (2 inH_2O range) for ΔP_p and P_{ao}.

2.5. Design of the prototypes

2.5.1. First prototype

This section describes a small prototype that was design and constructed for preliminary testing of a single actuator type of design. The purpose for this prototype was to generate proof of design for the other prototypes using only one actuator, as well as provide data to see the displacement performance of the actuator with a mesh-disk on top during simulated (by a pump) breathing noise.

The prototype was design to work at resonance frequency. The overall assembly consisted on two sections; the actuator block (see Figure 23) supporting the piezoelectric actuator and the camber around the mesh-disk.

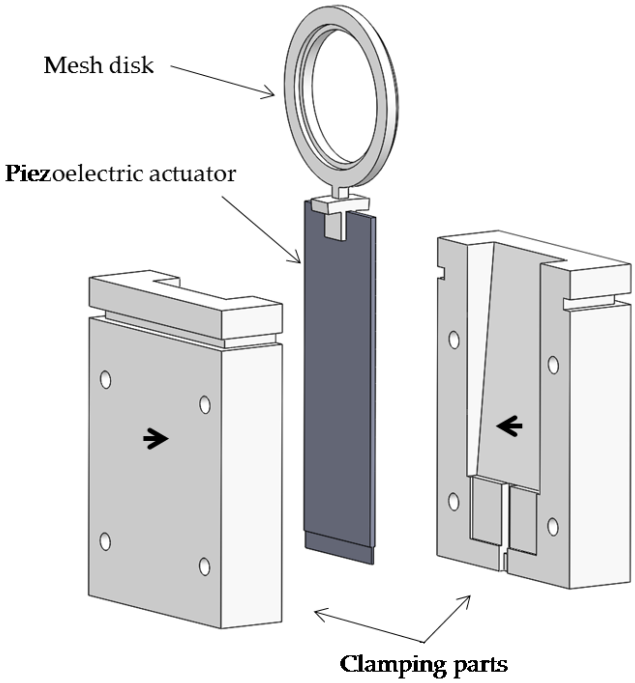

Figure 23. Clamped piezoelectric actuator assembly.

The actuator block shown in Figure 23 comprises 2 parts that act as the supporting clamp for the actuator, pressing on it at the lower end and giving it room to move as well. The clamping parts are joined by bolts going through the four orifices on these parts which also provide the clamping force.

The 3D model of the assembled prototype is shown in Figure 24. In this image the prototype is displayed with one of the two parts that forms the chamber around the mesh-disk removed in order to show the inside. The parts for the prototype were 3D printed with a Stratasys 3D printer model Dimension 1200 with a layer thickness of 0.33 mm. The mesh-disk was made with an outer 3D

printed ring (seen in Figure 23) and a second inner ring to which wire cloth (mesh) of 500 threads per inch was attached to. The mesh resistance, measured with the set-up shown in Figure 21, was 0.81 $cmH_2O/L/sec$.

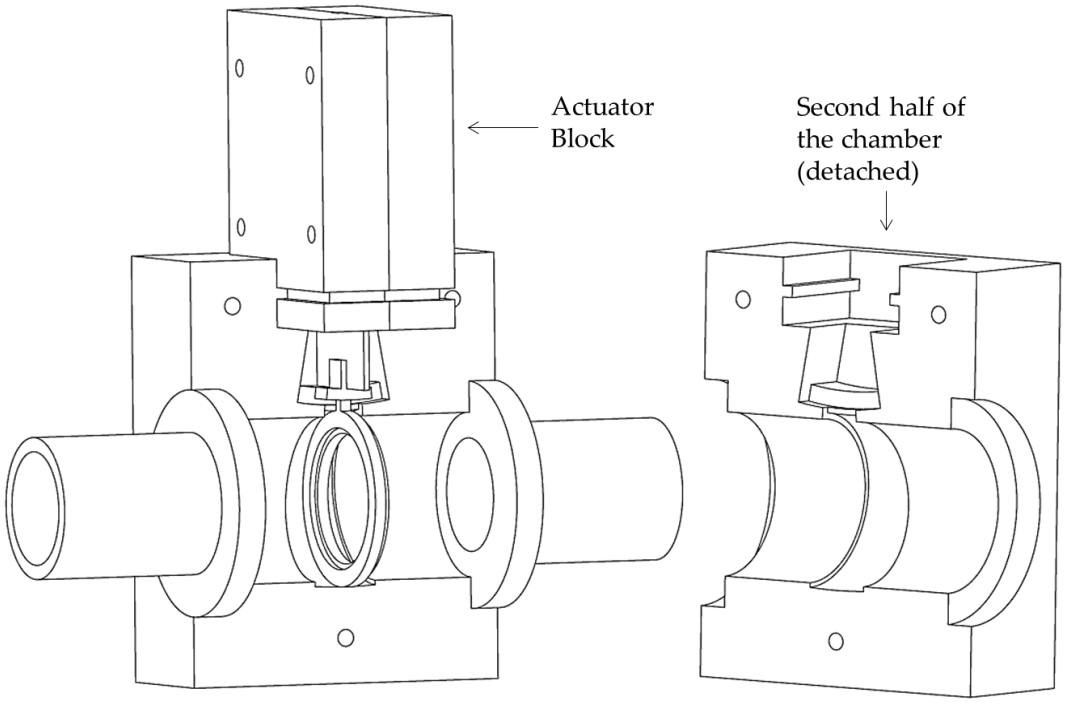

Figure 24. 3D model of the first prototype assembled (chamber open).

One of the first concerns for the use of this type of design was the impact of a load (such as breathing flow) on top of the moving actuator and mesh-disk while performing a forced oscillation. In order to see the displacement performance of the prototype under these conditions, a testing set-up including the following:

- Harvard Apparatus respirator pump model 607.
- AR200-50M Acuity's triangulating laser displacement sensor kit.
- High Voltage Amplifier/Piezo Driver - Model A-301HS.
- B&K Precision 4001A Function Generator.

- Hans Rudolph pneumotach model 4719.
- Scireq pressure transducers model UT-BDP-05 and amplified by a Scireq amplifier model SC-24.
- National instruments data acquisition card model USB-6008.

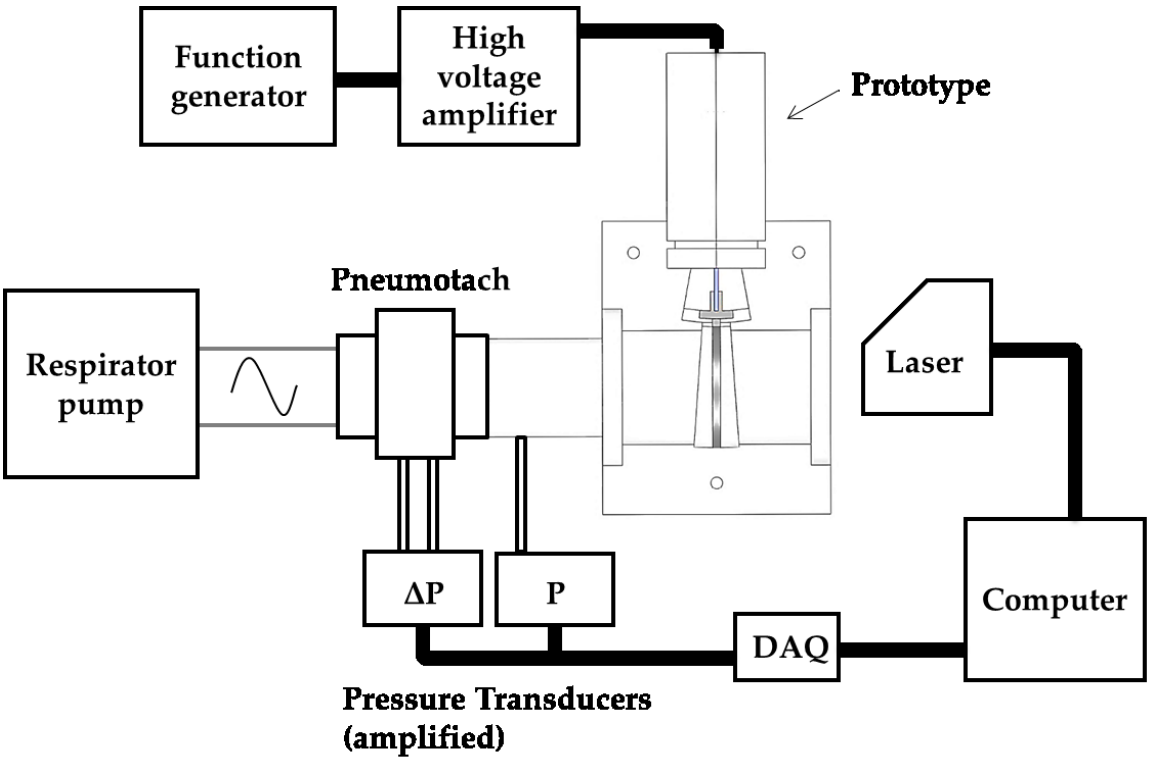

Figure 25. Testing set-up for first prototype.

Figure 25 shows a diagram of the testing set-up. A set of tests were performed with this setup. First, with the respirator pump detached, the actuator was stimulated at the resonance frequency and 50 p-p voltage. With a mesh disk of 6.9g the resonance frequency obtained was 35 Hz. The displacement was measured with the laser sensor kit pointed at the tip of the actuator at a sample

rate of 500 samples/sec. The test was performed 5 times for 5 seconds. Figure 26 and Figure 27 are examples of the data acquired by the laser:

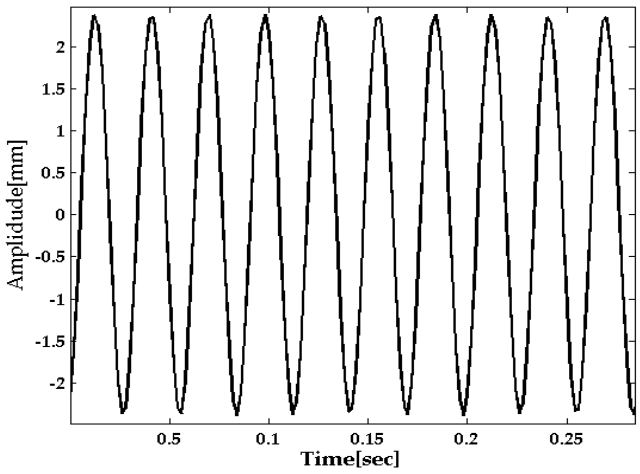

Figure 26. First prototype, measured displacement at the tip of actuator oscillating at 35Hz.

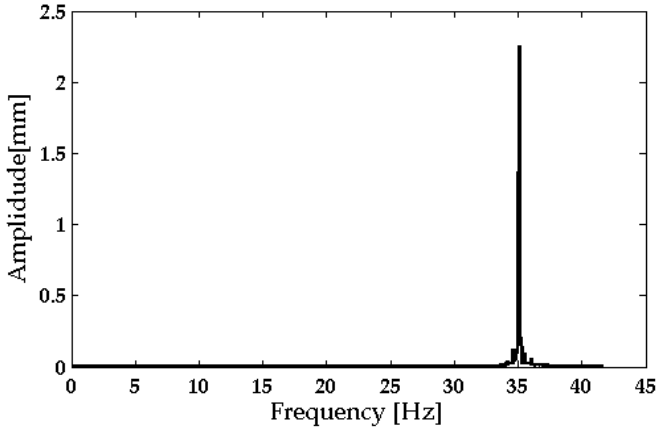

Figure 27. First prototype, FFT of the measured displacement at the tip of actuator oscillating at 35Hz.

The maximum average amplitude displacement at the tip of the actuator was 2.35mm with a standard deviation of 0.03mm. This measurement was made

(using MatLab®) by taking the peaks of the signal on each recording and then averaging them.

The second set of tests involved the addition of the simulated breathing provided by the respirator pump. To see the base noise, the displacement at the tip of the actuator was measured without the actuator being stimulated. Figure 28 shows an example of this displacement. This measurement was performed 3 times for 10 seconds at 500 samples/sec. The respirator pump was set to 15 cycles/minute, 600cc stroke (1200cc per cycle). The average amplitude displacement measured, obtained using the same method with MatLab®, was 0.55mm with a standard deviation of 0.01mm.

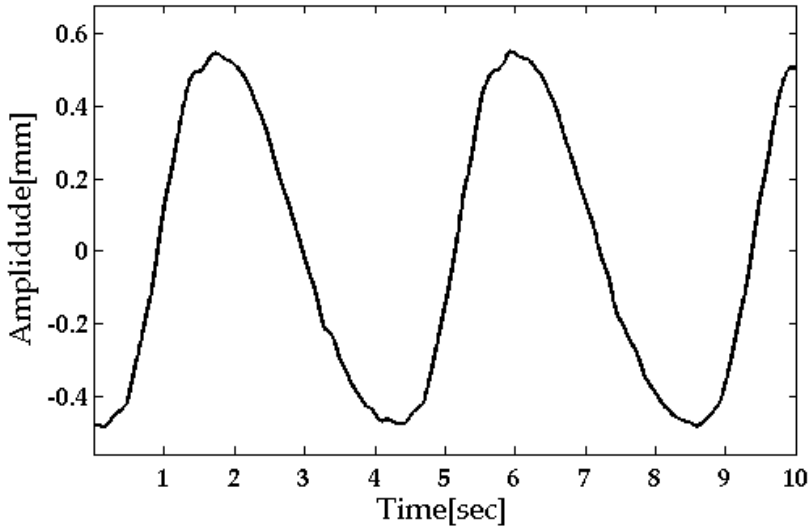

Figure 28. Displacement effect on actuator tip by simulated breathing noise from respirator pump.

With the respirator pump running at the same rate, the actuator was stimulated at 35 Hz as the previous test. This was done 5 times for 5 seconds. Figure 29 (bottom) shows an example of the displacement measured and the 35 Hz can be seeing over imposed on top of one cycle of the breathing noise.

In order to see the variation of the peak to peak displacement, the peaks and valleys of the signal where found and added up. Figure 29 (top) shows an example of this variation. It can be seen that in this scenario the p-p displacement slightly lower during the valleys (expiration) of the respirator noise compared to the peaks and an increase where the displacement effect of the respirator noise on the actuator is low.

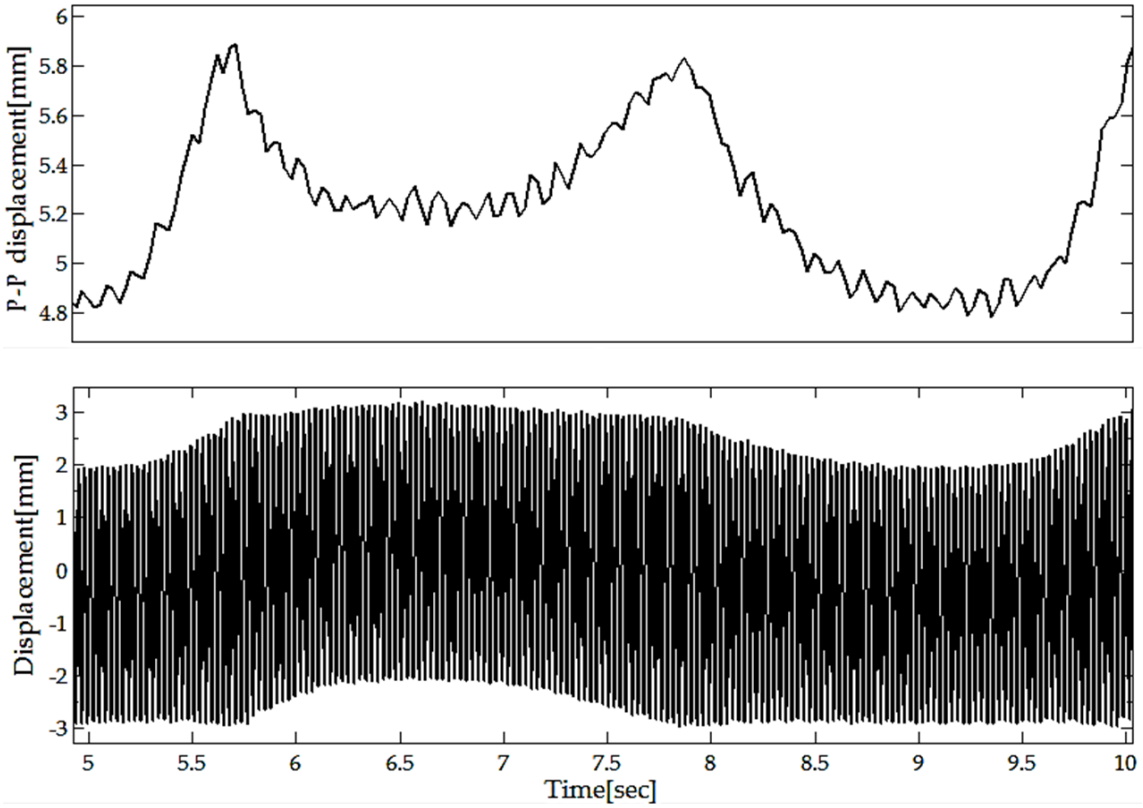

Figure 29. Bottom: 35Hz over respirator noise. Top: P-P displacement variation.

As can be seen in Figure 30, the peak-peak displacement at 30 Hz was sensitive to the breathing perturbation ranging from 4.8 to 5.8 mm peak-peak and showing a slightly higher value of 5.3 mm during the expiration (6.5 to 7 sec) than the inspiratory (inspiration is positive flow) phase of 4.9 mm (9-9.5 sec),

with peaks in the transitions at 5.8, 8 and 10 sec. The variation in the amplitude could be estimated from the standard deviation of the peak-peak measurements and was 0.30 mm. After filtering the data using a 10^{th} order Butterworth band-pass filter with cut-off frequencies at 30 and 40 Hz, the peaks of the signals were obtained from the 3 recordings using MatLab® and then an average amplitude of 2.58 mm with a variation of 0.14mm were calculated from all the peaks. Comparing this result to the initial test without respirator noise it can be see that the amplitude of the oscillations at resonance frequency of the actuator did not change substantially and the performance of the actuator was not compromised.

Measurements of pressure and flow using the pneumotach and pressure sensors, as shown in Figure 25, were made but since no resistance test load was used the data was not informative or useful regarding impedance measurement performance.

2.5.2. Prototypes to meet the recommended design requirements

The mechanical parts for two prototypes were designed following the findings of the performance evaluation of the piezoelectric actuators. One prototype was designed to work at resonance frequency using only one piezoelectric bimorph actuator. And another was designed to be a multi-frequency actuator and work below the resonance frequency and using multiple bimorph actuators. A multi-frequency actuator for above resonance was not attempted as being more challenging and assembling and testing two prototypes was already an ambitious goal.

For both single and multiple actuator prototypes, the design embodied a moving mesh to impose pressure oscillations on top of the patient's breathing using the same concept tested in the first prototype described in the previous section.

A different form of mechanical displacement amplification, inspired by the methods described in section 1.7.2, was implemented in each prototype to increase the displacement of the piezoelectric actuators.

In order to meet the general criteria and recommendations for FOT clinical practice from Oostveen et al.'s [43] described in section 1.5, calculations were made to determine the geometric dimensions of the main component of the system: the mesh-disk moved by the piezoelectric actuator(s) and the chamber enclosing it.

The displacement at the tip of the piezoelectric actuator is curved and the volume that the moving mesh-disk would displace can be approximated to a section of a ring torus. The volume of a ring torus (or section of) is the same to a cylinder (Equation 17) with length x equal to line running around the center of the ring torus.

$$V = x \cdot \pi r^2$$

Equation 17

The length of the cylinder required in this case will be the peak-to-peak linear motion on the curved arc x as in Equation 18. If the displacement is oscillatory with the motion being approximately sinusoidal, we can write:

$$x = a \cdot \sin(\omega t)$$

Equation 18

where a is the amplitude of oscillation at the center of the mesh-disk, t is the time, ω is the angular frequency.

Replacing Equation 18 in Equation 17 and deriving we get flow (assuming a solid disk instead of a mesh) as:

$$\dot{V} = a \cdot \omega \cdot \cos(\omega t) \cdot \ \pi r^2$$

Equation 19

With a solid or mesh disk, the relationship between pressure and flow will be as in Equation 20:

$$P = \dot{V} \cdot R_T$$

Equation 20

where P is the pressure difference, R_T is the total (parallel resistance) to air flow through the wire cloth (mesh) and any leak around the disk, described in Equation 21.

$$R_T = \frac{R_{Mesh} \cdot R_{Leak}}{R_{Mesh} + R_{Leak}}$$

Equation 21

Replacing Equation 19 in Equation 20 and rearranging for a gives Equation 22.

$$a = \frac{P}{R_T \cdot \omega \cdot A}$$

Equation 22

$$A = (\pi \cdot or^2) - (\pi \cdot ir^2 \cdot \gamma)$$

Equation 23

where A is the surface area of the disk and mesh, r_o is the outer radius of the mesh, r_i is the inner radius and γ is the percentage of open area of the wire cloth (mesh).

Equation 22 was used to calculate the displacement (amplitude) at which the mesh-disk with surface area A must move to achieve the chosen pressure and resistance magnitudes at a particular frequency.

Figure 30 shows the required amplitude of oscillation for different mesh-disk surface areas for the case of oscillating pressure amplitude of 1 cmH_2O and mesh resistance of 1 $cmH_2O/l/sec$. This plot was used to guide the determination of the surface area (dimensions) of the mesh-disks of the prototypes.

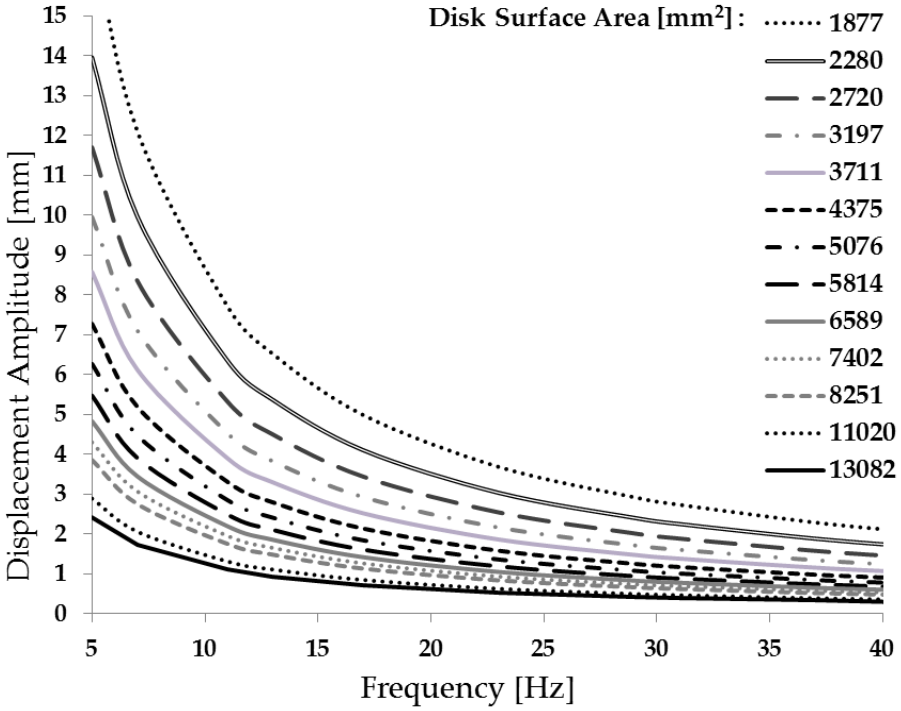

Figure 30. Required Displacement vs. Frequency using Equation 22.

The mechanical parts of the prototypes were 3D modeled in SOLIDWORKS®. The 2D drawings these parts were included in Appendix A. Then the custom parts were machined by the company RPWORLD (Beijing, China) using computer numerical control (CNC) machining, and for their assembly off-the-shelf hardware was used. Other off-the-shelf mechanical components used were the piezoelectric actuators, flexible air pipe and fittings.

More details on the mechanical design of the prototypes are presented in the following sections.

2.5.2.1. Single-actuator device

The single-actuator prototype was designed to work at resonance frequency to take advantage of the larger displacement of the actuators at such frequency. It was also designed to apply a single frequency oscillation.

One of the first considerations was the damping effect that would arise from the disk with surface area such as the ones shown in Figure 30 and how that would affect particularly the amplitude performance at the resonance frequency of the system. To address that question experiments similar to the frequency response characterizations performed in section 2.3.1 were performed with a plastic disk with a 10 cm diameter and a weight of 21 grams on top of the actuator as in Figure 31.

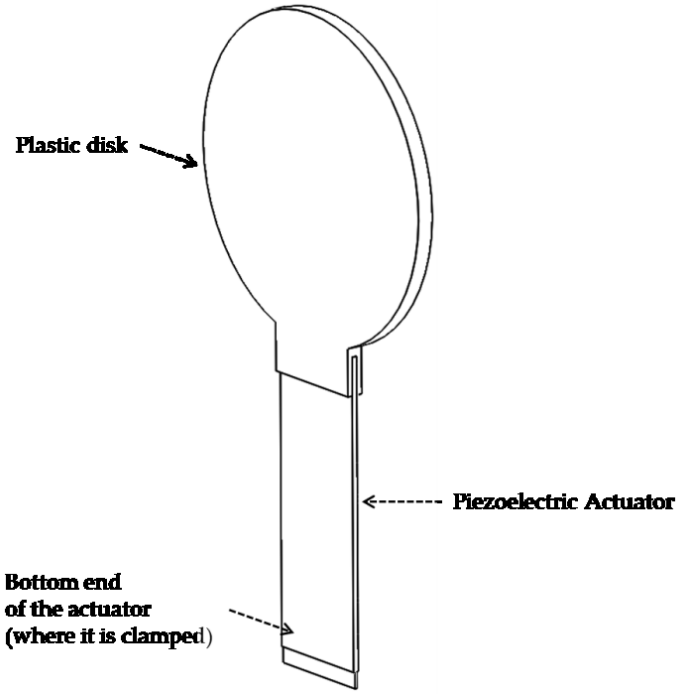

Figure 31. Piezoelectric actuator with disk on top.

Figure 32 shows a graph of one of the experiments that shows the average amplitudes of the oscillation measured against the frequencies and the two half power points for the half power bandwidth method to assess the damping ratio.

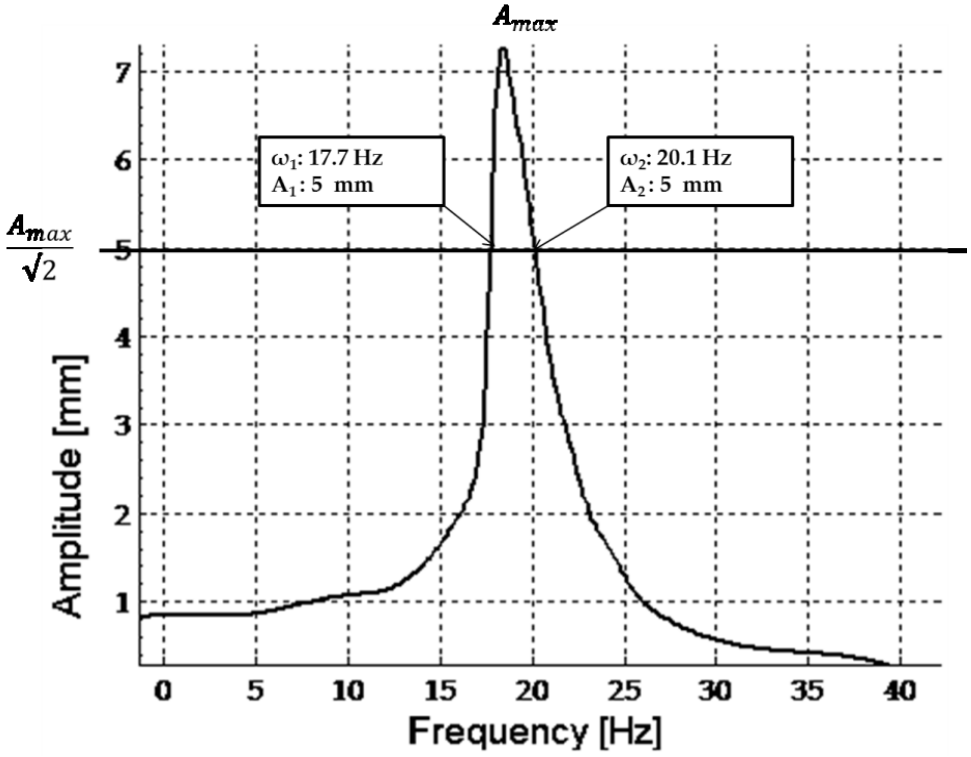

Figure 32. Frequency response test, determination of damping of actuator with disk on top by the half power bandwidth method.

By Equation 13 the damping ratio was calculated:

Table 7. Damping ratio by the half power bandwidth method, disk on top of actuator.

Parameter	Value	Uncertainty
Measured resonance frequency ω_n [Hz]	18.5	+/- 2 %
ω_1 [Hz]	17.7	+/- 2 %
ω_2 [Hz]	20.1	+/- 2 %
Damping ratio ζ	0.065	+/- 6 %

The low value for the damping ratio confirmed that the damping effect against no load (such as breathing) was minimal. Even though the damping ratio was expected to increase when the mesh-disk moves inside a chamber against a resistance, the effect was still expected to be small since only for ζ greater than 0.3 the effect on resonant frequency would be more than 5%, and ζ is not expected to exceed 0.1.

Two approaches can be used for analysis of the dynamic system. The first is assuming the mass of the molding clay is all located at the tip and the second is to more accurately calculate the moment of inertia using the parallel axis theorem that could be applied for a distributed mass of any moving body of finite volume that rotates around a fixed centre. In this chapter I first consider the fixed point approach. Given an estimated distance from the center of mass to the base of the cantilever (approximated to be with the added mass centred at the tip), Equation 11 can used to calculate a theoretical estimate of ω_n for point masses at the tip of the actuator from 1 to 100 grams as shown in Figure 33. These theoretical estimates were calculated by incrementing m in steps of 1 gram and assuming an increment of L by 0.25 mm per gram to account for the shift in centre of mass for the molding clay.

More experiments similar to the ones performed in section 2.3.1 were made with fabricated disks. As was seen in that section, the resonance frequency found in practice did not exactly match the model likely do to the fact that the disks had more distributed mass, and approximating their mass at their centre of mass is an approximationg; however the point-mass approximation was sufficiently accurate to predict resonance frequency to within about 1 Hz as can be observed in Figure 33. Figure 33 shows the comparison of the experimental

data to the theoretical estimation. It can be observed that using Equation 11, which accounts for rotational inertia of the beam including mass at the tip, and incrementing the location of the mass at the tip to approximately account for the changes in center of masses used in the experiment, describes reasonably well the observed experimental behavior.

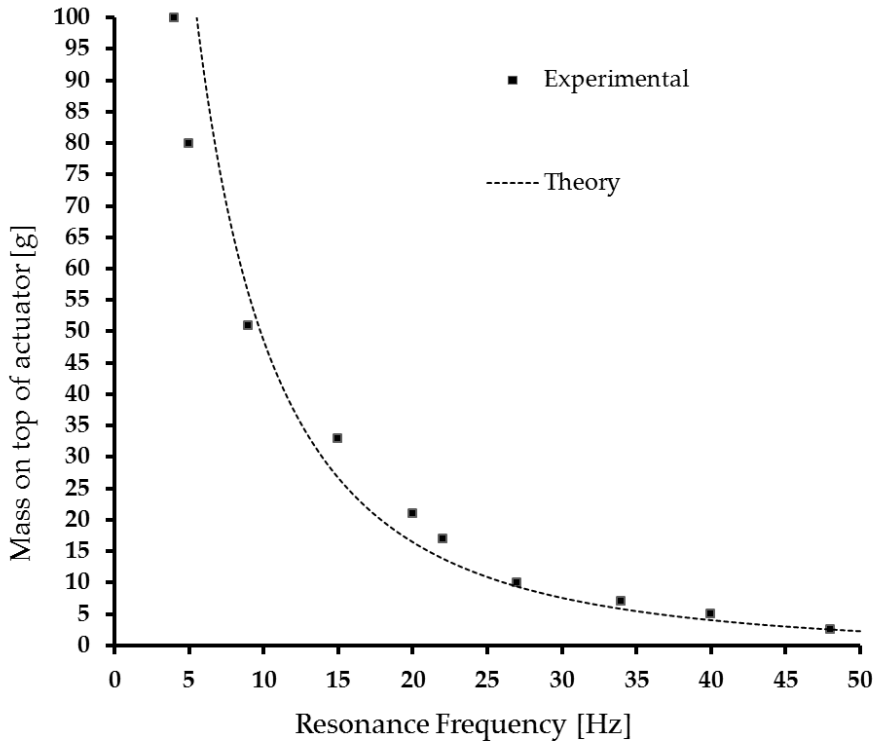

Figure 33. Mass at tip vs. Resonance Frequency with the theoretical prediction being according to Equation 11.

Based on the theorical model based on Equation 11, the mass at the tip of the piezoelectric actuator could be chosen for the desired ω_d. This model is strictly only valid for the case where distance to the centre of mass at the tip increases approximately 0.25 mm per gram approximating the experimental data. The theoretical curve should be used for design to use for different locations for the

centre-of-mass of the mass of the tip or for any changes in actuator material properties or dimensions.

The other approach to determine the resonance frequency of the system is to analize it as an inverted compound physical pendulum taking into account the rotational inertia of the system elements, and considering torque rather than translational force. Figure 34 shows free body force diagram of the system.

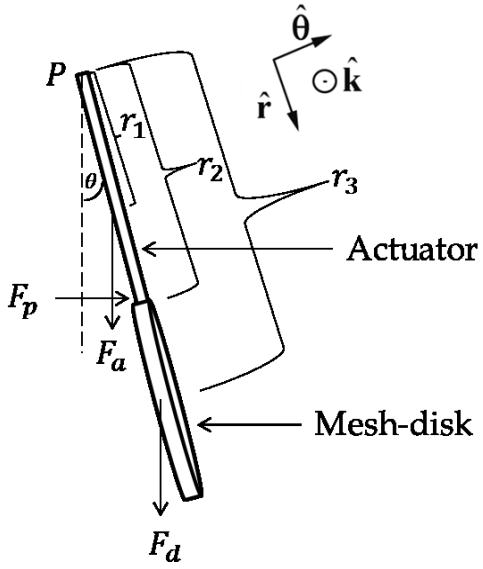

Figure 34. Force diagram of single-actuator system.

In this figure $\hat{k}$ is the normal plane of motion, θ is an angle such that counter clockwise rotation is a positive z-component of the angular velocity and therefore, a torque pointing out of the page has a positive z-component. The pendulum undergoes fixed axis rotation about point P. The force from the piezoelectric actuator F_p acts as at distance r_2 where the tip of the actuator is connected to mesh-disk. The gravitational force acts at the center of mass of the actuator F_a at distance r_1. Considering the mesh disk as a separate body, the

gravitational force acts at the center of mass of the mesh-disk at distance r_3. The torque about point P is given by:

$$\tau_p = r_2 \cdot F_p \cos\theta - r_1 \cdot F_a \sin\theta - r_3 \cdot F_d \sin\theta$$

Equation 24

Since the angle θ is small (maximum angle was 6°), sin(θ) can be assumed to be equal to 0 and cos(θ) to be unity. Then the torque can be considered as the one created by the force of the piezoelectric actuator at r_2:

$$\tau_p = r_2 \cdot F_p$$

Equation 25

where F_p is expressed as Equation 8 for the stiffness of the actuators and the displacement they generate.

$$F_p = k_d x$$

Equation 26

The angular frequency (resonance frequency) can be expressed as [73]:

$$\omega_n = \frac{1}{2\pi}\sqrt{\frac{r_2 \cdot k_d \cdot x}{I_p}}$$

Equation 27

where I_P is the moment of inertia about the pivot point P. Note this expression depends on the achieved amplitude of oscillation x, which also varies with frequency. Also I_P can be considered as the sum of moments of inertia of the actuator and the mesh-disk:

$$I_P = I_{P,disc} + I_{P,act}$$

Equation 28

where $I_{P,disc}$ is the moment of inertia of the mesh-disk and $I_{P,act}$ is the moment of inertia of the actuator, about the point P applying the parallel axis theorem.

For this design I considered the theoretical model shown in Figure 33 sufficient to use for choosing an approximate mass needed for the mesh disks for the desired resonant frequencies, with the location of the centre of the mass of the mesh disks to be reasonably close to the experimental locations. In order for the system to be able to apply two different frequencies (not at the same time) with two different mesh-disks, the mass chosen for a frequency equal to 5 Hz was 82.7g, and for 19 Hz was 22.3g. With the surface area design guide from Figure 30 in mind, Equation 22 and Equation 23 were used to design the mesh-disk and determine their inner radius and outer radius considering that the wire cloth (mesh) chosen to be used in the middle of the disks was a corrosion resistant 304 stainless steel woven wire cloth of 500 threads per inch, 0.0008" wire diameter, 0.0012" opening size and an open area of 36%.

Consecutively, two materials with different densities (ρ) were selected so that the outer radius and thickness of the two mesh-disks remained constant. This allowed both disks to move in the same chamber. The materials used were brass for the 5 Hz mesh-disk and ABS for the 19 Hz one.

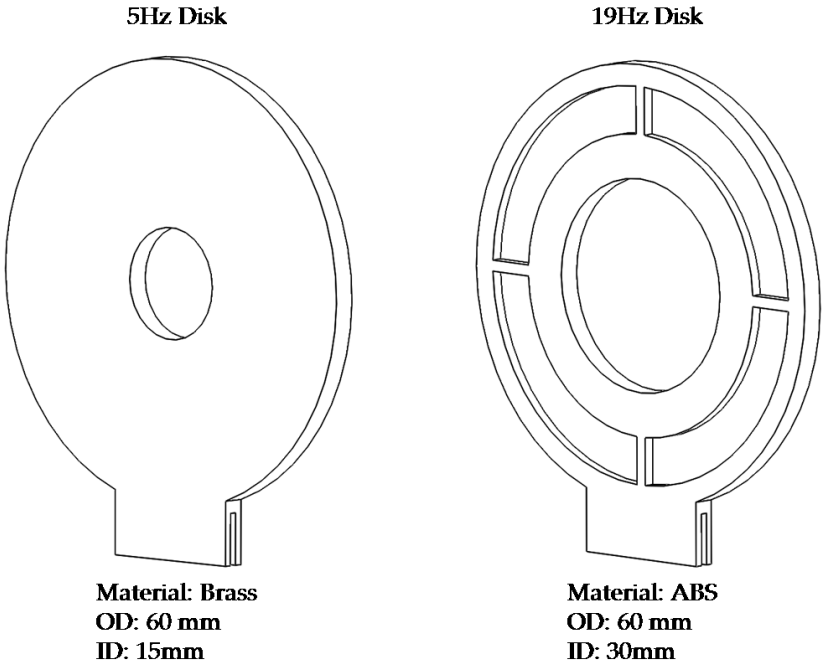

Figure 35. Single frequency prototype's mesh-disks

To corroborate the approximation approach to selecting the masses of the mesh-disk with the model shown in Figure 33, the 3D model of the designed mesh-disks attached to the tip of the actuator was used to analyze the system with the inverted compound physical pendulum approach as follows.

With the help of Solidworks®, I_P (as in Equation 28) for the brass and the ABS mesh-disks were computed. The results are shown in Table 11 and Table 9.

Table 8. Moment of inertia, low frequency disk single-actuator prototype.

Parameter	Value [g・mm^2]
$I_{P,disc}$ (Brass)	24735
$I_{P,act}$	171
I_P	24906

Table 9. Moment of inertia, high frequency disk single-actuator prototype.

Parameter	Value [g・mm^2]
$I_{P,disc}$ (ABS)	2620
$I_{P,act}$	171
I_P	2891

The resonance frequencies were obtained using Equation 27 with the parameters shown in Table 10. The calculation was made by setting the displacement (amplitude) at the tip of the actuator to be 3 mm (the maximum in this prototype) and estimated dynamic stiffness from Table 2.

Table 10. Resonance frequency of low frequency disk single-actuator prototype.

Parameter	Value
x [mm]	3
Estimated k_d [g・mm/s^2/mm]	329700
r_2[mm]	50
I_P [g・mm^2] (Brass disk)	24906
Estimated ω_n [Hz] (Brass disk)	7.1
I_P [g・mm^2] (ABS disk)	2891
Estimated ω_n [Hz] (Brass disk)	21.1

The estimated resonance frequency by this method for the 80 g (approximated mass in the 3D model) mesh-disk was 7.1 Hz compared to the 5 Hz used in the previous method, and for the 20 g (approximated mass in the 3D model) mesh-disk was 23.4 Hz compared to 19 Hz. This discrepancy is likely due to the assumptions made to simplify the model and the calculations, but also perhaps due to the estimated k_d.

For the design of the chamber around the disk, an arc following the trajectory of the tip of the actuator seen during the experiments was approximated and

adjusted according to the disk size. Also, the edges inside the chamber parts were rounded where possible in order to decrease possible turbulence.

For the area between the mesh-disk and the walls of the chamber (leak), a number of factors were considered when designing the dimensions involved. In Equation 21 is easy to see that the leak, when low, highly reduces the total effective resistance to air flow. To minimize the leak (maximize the resistance) around the disk, the design goal of the gap is to be as small as possible without creating friction between the disk and the wall of the chamber. However, the manufacturing process resolution for the mechanical parts acts as the main limitation to achieve this. The machining resolution offered by the selected manufacturer to make the parts was 0.13mm. Accounting for the stack-up of tolerances the gap between the mesh-disk and the surrounding wall was designed to be 0.5 mm (Detail E, Figure 38). When assembling the parts, a layer of tape 0.025mm thick was planned to be added around the mesh-disk to reduce the gap if necessary.

The following are figures that show the 3D model made for this prototype:

Figure 36 shows an isometric view of the prototype assembled with one of the parts that form the chamber, in which the mesh-disk moves, removed.

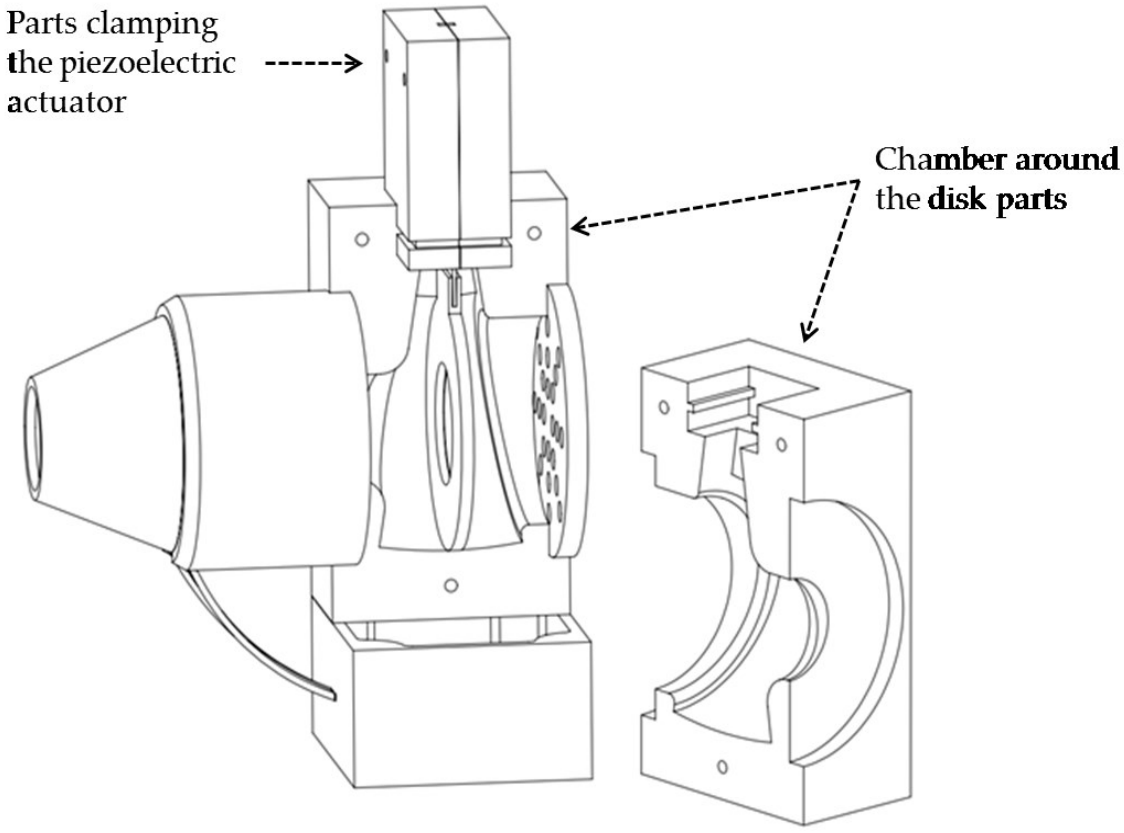

Figure 36. Isometric of the assembled 3D model of the single actuator prototype

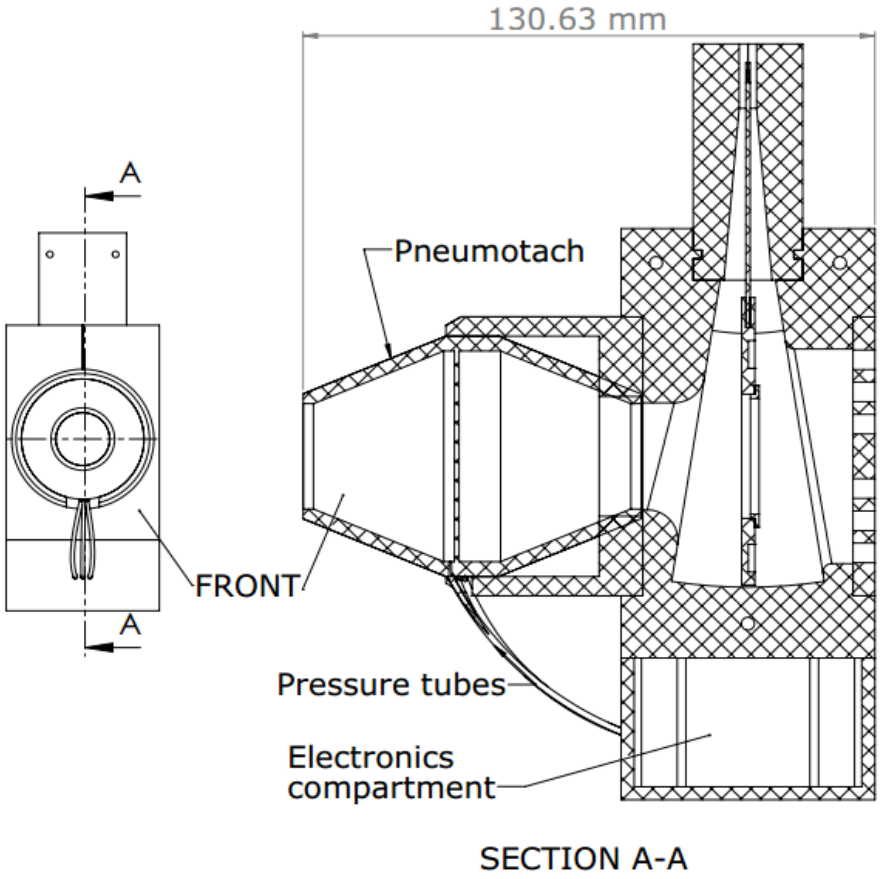

Figure 37. Single frequency prototype 3D model, right plane section view.

Figure 37 shows a section view though the right plane of the 3D model of the prototype. This view shows the pathway of the airflow front to back, the piezoelectric actuator clamped at the top of the whole assembly, the mesh-disk in the middle and the pneumotachometer subassembly attached to the front.

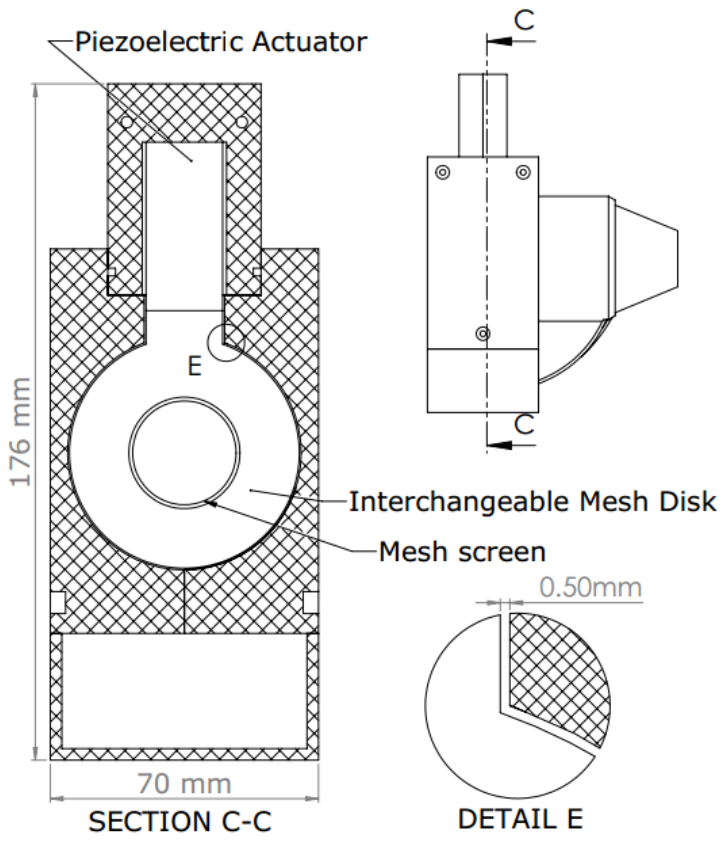

Figure 38. Single frequency prototype 3D model, front plane section view.

Figure 38 shows a section view though the front plane of the 3D model of the prototype. This view better shows the piezoelectric actuator, the mesh-disk in the middle and a detail view on the distance (by design) between the chamber walls and the mesh-disk.

2.5.2.2. Multi-actuator version

The multi-actuator prototype was designed to work below and over the resonance frequency. It was designed with the intention to apply any frequency in the range from 4 Hz to 20 Hz one at a time or combined (in a composite

signal). The prototype would use the small but consistent displacement of the piezoelectric actuators below the resonance frequency and, by means of mechanical amplification, deliver the displacement needed according to Figure 30. However because of the trade-off and loss of force to achieve the large amplitude amplification, the stiffness and force needed to be improved. The design of the multiple-actuator was based in the idea of increasing these two factors by using multiple actuators. Increasing the stiffness using multiple actuators is needed to increase the generated force, necessary to move the required masses (loads) as a result of the displacement amplification. By doing so appropriately, the desired frequencies for the forced oscillations could be designed to be in the range of frequencies either below and/or above the system's resonance frequency.

Two types of amplification methods were considered to implement the multiple actuator approach; simple extension and a lever-linkage.

After a kinetic analysis of how the tip of the actuators would move when joined together, it was concluded that a simple extension type of amplification would not be sufficient. This occurred mainly because of the way the actuators would be linked to each other, as in Figure 39 (A). A beam (or other extension) growing perpendicularly from the linking-beam or cap (cassette) would remain parallel to the Y axis (as shown in Figure 39 (B)) and would not turn in an angle. Therefore, the translation of the beam would only be equivalent to the displacement measured at the tip of the actuators and not really amplified, as opposed to the case of the single actuator with an extension attached to the tip. Figure 39 (B) illustrates the movement of the cassette.

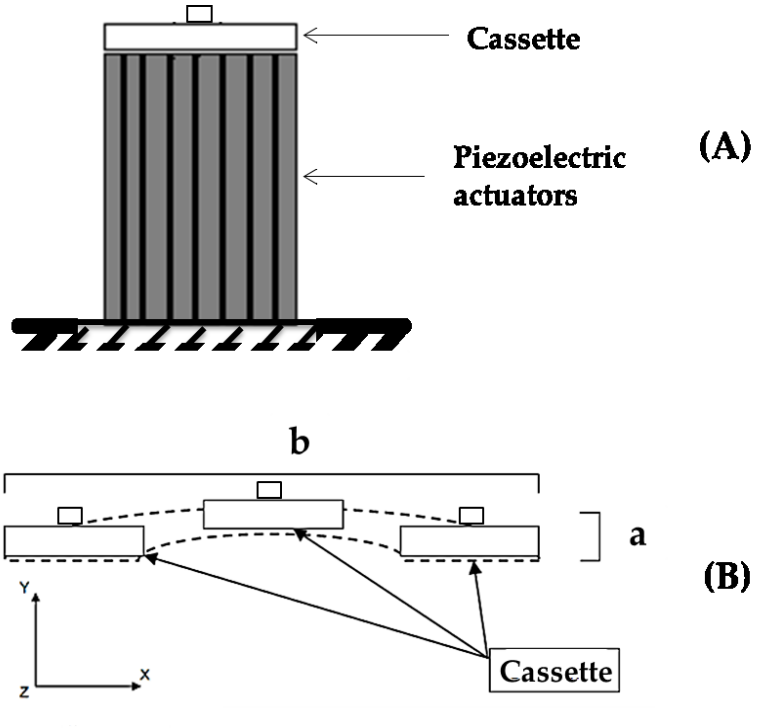

Figure 39. Cassette movement

The design for the displacement mechanism was instead decided to be a lever moved by the cassette as shown in Figure 40. This type of mechanism provides the angular displacement that can be easily amplified by the dimensions. The length of the lever is dependent of the ratio between the distance from the input force to the pivot point and the distance from the output force to the pivot.

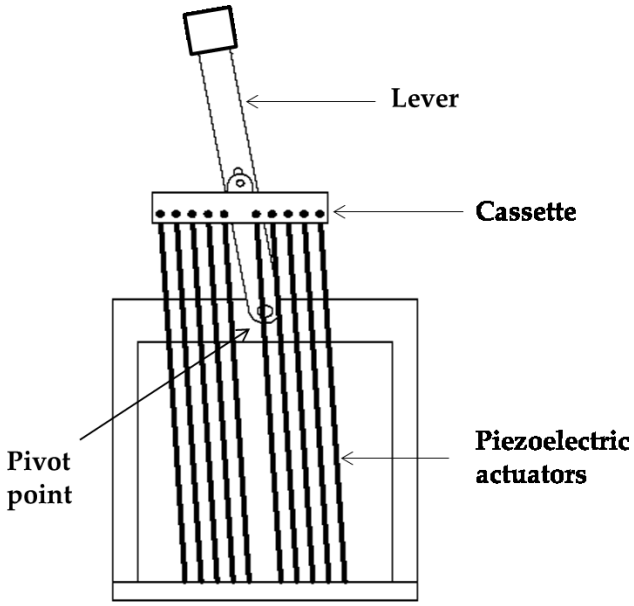

Figure 40. Multi-actuator, lever displacement amplification.

As with the single actuator prototype, the surface area vs. displacement design guide from Figure 30, Equation 22, and Equation 23 were used to design the size of the mesh-disk and determine their inner radius and outer radius. It was also used to determine the lever dimensions. The size of the mesh-disk was selected to be 13082 mm^2 so that the displacement needed at 5 Hz is 2.5 mm. Layers of the 500 threads per inch wire cloth, as used on the other prototypes, would be implemented in this design to adjust the resistance of the mesh-disk to 1 $cmH_2O/l/sec$.

Taking into account the experimental data acquired in Section 2.3.1 for a single actuator loaded at the tip, 0.3 mm of amplitude at the tip of the actuators is expected below the resonance frequency. The output point of the lever would be close to the center of the mesh-disk, and so, the corresponding length of input-to-pivot was set to 1 cm and the output-to-pivot to 17 cm. These

dimensions provide an amplification factor of 17 and a safety factor of 1.56 in terms of the required displacement. Figure 41 shows the 3D model of the designed mesh-disk. Its calculated total mass was 33.81 grams.

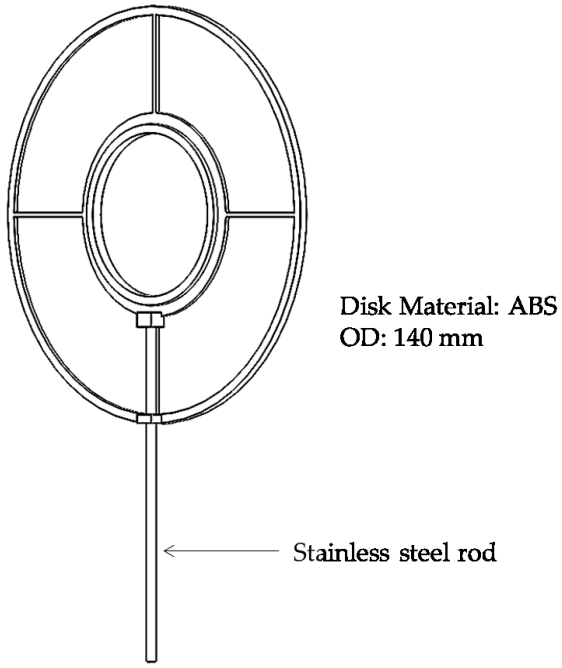

Figure 41. Mesh-disk for the multi-actuator prototype.

Since each actuator is independent (not bonded to one another), they can be considered as parallel springs. Therefore, the effective static stiffness k_f of the system was expected to increase, like the force, by a factor equal to the number of actuators. This was tested by arranging the actuators side by side and one below the other, similarly to the design in Figure 46. Simple layers of plastic were cut and modify to build the system for these tests. The setup shown in Figure 42 was used to measure the displacement at the tip of the actuators after a mass m was hanged from the linking part.

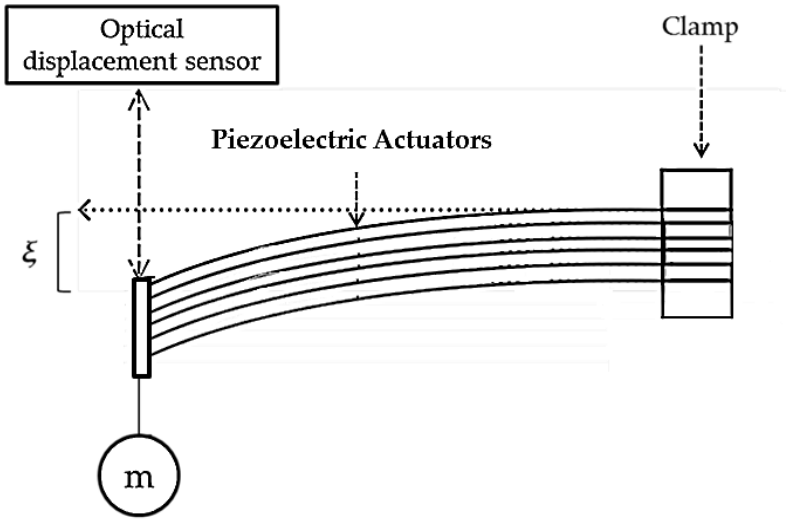

Figure 42. Multiple actuator stiffness measurement set-up.

This test was performed 3 times and the static stiffness calculated as a first estimate of performance as was done with the signal actuator with Equation 8, recognizing that this stiffness will not be representative for the dynamic performance as was described with the single actuator, but will still serve as a comparative reference. Table 11 shows the averaged stiffness for the system with 12 actuators and the a linking plastic part which extended the total length of the equivalent beam by 5 mm.

Table 11. Multiple actuator stiffness measurement results.

Parameter	Value	Uncertainty
Mass at tip [g]	18.6	+/- 0.1
Force calculated [N]	0.18	+/- 0.5%
Displacement ξ [mm]	0.026	+/- 0.015
Calculated stiffness k_f [N/m]	6923.1	+/- 1%

As expected, the stiffness obtained was 14% less than the sum of the stiffness of the 12 actuators. This is attributed to the longer length of the cantilever beam system, extended by the piece of plastic joining the tip of the actuators and the mass hanging at the end of this distance (as the length of the beam affects the stiffness, see Equation 7). The experimentally determined stiffness was sufficient for moving on to the design and tests for the multi-actuator system.

Dynamic tests for this multiple actuator arrangement were not done at this point since the bond between the plastic part connecting the actuators in this setup was not strong enough to allow this kind of test. However, I tried another approach to come up with a predicted dynamic stiffness, and use this value to predict the frequency response behaviour including resonance frequency. Assuming that a similar difference factor found with the single actuator between the static stiffness and the dynamic stiffness (of 2.15) might also occur in this configuration, the expected dynamic stiffness was estimated from the measured static stiffness and then an equivalent E could possibly be roughly estimated using Equation 9 which accounted for rotational inertia of an actuator loaded with a mass at the tip, see Table 12.

Table 12. Multiple actuator dynamic stiffness.

Parameter	Value	Uncertainty
Expected dynamic stiffness k_{dm} [N/m]	3218.9	+/- 1%
I [mm^4]	6.6	+/- 0.08%
L [mm]	55	+/- 0.02%
E [N/m]	2.46x10^10	+/- 1.14%

Following the theory used in the first method used to estimate the resonance frequency in the design of single-actuator prototype, Figure 44 shows the expected theoretical ω_n using Equation 11 considering the damping coefficient

negligible, and *L* to be the distance from the center of mass of the mesh-disk and the pivot point of the lever as shown in Figure 43 (center of mass calculated from 3D model in Solidworks®).

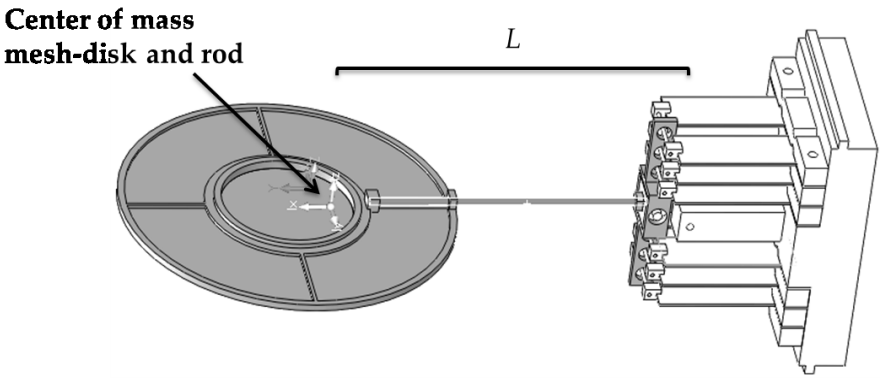

Figure 43. Center of mass and distance to pivot point.

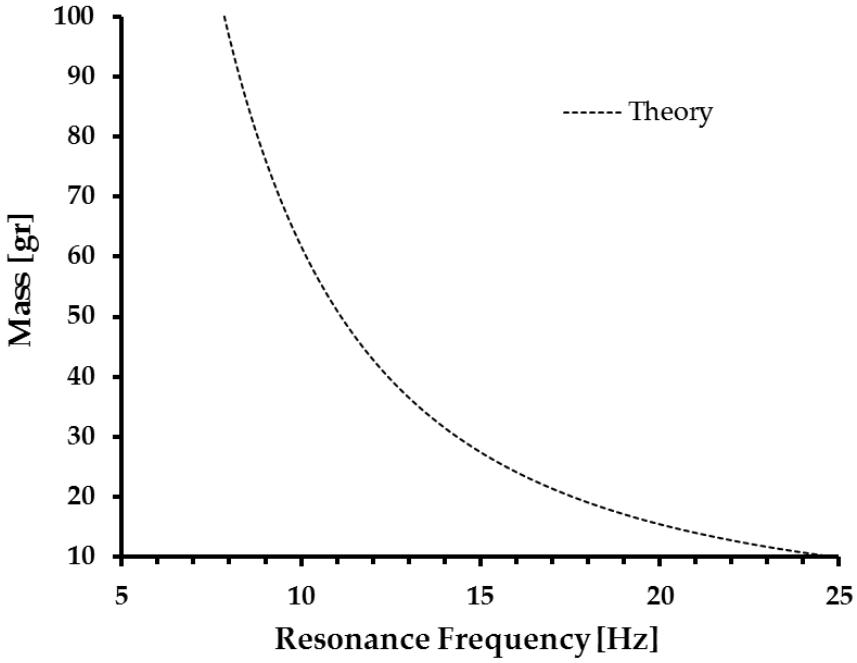

Figure 44. Mass at the tip of the actuators vs. theoretical resonance frequency

According to these calculations, for the mass of the mesh-disk (of 33.81 grams) it is expected that the system would have a resonance frequency of 13 Hz for a type of prototype in which the resonance frequency falls in between the desired range for low frequency FOT (4 to 20 Hz). However, this method doesn't account for the expected large rotational inertia of the large mesh disk. That is the approximation as a point mass is not valid for this larger mesh compared with the signle actuator model. Therefore, the resonance frequency was also estimated considering the system as an inverted compound physical pendulum and analysing it taking into account the rotational inertia of all of the system elements.

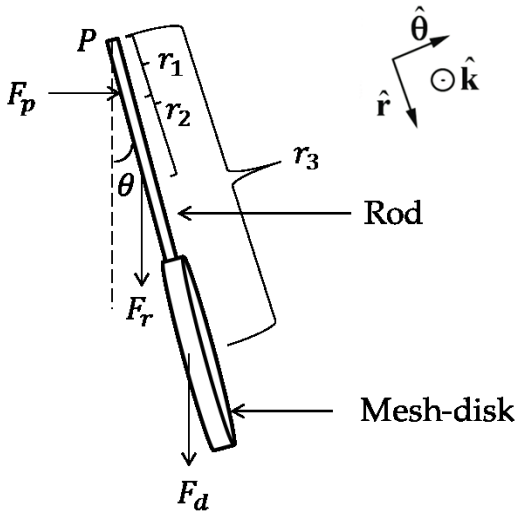

Figure 45. Force diagram of system.

Figure 25 shows free body force diagram of the system. In this figure $\hat{k}$ is the normal plane of motion, θ is an angle such that counter clockwise rotation is a positive z-component of the angular velocity and therefore, a torque pointing out of the page has a positive z-component. The pendulum undergoes fixed axis rotation about point P. The force from the piezoelectric actuators F_p act as at

distance r_1 where the linking beam connecting all the actuators makes contact with the rod. The gravitational force acts at the center of mass of the rod F_r at distance r_2. Considering the mesh disk as a separate body, the gravitational force acts as well on the center of mass of the mesh-disk at distance r_3. The torque about point P is given by:

$$\tau_p = r_1 \cdot F_p \cos\theta - r_2 \cdot F_r \sin\theta - r_3 \cdot F_d \sin\theta$$

Equation 29

Since the angle θ is small (maximum angle is 9°), sin(θ) can be assumed to be equal to 0 and cos(θ) to be 1. Then the torque can be considered as the one created by the force of the piezoelectric actuators assembly at r_1:

$$\tau_p = r_1 \cdot F_p$$

Equation 30

where F_p is expressed as Equation 8 for the stiffness of the actuators and the displacement they generate as:

$$F_p = k_{dm} x$$

Equation 31

And the angular frequency (resonance frequency) can be expressed as:

$$\omega_n = \frac{1}{2\pi}\sqrt{\frac{r_1 \cdot k_d \cdot x}{I_p}}$$

Equation 32

where I_P is the moment of inertia about the pivot point P. For simplification, I_P can be considered as the sum of moments of inertia of the rod and the mesh-disk and the actuators assembly:

$$I_P = I_{P,rod} + I_{P,disc} + I_{P,act}$$

Equation 33

where $I_{P,rod}$ is the moment of inertia of the rod, $I_{P,disc}$ is the moment of inertia of the of the mesh-disk and $I_{P,act}$ is the moment of inertia of the actuators assembly, all about the point P applying the parallel axis theorem.

Using the 3D model of the system, I_P was computed in Solidworks®. The results are shown in Table 13.

Table 13. Moment of inertia, multi-actuator prototype.

Parameter	Value [g · mm²]
$I_{P,rod}$	37743
$I_{P,disc}$	557700
$I_{P,act}$	16090
I_P	611533

The resonance frequency was obtained using **Error! Reference source not found.** with the parameters shown in Table 14. The calculation was made by setting the displacement (amplitude) at the tip of the actuators to be 1.6 mm

(the maximum in this prototype) and estimated dynamic stiffness from Table 12.

Table 14. Resonance frequency of multi-actuator prototype.

Parameter	Value
x [mm]	1.6
Estimated k_{dm} [g・mm/s^2/mm]	3218900
r_1[mm]	10
I_P [g・mm^2]	611533
Estimated ω_n [Hz]	1.5

From this analysis it can be seen the effect of the large effect of the moment of inertia of the rod and disk-mesh. The estimated resonance frequency by this method is lower by a factor of 8.6 compared to the point mass approximation approach, necessitating this method for design.

In this case, a system with a resonance frequency at 1.5 Hz allows for a prototype running over the resonance frequency as described in page 49.

The multi-actuator motor was designed then to be able to work with 12 actuators as shown in Figure 46.

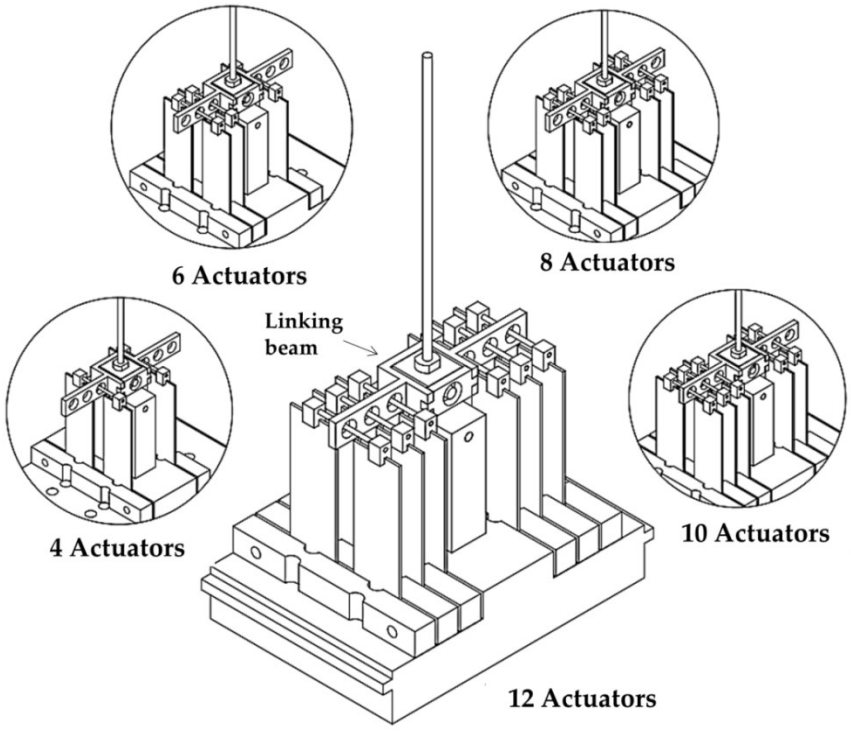

Figure 46. Multiple-Actuator motor.

Figure 47 shows a closer look to the linking-beam and its components. The linking-beam was joined to the tip of the actuators by ball bearings (ball bearings A). The top of the actuators were joined in pairs by a shaft which passed through the inner orifice of the ball bearing A embedded in the linking-beam. In the case of the of the lever rod, the linking-beam was joined to it by a moving part holding a sleeve bearing (sleeve bearing holder). The sleeve bearing holder part was connected to the linking-beam by a pair of ball bearings (ball bearings B) that allowed it to rotate on the z axis. The sleeve bearing embedded in the sleeve bearing holder (better shown in section view Figure 48) allowed the ball bearing elbow joint to slide in order to allow the displacement on the y axis of the linking-beam (illustrated in Figure 49).

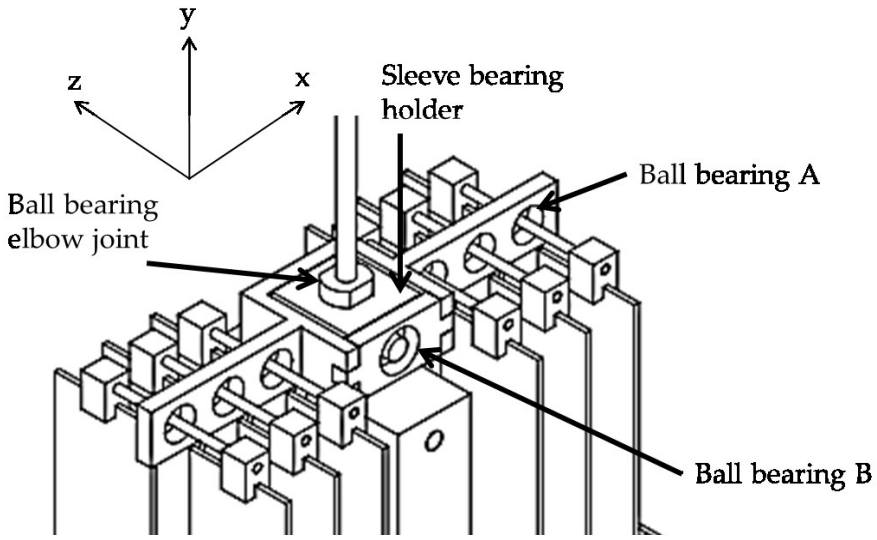

Figure 47. Linking-beam components.

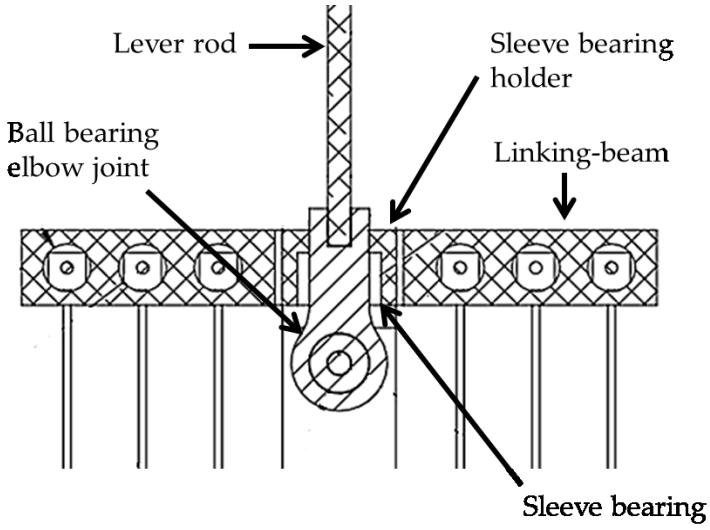

Figure 48. Detail view of linkage mechanism

Figure 49 shows a side view of the motor on its resting position (image to the right) and motor moving the lever rod to its maximum capacity towards one side (image on the left). It also shows the displacement of the linking-beam with

respect to the bottom of the motor and with respect to the ball bearing elbow joint.

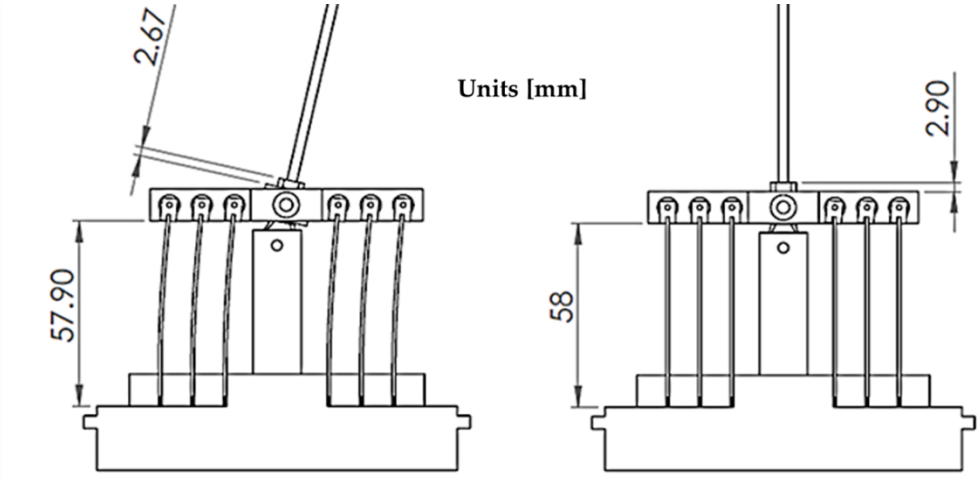

Figure 49. Multi-actuator prototype motor movement.

Considering the leak around the mesh-disk, the device was designed to have a gap between the mesh disk and the surrounding wall of 0.7 mm (Detail C, Figure 35), like the single-actuator prototype. However, the gap was increased by 0.2 mm to allow more clearance. More play around the mesh-disk was needed since error in the positioning of the input force point was also amplified at the output. The decrement in leak resistance as a consequence of the gap would be compensated by the use of more than one layer of wire mesh cloth to increase the resistance.

The following are figures that show the 3D model made for this prototype:

Figure 50 shows an isometric view of the prototype assembled with two of the parts that form the chamber removed.

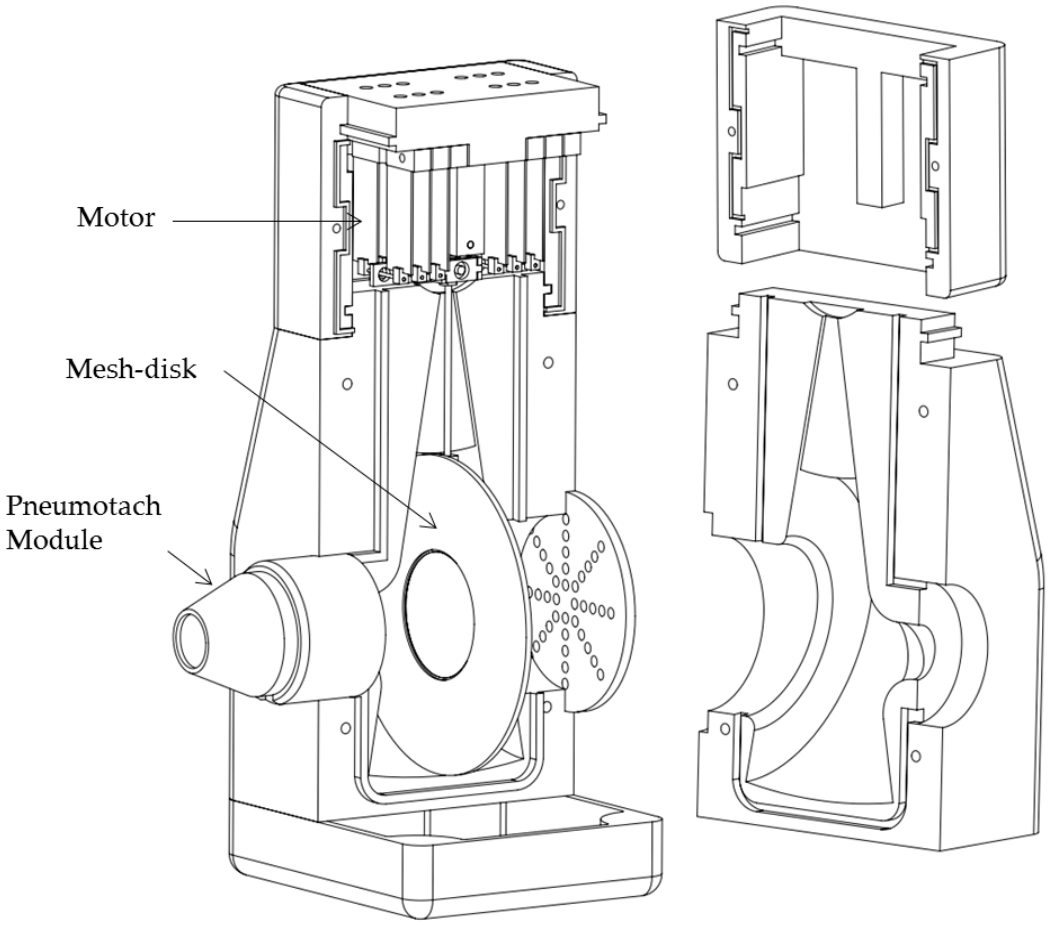

Figure 50. Isometric of the assembled 3D model of the Multiple Actuator Prototype.

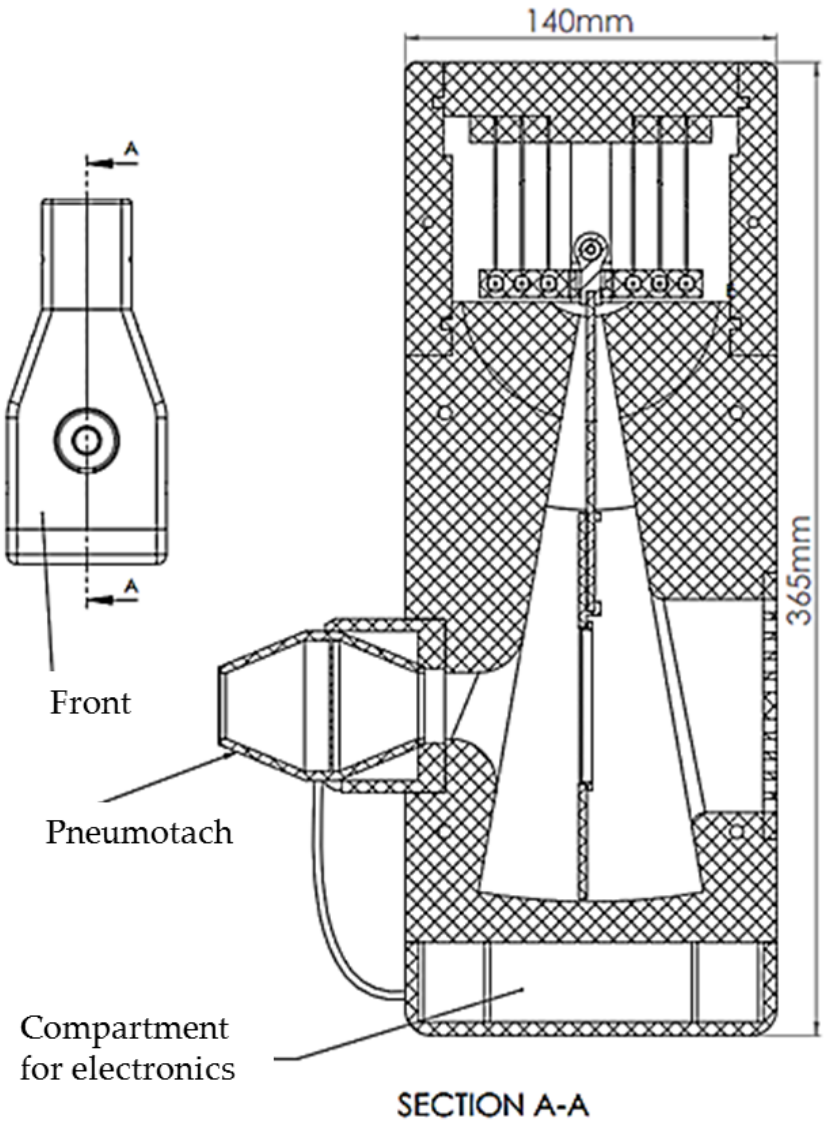

Figure 51. Multiple Actuator prototype 3D model, right plane section.

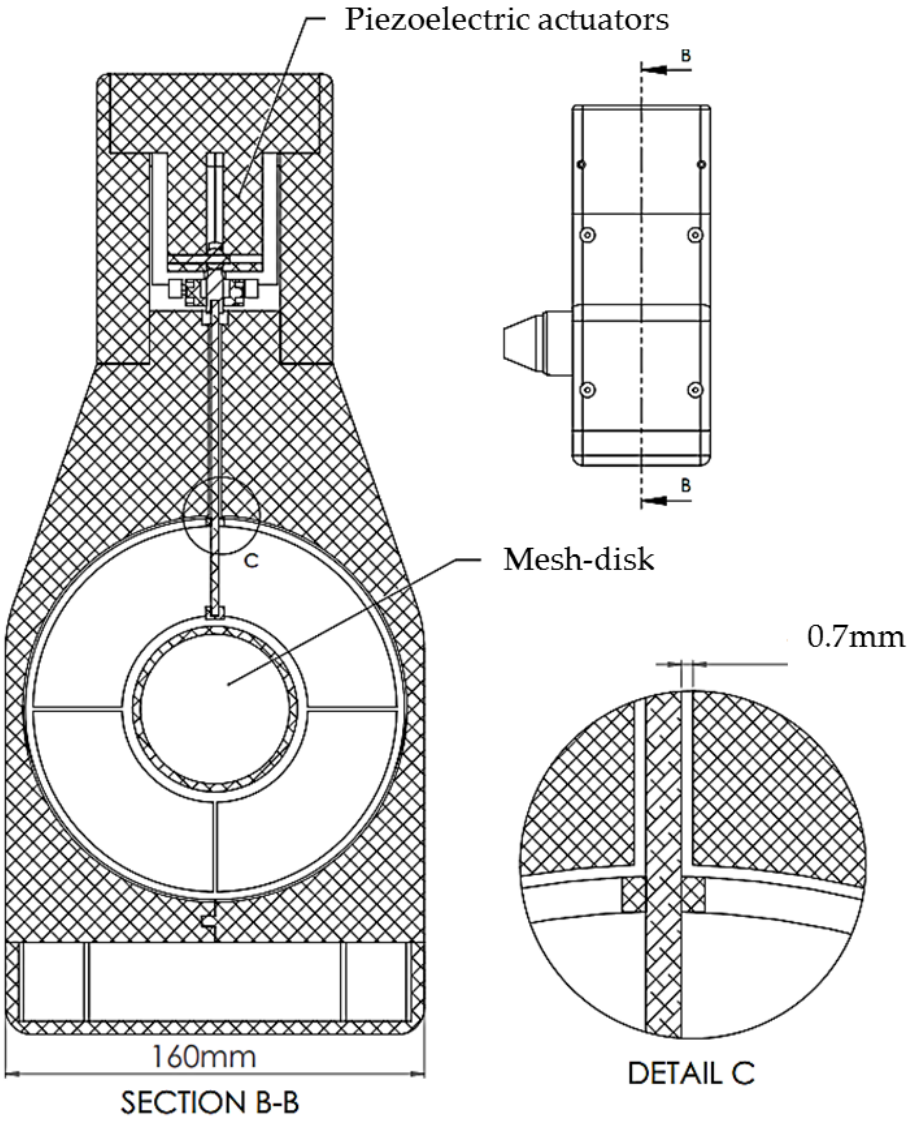

Figure 52. Multi actuator prototype 3D model, view front plane section view.

CHAPTER 3: PROTOTYPES TESTING AND RESULTS

3.1. Introduction

This chapter describes the methods and results of the tests performed on the two prototypes designed following the recommendations in the literature; The Single-actuator and the Multi-actuator prototypes. The chapter is divided into 2 sections dedicated to each of the two prototypes.

After having the parts manufactured and receiving them, the prototypes were assembled. The mechanisms were briefly tested during assembly to verify that they functioned according to design. After being fully assembled and adjusted, the tests on the prototypes aimed at assessing their performance in terms of displacement, frequency response, pressure and flow generation, and impedance measurement. Data from a technologically similar device in the market, the tremoFlo™, including SNR calculations were used to compare to the level of performance achieved by the prototypes.

3.2. Single-actuator prototype

3.2.1. Preparation

The first thing done to prepare the prototype for testing was to adjust the mesh-disks in order to minimize the leak around them and get the desired resistance to flow from the mesh in the middle of them.

As mention in the design section 2.5.2.1, layers of Kapton® tape with a specified thickness of 0.025mm were applied around the edges of the disks. The layers

were applied one by one testing the motion of the disk inside the chamber after each layer until friction was noticed. In the case of the brass mesh-disk, 2 layers were applied, and in the case of the ABS mesh-disk, 1 layer was applied.

Since the mesh in the pneumotach module has a resistance of 0.4 $cmH_2O/l/sec$ ±3% and the recommended maximum total resistance of the device is 1.02 $cmH_2O/l/sec$ for FOT frequencies of 5Hz or less, the brass mesh-disk (aimed at a frequency equal or close to 5Hz) resistance was tuned so that the total resistance (from Equation 21) of the prototype was close to 0.6 $cmH_2O/l/sec$.

In order to measure the resistance of the meshes and the whole prototype, the set-up shown in Figure 21 and a flow of 1 l/sec was used. In this set-up, the "adapter to mount mesh" was changed to fit the mesh-disks and also replaced by the prototype itself.

For the brass mesh-disk, one layer of wire cloth was used. The resistance measured of the mesh-disk was 1.53cm $cmH_2O/l/sec$ ±3%. After placing the mesh-disk inside the prototype, the resistance measured across the prototype (without the pneumotach module) was 0.57 $cmH_2O/l/sec$ ±3%. This means that (using Equation 21) the leak around the mesh-disk was 0.91 $cmH_2O/l/sec$ ±9%.

The testing set-up for the prototype was similar to the one shown in Figure 25. The equipment used was the same but in this case, the section before the pneumotach module was changed in order to measure different calibrated test load (TL) resistances and also introduce a simulated respiration noise during some tests.

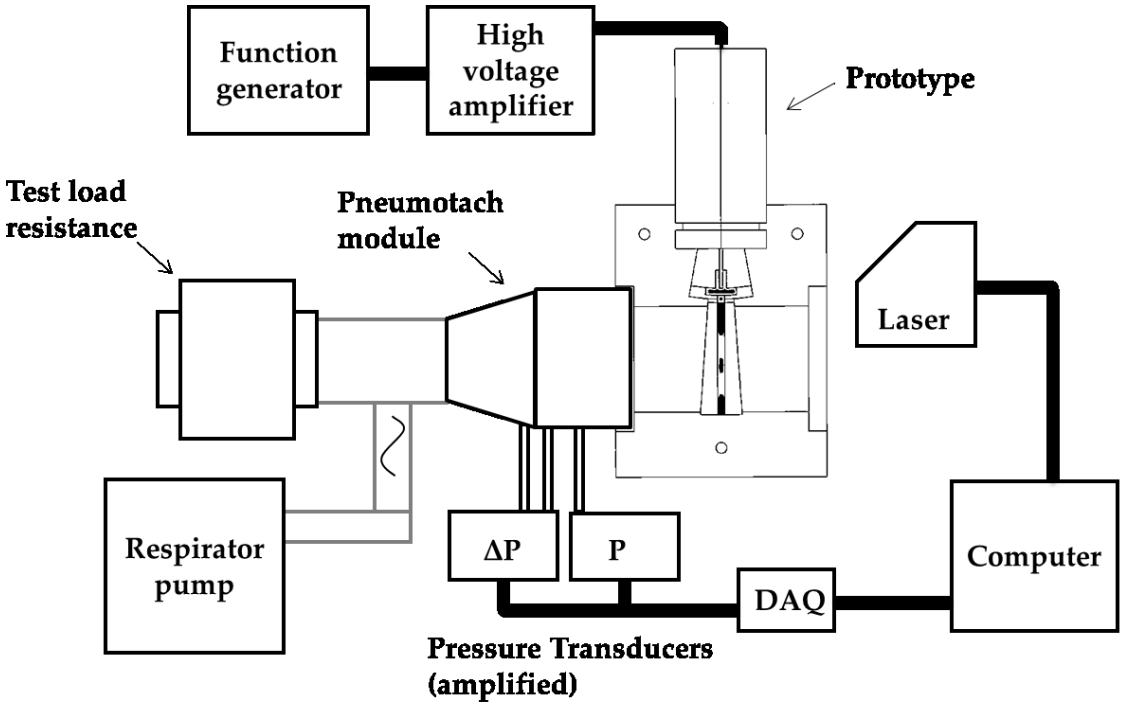

Figure 53. Testing set-up for prototypes.

When conducting the tests, the piezoelectric actuator was always driven at the maximum AC amplitude recommended by the manufacturer (50 Volts p-p). The displacement of the mesh-disks was measured by the laser displacement sensor kit pointing at the center of the mesh-disk. Pressure and flow were measured using the pneumotach module described in section 2.4 connected to the differential pressure transducers. The uncertainties of the measurements coming from the equipment are listed in Table 15. The uncertainties were calculated as the specified equipment accuracy multiplied by the calibration coefficient.

Table 15. Measurement uncertainties.

Parameter	Uncertainty (from equipment)
Displacement[mm]	±0.072
Pressure[cmH_2O]	±0.009
Flow[l/sec]	±0.010

A program using LABVIEW® was made to collect the data through the acquisition card at sample rate of 1000 samples/sec. Figure 54 shows a picture of the actual prototype being tested.

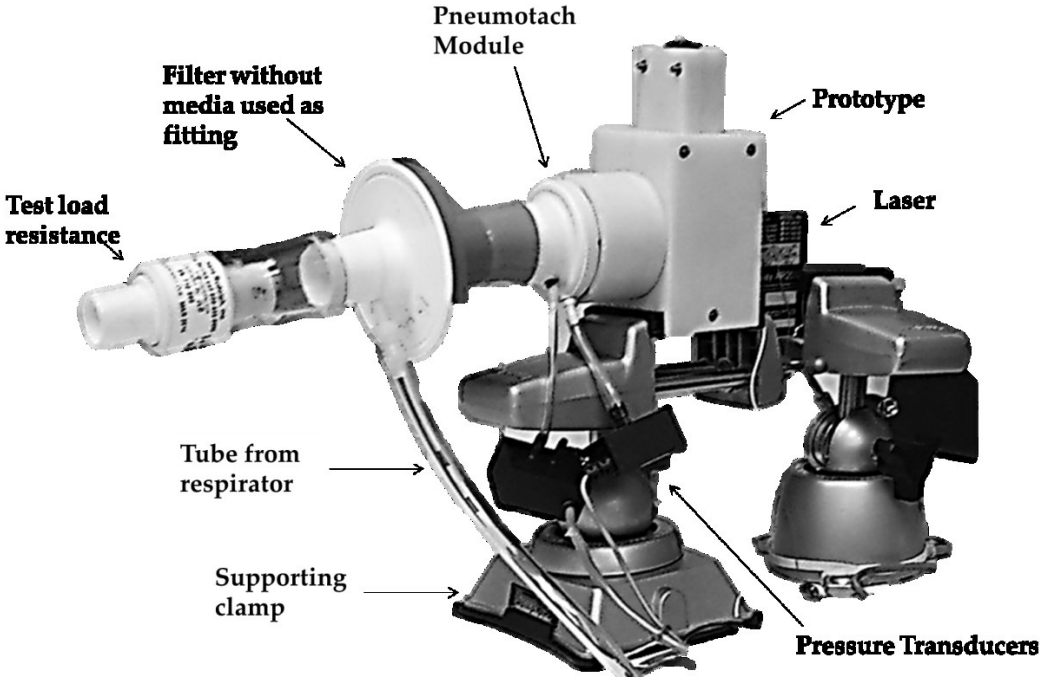

Figure 54. Single actuator prototype being tested

3.2.2. Performance tests

The following sections will show the performance tests performed on the prototype with each mesh-disk separately. The heavy brass mesh-disk was assigned the name of Low frequency mesh-disk, and the lighter ABS mesh-disk the name of High frequency mesh-disk.

3.2.2.1. Low frequency mesh-disk

To evaluate the performance of this configuration of the prototype, tests to determine its frequency response as well as the displacement, pressure, and flow achieved at resonance frequency against different TL resistances were made.

The frequency response test was performed by stimulating the system with frequencies from 0.5Hz to 20Hz in steps of 1 Hz and duration of 10 seconds each, against no TL resistance (open) and no induced respiration noise. Figure 55 shows the results of this test. The line in between the data points in this plot was made by a smoothing spline with a parameter p=0.99 for better visualization.

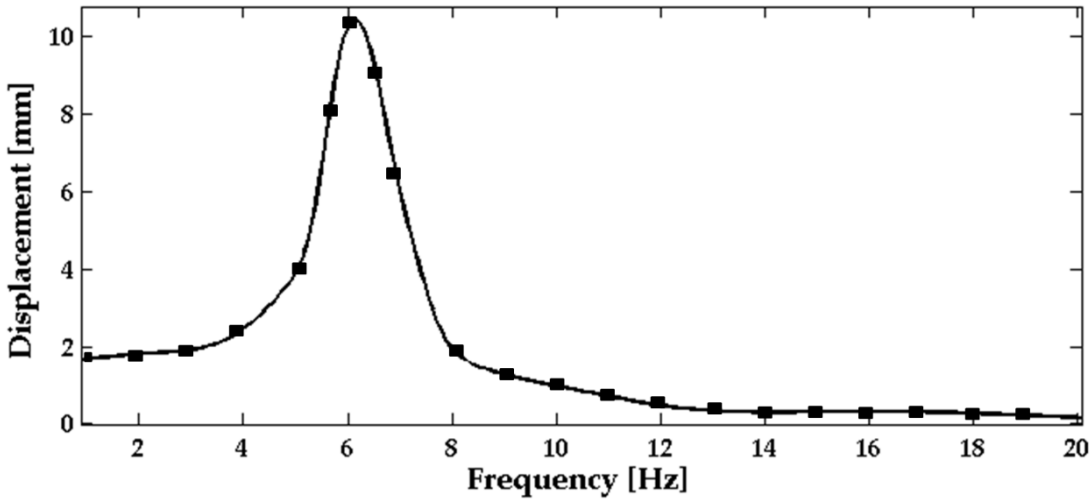

Figure 55. Frequency response, single-actuator prototype with low frequency mesh-disk.

This figure shows that the resonance frequency of the system was 6.2 Hz. Compared to the calculations in Section 2.5.2.1 (page 74) for this mesh-disk, the resonance frequency was predicted (5 Hz, and 7.1 Hz) reasonably accurately

(within 16% error from both approaches). A contributing factor in the divergence is that the manufactured disk had an actual mass of 75.6 g, 5% less than design.

The next set of tests was performed stimulating the actuator at resonance frequency (at 6Hz for practicality) and without induced respirator noise. Each test was performed for 20 seconds, 3 times. The acquired data was filtered by a Butterworth level 10 band pass filter with cut-off frequencies of 2Hz and 10Hz.

First, the prototype was tested against no TL resistance in order to determine the maximum displacement, minimum pressure and maximum flow it could produce. The following images show examples in the time domain and frequency domain (using the Fast Fourier Transform (FFT)) of the displacement (Figure 56), pressure (Figure 57), and flow (Figure 58) data recorded in one of the tests.

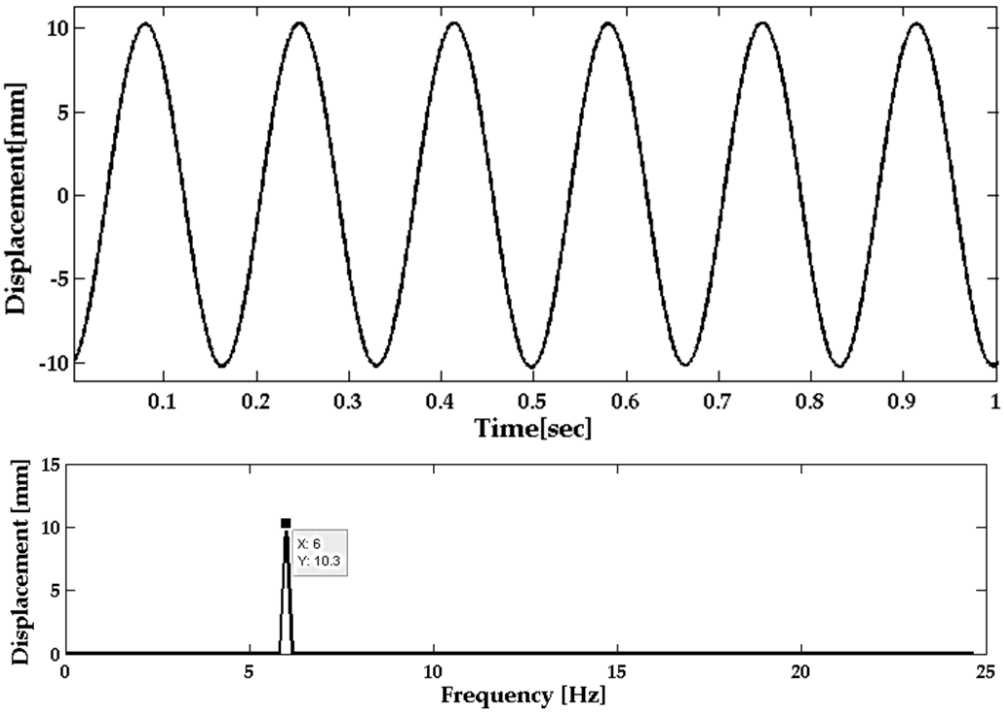

Figure 56. Single actuator prototype, low frequency mesh-disk, maximum displacement.

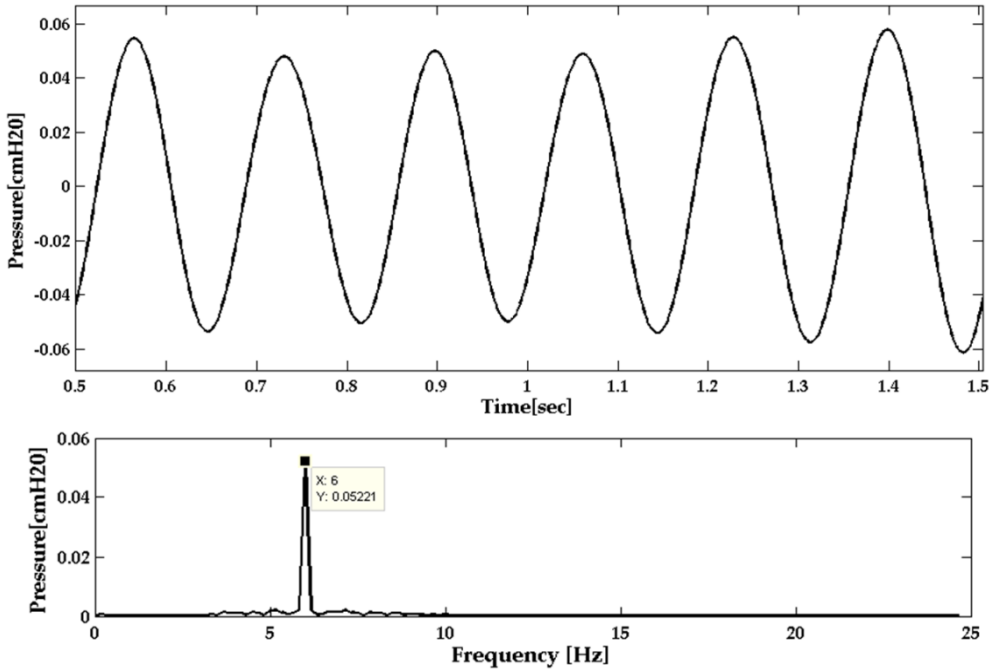

Figure 57. Single actuator prototype, low frequency mesh-disk, minimum pressure.

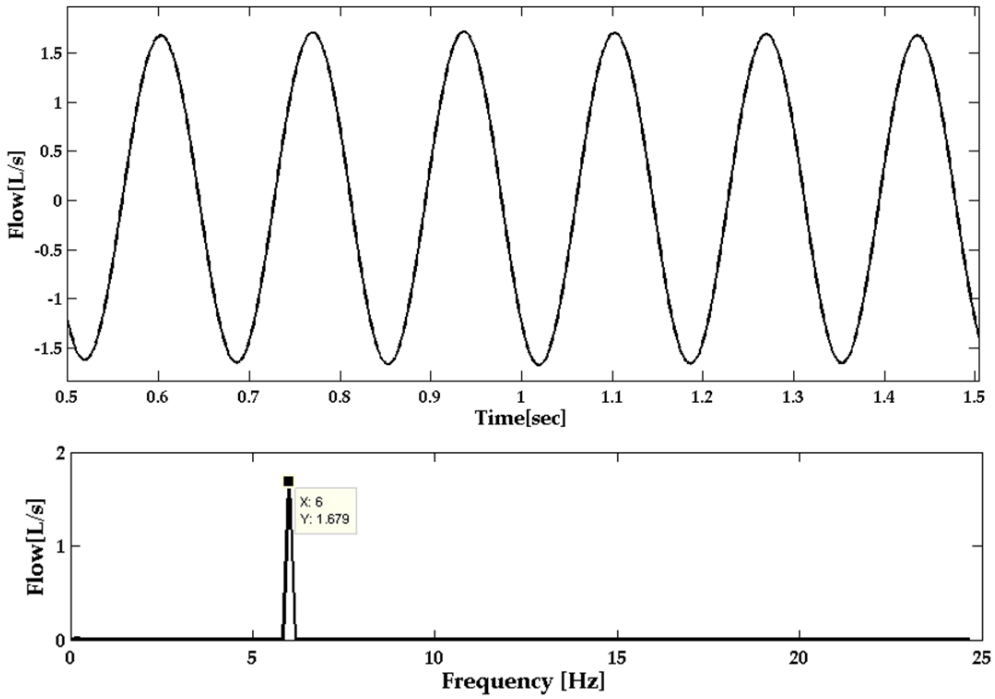

Figure 58. Single actuator prototype, low frequency mesh-disk, maximum flow.

The maximum average amplitude for displacement, pressure and flow measured are shown in Table 16. The calculations were made by taking the peaks of the signal on all the recordings and then averaging them using MatLab®. The signal to noise ratios and impedance values (see Equation 3) of each test were calculated using Bhatawadekar et al's MatLab® algorithms, which calculate the SNR based on the ratio of the peak at the signal frequency divided by the average of the magnitude in two 1 Hz bands located at least 1.5 Hz to either side of the signal frequency peak. [74].

Table 16. Single-actuator prototype with low frequency mesh-disk. Performance against no resistance.

Parameter	Ave. Max. Amp.	Std. Dev.	Ave. SNR [dB]	Std. Dev. SNR [dB]
Displacement[mm]	10.343	0.053	49.30	0.10
Pressure [cmH_2O]	0.053	0.005	35.05	0.05
Flow [l/sec]	1.683	0.018	49.33	0.07

Tests of the prototype against TL resistance of 1, 2, 5 and 15cmH_2O/l/sec (values measured at 5 liters/sec) were performed. These TLs act as the resistance of the airways, where the 2 cmH_2O/l/sec represents the normal resistance of healthy adult patients and 5 and 15 cmH_2O/l/sec represent adult patients with some airflow obstruction, as explained in section 1.3 and illustrated in Figure 1. The higher the resistance value of the TL, the more challenging it is to measure it. This is due to the lower flows through high impedance TLs. Also, as the TL resistance in the forward direction increases, the more air flows (towards the back) through the actuator mesh screen and the gap in between the mesh-disk and the chamber since this path is mechanically in parallel to the TL, and offers a path of less resistance.

These tests were performed by the same methods as the tests against no TL resistance. The results for the tests on the 1, 2 and 5 $cmH_2O/l/sec$ TLs are presented below in Table 17. The average impedance values *R* and *X* and the standard deviation among the 3 tests are presented in Table 18.

Table 17. Single-actuator prototype with low frequency mesh-disk. Performance against 1, 2, and 5 $cmH_2O/l/sec$ resistances.

Resistance [$cmH_2O/l/sec$]	Parameter	Ave. Max. Amp.	Std. Dev.	Ave. SNR [dB]	Std. Dev. SNR [dB]
1	Displacement[mm]	10.266	0.186	49.63	0.51
	Pressure [cmH_2O]	0.797	0.008	49.28	0.06
	Flow [l/sec]	0.819	0.018	46.66	0.44
2	Displacement[mm]	10.024	0.225	49.09	0.56
	Pressure [cmH_2O]	0.846	0.005	44.58	0.12
	Flow [l/sec]	0.606	0.013	41.51	0.40
5	Displacement[mm]	11.178	0.252	50.18	0.59
	Pressure [cmH_2O]	1.127	0.006	45.00	0.17
	Flow [l/sec]	0.314	0.020	38.35	0.48

Table 18. Single-actuator prototype with low frequency mesh-disk. Impedance values against 1, 2, and 5 $cmH_2O/l/sec$ resistances.

Resistance [$cmH_2O/l/sec$]	Parameter [$cmH_2O/l/sec$]	Average	Std. Dev.
1	*R*	1.46	0.01
	X	0.21	0.01
2	*R*	1.77	0.01
	X	0.10	0.02
5	*R*	3.40	0.02
	X	0.11	0.02

The results for the tests against the most difficult TL resistance, the 15cmH_2O/l/sec, are presented in more detail. The following images show examples in the time domain and frequency domain of the displacement (Figure 56), pressure (Figure 57), and flow (Figure 58) data recorded in one of the tests.

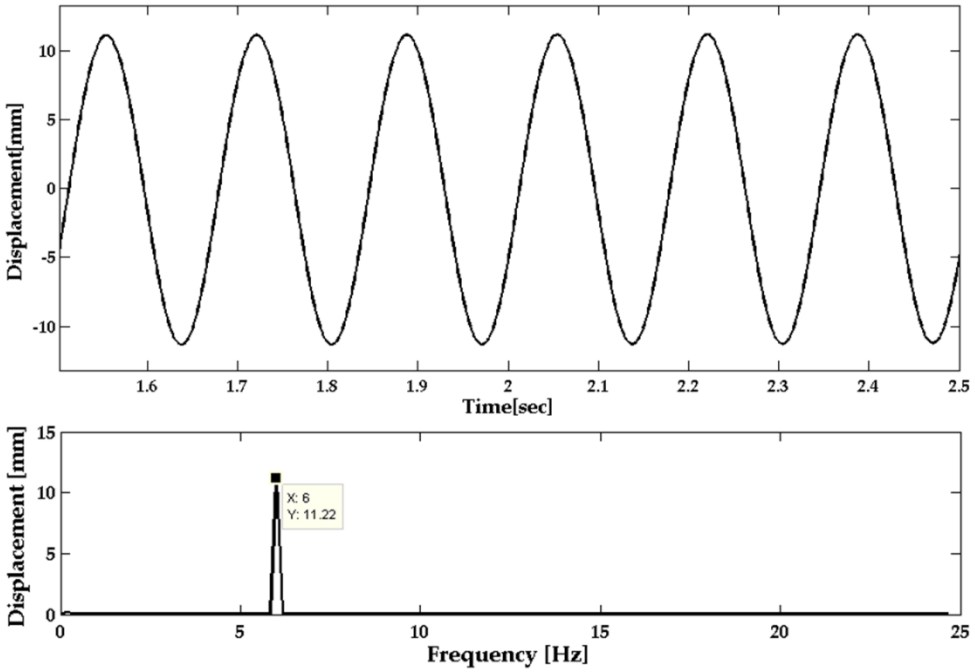

Figure 59. Single actuator prototype, low frequency mesh-disk, displacement against 15 cmH_2O/l/sec.

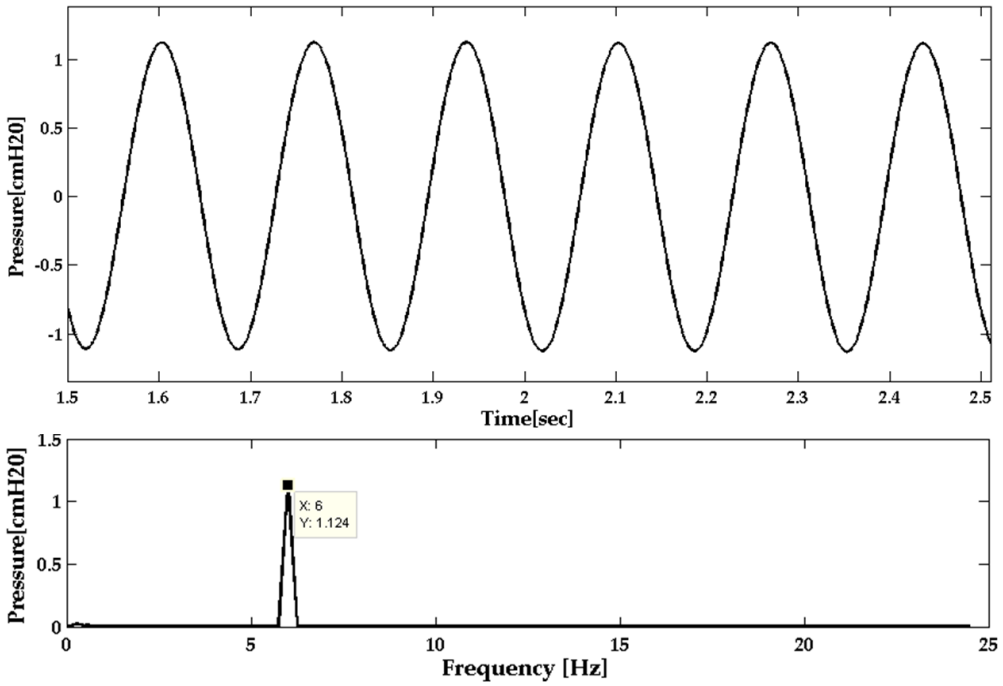

Figure 60. Single actuator prototype, low frequency mesh-disk, pressure against 15 $cmH_2O/l/sec$.

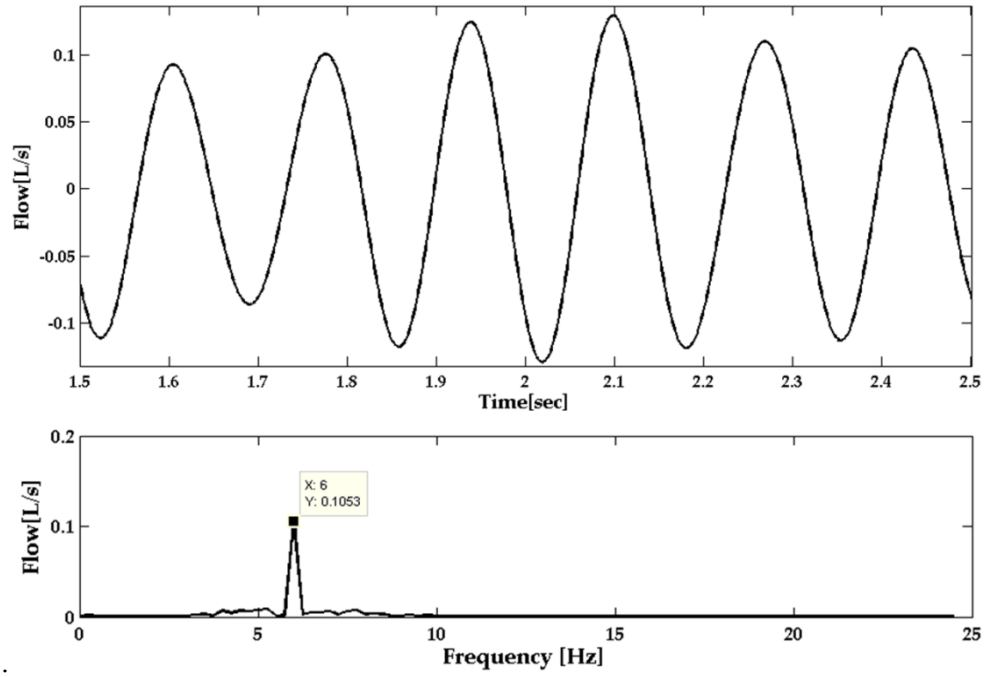

.

Figure 61. Single actuator prototype, low frequency mesh-disk, flow against 15 $cmH_2O/l/sec$.

The maximum average amplitude for displacement, pressure and flow measured are shown in Table 19. The average impedance values *R* and *X* and the standard deviation among the 3 tests are presented in Table 20.

Table 19. Single-actuator prototype with low frequency mesh-disk. Performance against 15 $cmH_2O/l/sec$ resistance.

Parameter	Ave. Max. Amp.	Std. Dev.	Ave. SNR [dB]	Std. Dev. SNR (dB)
Displacement[mm]	11.223	0.157	48.57	0.48
Pressure [cmH_2O]	1.1240	0.017	51.83	0.42
Flow [l/sec]	0.1062	0.018	31.90	0.43

Table 20. Single-actuator prototype with low frequency mesh-disk. Impedance values against 15 $cmH_2O/l/sec$ resistance.

Resistance [$cmH_2O/l/sec$]	Parameter [$cmH_2O/l/sec$]	Average	Std. Dev.
15	*R*	7.93	0.03
	X	0.10	0.04

From these performance results so far, it can be seen that the measurements of displacement, and most importantly, pressure and flow, have high SNR. All measurements have a SNR above 30dB, even the flow measurements against the highest resistance. This 30dB of SNR threshold reference was obtained from consulting the mechanical engineer and lead designer of the tremoFlo™ Guy Drapeau at the company Thorasys Inc. This topic will be revisited in section 3.2.3.

From the impedance calculation results, it can be seen that the prototype was consistent on both values R and X. It is important to note, that the impedance measured directly from the ratio of pressure to flow will not be the TL

impedance, but is the impedance of the TL in parallel with any impedance path to atmosphere which is dominated by the flow path via the oscillating mesh and air-gap. Additionally, the resistance to air flow through a mesh is flow dependant. A simple way to correct for the parallel path and its flow dependent behavior is to use a correction function, or calibration curve [75]. The measurements are then corrected as follows. By comparing the measured value of impedance to the respective reference values, as shown in Figure 62, it is possible to obtain a calibration curve.

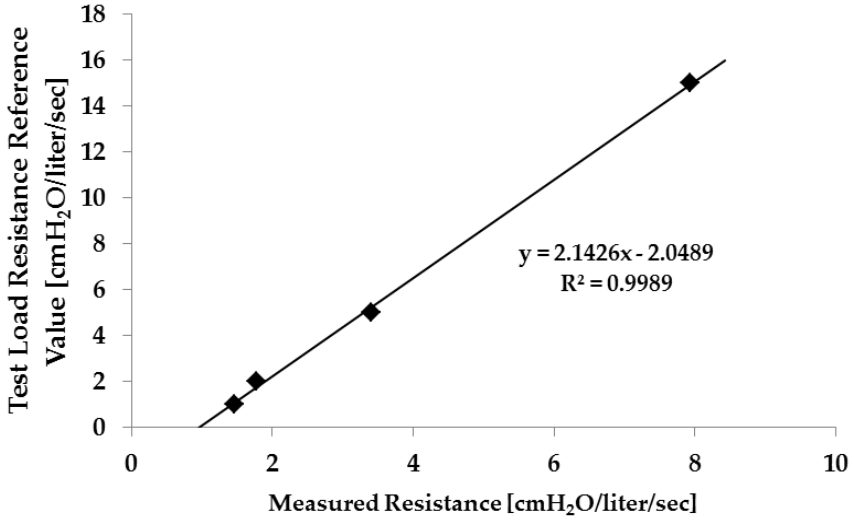

Figure 62. Resistance correction function, low frequency configuration.

The tests that are presented next were performed using the respirator pump to introduce simulated breathing noise. The pump was set at 18 cycles/min and stroke of 600ml/stroke (1200ml/cycle). And the prototype was tested against TL resistances of 2, 5 and 15 $cmH_2O/l/sec$. Each test was performed for 20 seconds, 3 times. The acquired data was filtered by a 10^{th} order Butterworth low pass filter with a cut-off frequency of 10Hz to show the effect of the breathing noise in the example images. Separately, the data was filtered by a 10^{th} order

Butterworth band pass filter with cut-off frequencies of 2Hz and 10Hz before doing the impedance calculations.

Figure 63, Figure 64, Figure 65, show examples in the time domain and frequency domain of the displacement, pressure, and flow respectably of the data recorded in one of the tests against the 2 $cmH_2O/l/sec$ TL.

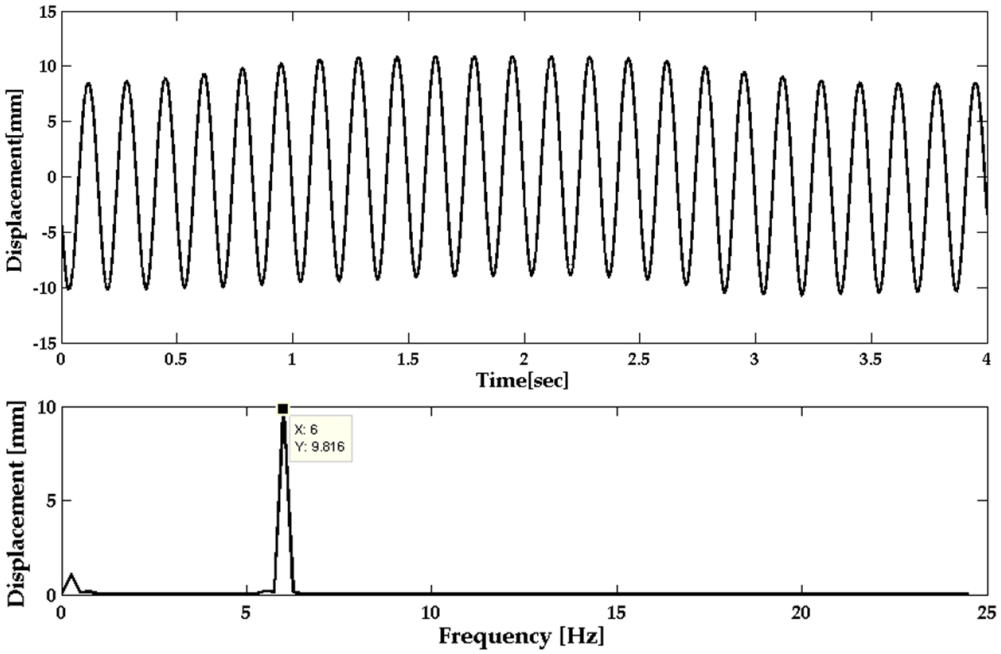

Figure 63. Single actuator prototype, low frequency mesh-disk, displacement against 2 $cmH_2O/l/sec$ with one cycle of breathing noise.

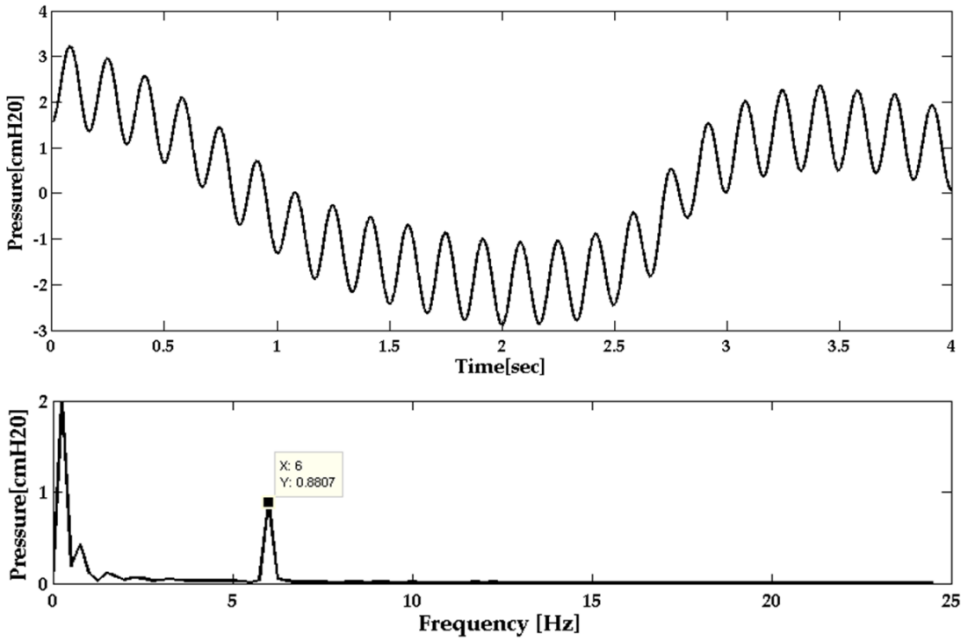

Figure 64. Single actuator prototype, low frequency mesh-disk, pressure against 5 cmH_2O/l/sec with breathing noise.

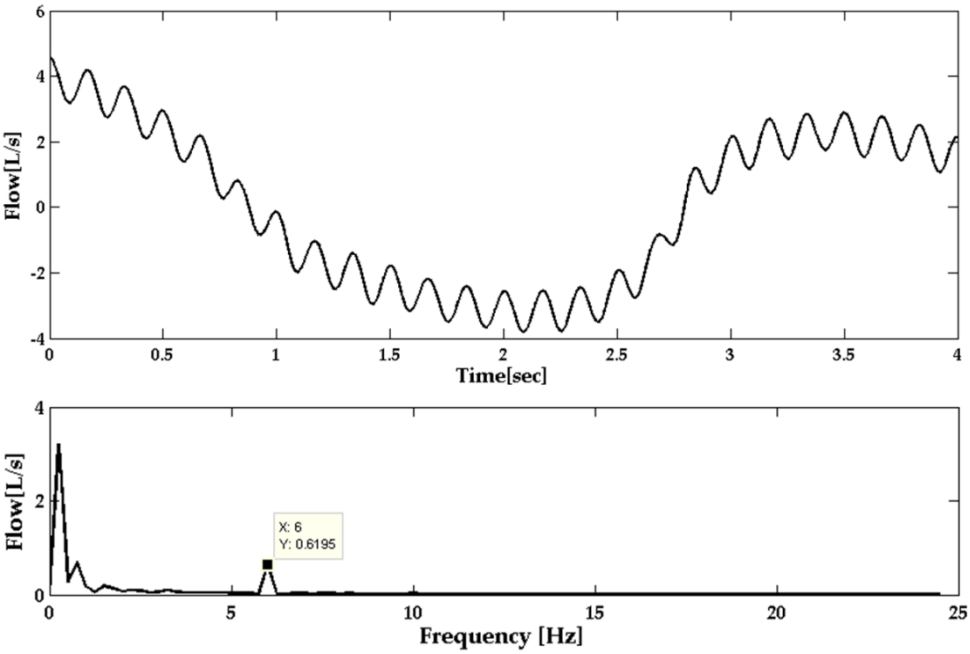

Figure 65. Single actuator prototype, low frequency mesh-disk, flow against 15 cmH_2O/l/sec with breathing noise.

The results for these tests are presented below in Table 21. The average impedance values *R* and *X* and the standard deviation among the 3 tests are presented in Table 22.

Table 21. Single-actuator prototype with low frequency mesh-disk. Performance against 2, 5, and 15 $cmH_2O/l/sec$ resistances with breathing noise.

Resistance [$cmH_2O/l/sec$]	Parameter	Ave. Max. Amp.	Std. Dev.	Avg. SNR [dB]	Std. Dev. SNR [dB]
2	Displacement[mm]	9.836	0.318	44.29	0.51
	Pressure [cmH_2O]	0.876	0.044	36.01	0.06
	Flow [l/sec]	0.621	0.057	36.01	0.44
5	Displacement[mm]	9.320	0.409	40.94	0.01
	Pressure [cmH_2O]	0.323	0.062	35.01	0.24
	Flow [l/sec]	1.031	0.056	30.27	0.25
15	Displacement[mm]	8.788	0.557	38.19	0.62
	Pressure [cmH_2O]	1.128	0.067	33.20	1.42
	Flow [l/sec]	0.146	0.056	20.47	0.54

Table 22. Single-actuator prototype with low frequency mesh-disk. Impedance values against 2, 5, and 15 $cmH_2O/l/sec$ resistances with breathing noise.

Resistance [$cmH_2O/l/sec$]	Parameter [$cmH_2O/l/sec$]	Average	Std. Dev.
2	*R*	1.79	0.01
	X	0.09	0.01
5	*R*	3.13	0.01
	X	0.13	0.03
15	*R*	7.33	0.03
	X	0.42	0.11

From these results it can be seen that, as expected, the measurements of displacement, pressure and flow, have lower SNRs compared well to the results without using the respirator pump (see Table 17 and Table 19).

The impedance calculation results were consistent with low standard deviations on values R, although not as much with X, which may be due to the very low reactance of the TLs, but as we will see the variation was lower with higher frequency oscillating mesh. By applying the calibration curve it can be seen how these values of R compare with the ones obtained without breathing noise. Table 23 shows these values.

Table 23. Single-actuator prototype with low frequency mesh-disk. Values of R after correcting function.

TL Resistance [cmH_2O/l/sec]	Corrected value [cmH_2O/l/sec]	Error %
2	1.8	10
5	4.6	8
15	13.6	9

3.2.2.2. High frequency mesh-disk

To evaluate the performance of this configuration with the lighter mesh-disk of the prototype, the same tests as with the previous configuration were made using the same methods.

Figure 66 shows the frequency response of this system.

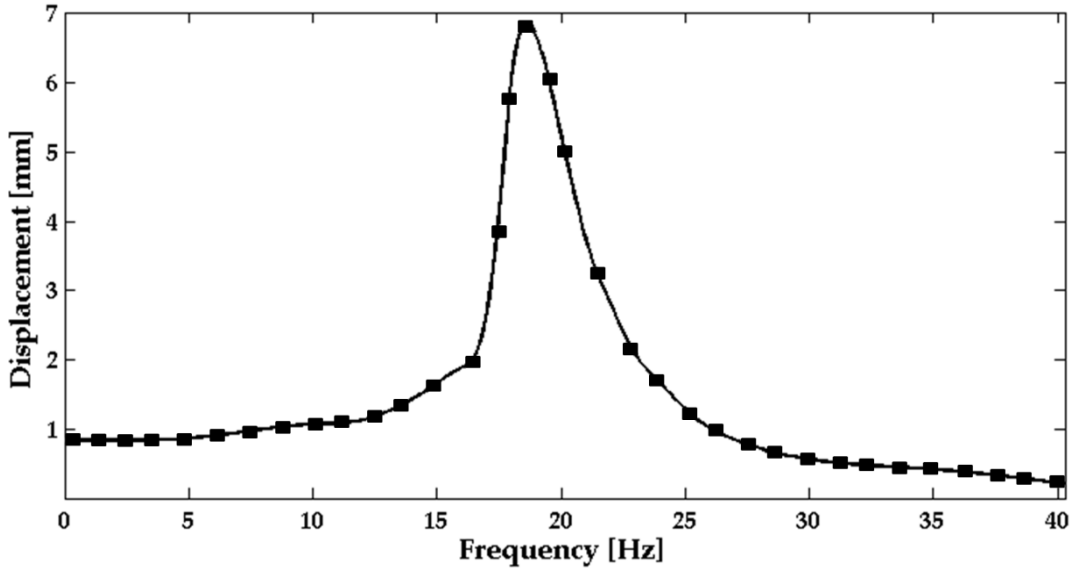

Figure 66. Frequency response, single-actuator prototype with high frequency mesh-disk.

It was found that the resonance frequency of the system was 18.8Hz. Compared to the calculations in Section 2.5.2.1 for this mesh-disk, the resonance frequency was predicted accurately, diverging from the method using experimental data by 1% and 12% from the method using the moment of inertia and other approximations.

The set of tests for this configuration was performed stimulating the actuator at resonance frequency (rounded to 19Hz for practicality).

As with the previous configuration the prototype was tested against no TL resistance, against 1, 2, 5 and 15cmH_2O/l/sec TL resistances, and also against the same TLs with simulated respiration noise. The acquired data was filtered by a 10^{th} order Butterworth band pass filter with cut-off frequencies of 15Hz and 23Hz.

The maximum average amplitude for displacement, pressure and flow measured are shown in Table 24. The average impedance values *R* and *X* and the standard deviation among the 3 tests for every TL are presented in Table 25.

Table 24. Single-actuator prototype with high frequency mesh-disk performance.

Resistance [cmH_2O/l/sec]	Parameter	Ave. Max. Amp.	Std. Dev.	Ave. SNR [dB]	Std. Dev. SNR [dB]
0	Displacement[mm]	6.715	0.094	43.06	0.11
	Pressure[cmH_2O]	0.263	0.003	50.74	0.04
	Flow[l/sec]	2.643	0.025	54.25	0.05
1	Displacement[mm]	5.327	0.093	40.52	0.50
	Pressure [cmH_2O]	0.867	0.005	43.41	0.05
	Flow [l/sec]	0.769	0.013	41.26	0.39
2	Displacement[mm]	5.201	0.115	39.13	0.39
	Pressure [cmH_2O]	0.962	0.004	42.96	0.08
	Flow [l/sec]	0.632	0.016	42.79	0.74
5	Displacement[mm]	5.005	0.127	40.27	1.10
	Pressure [cmH_2O]	1.096	0.007	42.96	0.02
	Flow [l/sec]	0.316	0.013	38.66	0.91
15	Displacement[mm]	4.835	0.151	38.24	0.40
	Pressure [cmH_2O]	1.184	0.006	43.40	0.25
	Flow [l/sec]	0.116	0.017	31.02	0.18

Table 25. Single-actuator prototype with high frequency mesh-disk. Impedance values against 1, 2, 5, and 15 $cmH_2O/l/sec$ resistances.

Resistance [$cmH_2O/l/sec$]	Parameter [$cmH_2O/l/sec$]	Average	Std. Dev.
1	*R*	0.91	0.11
	X	0.67	0.04
2	*R*	1.35	0.08
	X	0.67	0.01
5	*R*	3.35	0.16
	X	0.74	0.01
15	*R*	10.30	0.12
	X	0.21	0.06

As with the low frequency mesh-disk, it can be seen that the measurements of displacement, pressure and flow, have high 30 dB SNRs.

It also can be seen that the prototype was consistent on both values R and X. Matching the measured values to the respective reference, the correcting calibration function is obtained, as shown in Figure 67.

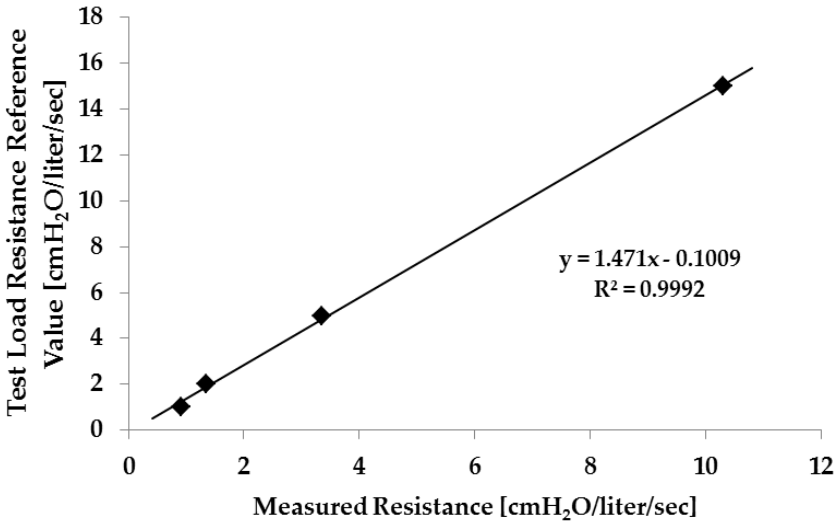

Figure 67. Resistance correction function (calibration curve), high frequency configuration.

The results for the tests with simulated breathing noise are presented below in Table 26. The average impedance values *R* and *X* and the standard deviation among the 3 tests are presented in Table 27.

Table 26. Single-actuator prototype with high frequency mesh-disk. Performance against 2, 5, and 15 $cmH_2O/l/sec$ resistances with breathing noise.

Resistance [$cmH_2O/l/sec$]	Parameter	Ave. Max. Amp.	Std. Dev.	Avg. SNR [dB]	Std. Dev. SNR [dB]
2	Displacement[mm]	4.413	0.267	32.39	0.38
	Pressure [cmH_2O]	0.994	0.025	31.12	0.07
	Flow [l/sec]	0.616	0.057	28.60	0.20
5	Displacement[mm]	4.217	0.461	31.22	0.27
	Pressure [cmH_2O]	1.115	0.0371	29.82	0.07
	Flow [l/sec]	0.309	0.047	26.53	0.40
15	Displacement[mm]	3.956	0.450	30.63	0.50
	Pressure [cmH_2O]	1.189	0.055	29.86	0.10
	Flow [l/sec]	0.134	0.050	22.67	0.94

Table 27. Single-actuator prototype with high frequency mesh-disk. Impedance values against 2, 5, and 15 $cmH_2O/l/sec$ resistances with breathing noise.

Resistance [$cmH_2O/l/sec$]	Parameter [$cmH_2O/l/sec$]	Average	Std. Dev.
2	*R*	1.48	0.01
	X	0.64	0.03
5	*R*	3.47	0.05
	X	0.58	0.09
15	*R*	9.06	0.13
	X	0.40	0.06

From these results it can be seen that, as expected, the measurements of displacement, pressure and flow with breathing noise, have lower SNRs compared to the results without using the respirator pump (see Table 24).

The impedance calculation results were consistent with low standard deviations on values R, but not as much with X. By applying the correcting calibration function it can be seen how these values of R compare with the ones obtained without breathing noise. Table 23 shows these values.

Table 28. Single-actuator prototype with low frequency mesh-disk. Values of R after correcting function.

TL Resistance [$cmH_2O/l/sec$]	Corrected value [$cmH_2O/l/sec$]	Error %
2	2.08	4
5	5.00	0
15	13.23	12

3.2.3. Comparison with the tremoFlo™

The tremoFlo, as explained briefly in section 1.5.1, is a device which uses a moving mesh to deliver the forced oscillations and through which patients breathe. The concept is the same used in this prototype and faces the same challenges in terms of mesh resistance, leak resistance and required displacement. Regarding the mechanics of the system, the main difference relies on type of actuator. The tremoFlo uses a linear voice-coil motor to move the mesh (also referred as the piston).

After consulting the mechanical engineer and lead designer of the tremoFlo Guy Drapeau, it was known that the SNR of measured pressure and flow signals is one of the most important parameters that the research and

development team at the company that developed the tremoFlo, Thorasys Inc., relies on the SNR achieved as a reference for performance.

The SNR comparison between the prototype presented in this theses and the tremoFlo is valid because the sources of noise for both systems are very similar even though the systems don't use the same mechanical parts or electronics. When performing measurements without a person (or a pump) breathing though the device, the main factor that lowers the SNR is the non-linear resistance to airflow around the moving mesh of the systems. The SNR indicates if the generated signals are of sufficient magnitude relative to the noise level.

For the tremoFlo, one of the requirements is that SNR across all frequencies should be above 30dB.

Data from a tremoFlo regarding this parameter was shared by the company to use as a reference for the prototypes developed in this thesis. Table 29 shows the SNR values obtained at four different frequencies when measuring two TLs and no load without inducing breathing noise. Table 30 shows the SNR values obtained with the prototype at similar frequencies and TLs.

Table 29. TremoFlo SNR values in dB. No noise induced.

		Frequencies			
Resistance	Parameter	5	13	17	19
14.8	Pressure SNR [dB]	62.62	57.12	52.49	53.55
	Flow SNR [dB]	52..31	43.79	40.63	42.85
0	Pressure SNR [dB]	34.61	38.72	36.62	40.85
	Flow SNR [dB]	60.8	53.18	51.09	48.58
0.5	Pressure SNR [dB]	55.31	48.36	42.75	44.00
	Flow SNR [dB]	53.95	48.21	42.44	43.45

Table 30. Single-actuator prototype SNR values in dB. No noise induced.

		Frequencies	
Resistance	Parameter	6	15
15	Pressure SNR [dB]	51.83	43.40
	Flow SNR [dB]	31.90	31.02
0	Pressure SNR [dB]	35.05	50.74
	Flow SNR [dB]	49.33	54.25
1	Pressure SNR [dB]	49.28	43.41
	Flow SNR [dB]	46.66	41.26

Even though the values obtained with the prototype were not as high as the tremoFlo, with notably lower flow SNR, the prototype did pass the required 30dB requirement.

3.3. Multiple-Actuator Version

3.3.1. Preparation

The same set-up for measuring the resistance to flow was used as described in the preparation section of the single-frequency prototype.

As with the previous prototype, the mesh-disk was adjusted in order to minimize the leak around it and get the desired resistance to flow from the mesh.

Around the edge of the disk, 4 layers of Kapton® tape were applied while checking for friction. Four was the maximum number of layers that could be used before the mesh-disk started rubbing against the chamber walls during motion. Since this prototype used the same pneumotach module with a resistance of 0.4 $cmH_2O/l/sec$ ±3%, the mesh-disk resistance was tuned in order to make the total resistance of the prototype close to 0.6 $cmH_2O/l/sec$. However this could not be achieved on this prototype due to low gap resistance as follows.

The number of layers of wire cloth used on this mesh-disk was 3. This was the maximum possible number with the press-fit part made to go in the middle of the disk. The resistance measured of the mesh-disk was 2.11cm $cmH_2O/l/sec$ ±3%. After placing the mesh-disk inside the prototype, the resistance measured across the prototype was 0.37 $cmH_2O/l/sec$ ±3%. This means that (using Equation 21) the leak around the mesh-disk was 0.45 $cmH_2O/l/sec$ ±9%, which is almost half of what would be desired.

Nevertheless the prototype was tested with this lower resistance. The testing set-up for this prototype was the same as shown in Figure 53. The piezoelectric actuators were driven at 50 Volts p-p as well and the rest of settings for the measurements were the same as with the single-actuator prototype.

Figure 54 shows a picture of the actual prototype. On the left, the prototype with the chamber opened, and on the right, being tested.

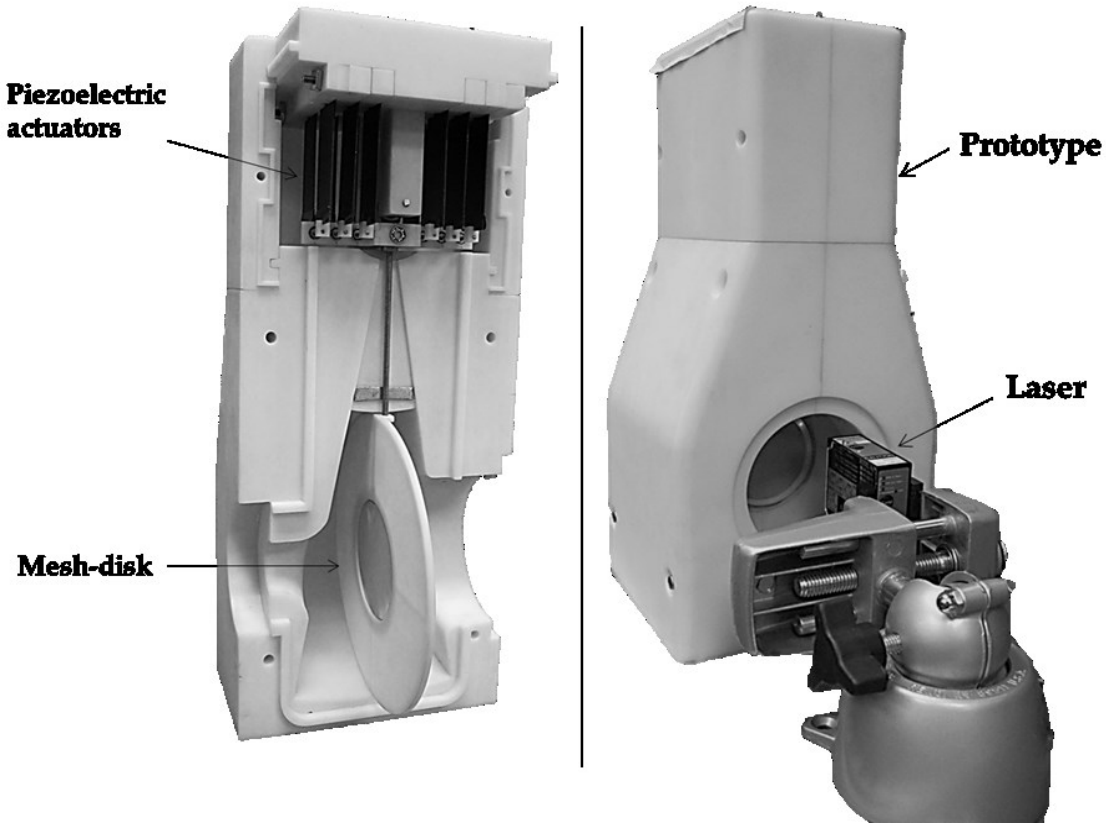

Figure 68. Multiple-actuator prototype. Open chamber (left), being tested (right).

3.3.2. Performance tests

To evaluate the performance of the multi-actuator prototype, tests were done to determine its frequency response. Before these tests, in order to verify that the displacements at the center of the mesh-disk were scalable to the displacement at the tip of the actuators and there wasn't considerable bending of the rod, a quick test was performed measuring the displacement at two different points of the rod while the system was stimulated at resonance frequency. Table 31 shows the results of this test, where the "location of measurement" corresponds to the distance from the pivot point of the lever (on end of the rod) to the point on the rod at which the displacement (on the axis perpendicular to the rod at rest) was measured.

Table 31. Resonance frequency of multi-actuator prototype.

Location of measurement [mm]	Disp. Amplitude [mm]	Standard deviation [mm]	Scale factor
130	27.270	0.241	4.76
25	5.230	0.046	4.78

As expected, due to the highly stiff stainless steel rod, the results showed that the scale factor on both measurements was (practically) the same as the location of the measurements on the rod.

The frequency response tests were then performed by measuring the displacement at the center of the mesh-disk (170 mm from the pivot point of the lever) and stimulating the system with frequencies from 0.5Hz to 20Hz in steps of 0.5 Hz for 10 seconds each against no TL resistance and no induced respiration noise. Figure 69 shows the obtained frequency response. The line in

between the data points was made by a smoothing spline with a parameter p=0.99 for better visualization.

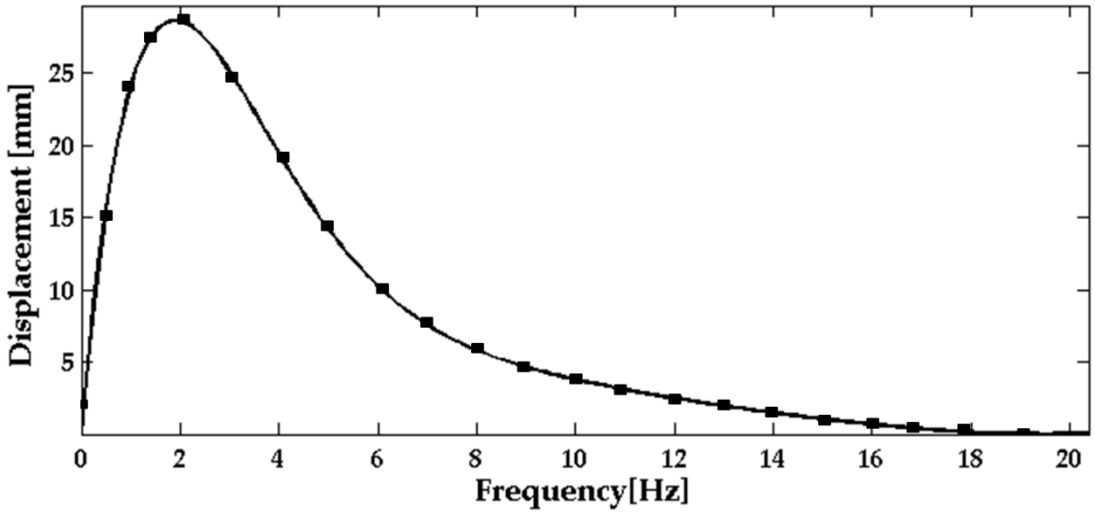

Figure 69. Frequency response, Multi-actuator prototype with all actuators stimulated.

It was found that the resonance frequency of the system was 1.9 Hz. This result differed by only 0.4 Hz (a discrepancy of 21%) form the estimated in design. This discrepancy is likely due mainly to the assumptions made to simplify the model and the calculations, but also perhaps due to small errors in measurement of the actual moment arm distances.

Tests were made on the system with different masses (moulding clay spheres) placed at the end of the rod (instead of the mesh-disk), similarly to the ones made in section 2.5.2.1 for the single-actuator device, in order to see the resonance frequencies obtained. Figure 70 shows the results of the tests.

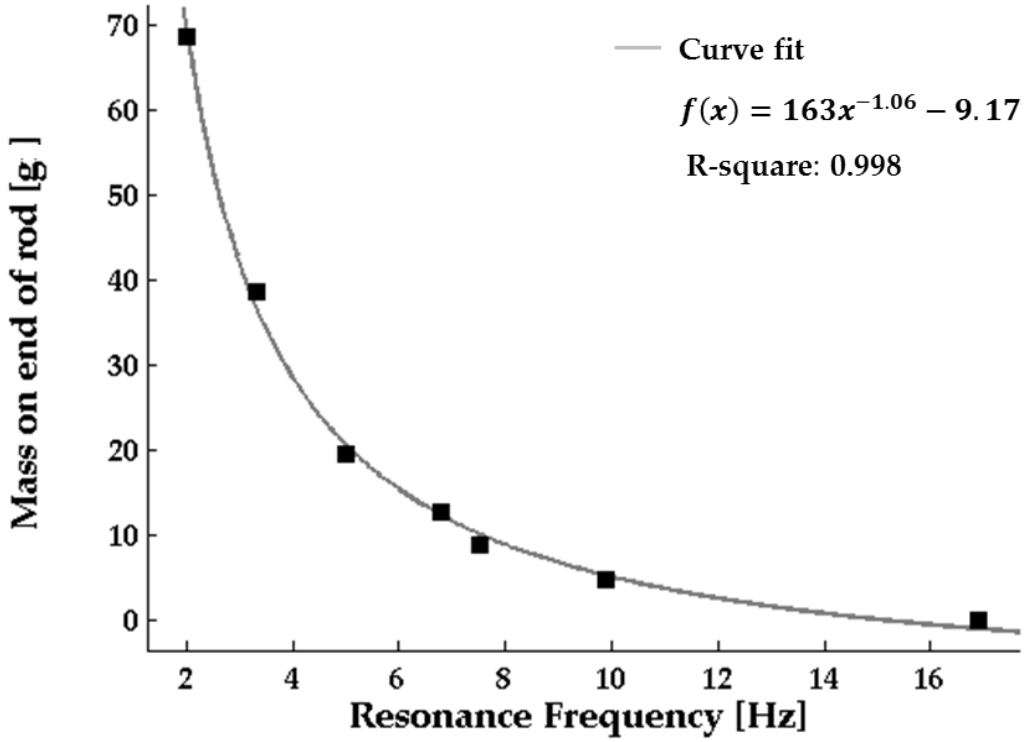

Figure 70. Multi-actuator prototype, mass at tip vs. resonance frequency results.

The empirical curve fit varies nearly inversely with resonant frequency. While Equation 32 indicates that the resonant frequency should vary inversely to the square root of the angular momentum of the rod-mesh disk system. Since the angular momentum of any rod or fixed point mass is proportional to the mass, this implies a theoretical prediction for fixed amplitude of oscillation that should be according to the inverse square root of mass at the tip. Since the relation is better approximated by an inverse power law with unity exponent, this means that the displacement of the dynamical system must vary inversely with mass as well (x approximately proportional to 1/m and thus $1/I_P$). These results of Figure 70 show an approximated behavior of the system since it wasn't tested with actual disks of the required size from the design, and in

consequence, the moments of inertia are lower due to size and density of the masses used for these tests. However, it is useful to see that with the designed length of the rod, required size (and thus mass) of the mesh-disk, and the torque applied by the actuators, it would be very difficult to achieve a resonance frequency higher than 10 Hz, since the mass of the disk would have to be extremely low. Recommendations for future designs are made in section 4.1.

It was of interest to determine the performance of the system with altered number of actuators, as this was made adjustable in the design, as a means to determine the fewest number of actuators needed to achieve acceptable performance. The prototype was thus also tested for its frequency response using the minimum number of actuators it can work with, 4 actuators (as shown in Figure 46). Figure 71 shows the results of this test.

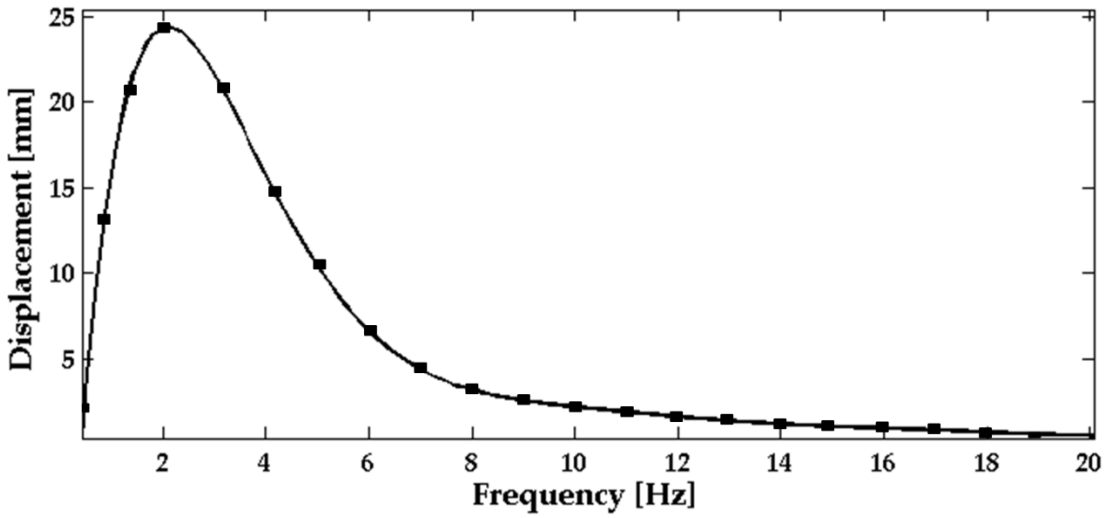

Figure 71. Frequency response, multi-actuator prototype, 2 actuators stimulated and 10 passive.

On these results, the system showed a reduction of 11% in amplitude compared to the use of all 12 actuators and thus it could be concluded that this could still deliver the required displacement at low frequencies, although this was not tested with breathing loading. The reasonable performance with fewer actuators was interesting as it indicated fairly robust behavior, but again, this test was unloaded and thus might exhibit some compliance with breathing or with high patient load. In any case, the goal of this prototype was to be able to apply oscillations at different frequencies among the standard range of frequencies for FOT, and the best performance should be with all actuators active. Therefore, the prototype was tested using 12 actuators under unloaded and loaded conditions and with respiratory noise as follows.

Despite the low resonance frequency, it was reasoned that the prototype design would serve as a reasonable test bed for an above resonance FOT device. Indeed the amplitude of oscillations are generally reduced with frequency of oscillation in FOT in an approximately 1/f dependence, thus by adjusting the resonant frequency to be at or below the lowest desired frequency, it may be possible to achieve acceptable performance. Thus the performance in terms of displacement, pressure, and flow of the prototype was tested with a composite signal of 5 and 15 Hz added to each other of equal amplitude and shifted 180 degrees. The composite signal was created with amplitudes for both frequencies adjusted to partly compensate for the shape of the frequency response of the system. That is the oscillating input was designed with a small amplitude for 5 Hz, and a larger amplitude at 15 Hz to increase the signal amplitude at the higher frequency with the goal of achieving similar flow amplitudes as is common for FOT devices. Thus this test used the prototype for oscillations only above the actual resonance frequency, which was one of the

original designs considered. The prototype was tested against no resistance load first and then against TLs of 1, and 5 $cmH_2O/l/sec$ resistance without simulated respiratory noise. As with the single-actuator prototype, the tests were performed 3 times, 20 seconds each. The acquired data was filtered by a 10^{th} order Butterworth band pass filter with cut-off frequencies of 3 Hz and 19Hz. Separately, the data was filtered by the same type of filter with cut-off frequencies of 3 Hz and 7 Hz to analyze the 5 Hz portion of the signal and 13 Hz and 17 Hz for the 15 Hz part before doing the amplitude calculations and impedance measurements.

Figure 72, Figure 73, Figure 74, show examples in the time domain and frequency domain of the displacement, pressure, and flow respectably of the data recorded in one of the tests against no TL.

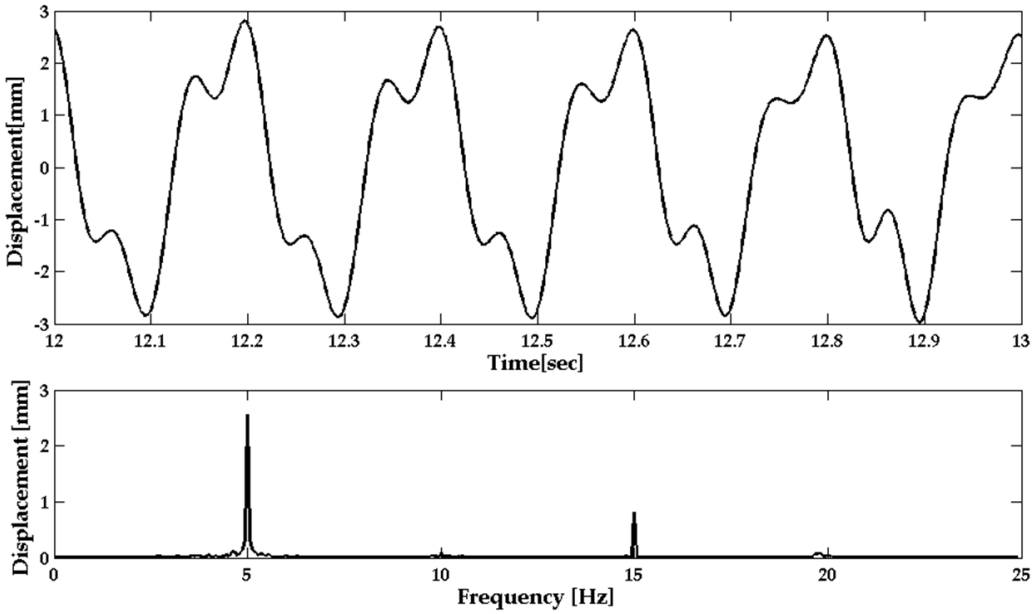

Figure 72. Multi-actuator prototype, 5-15 Hz signal displacement example.

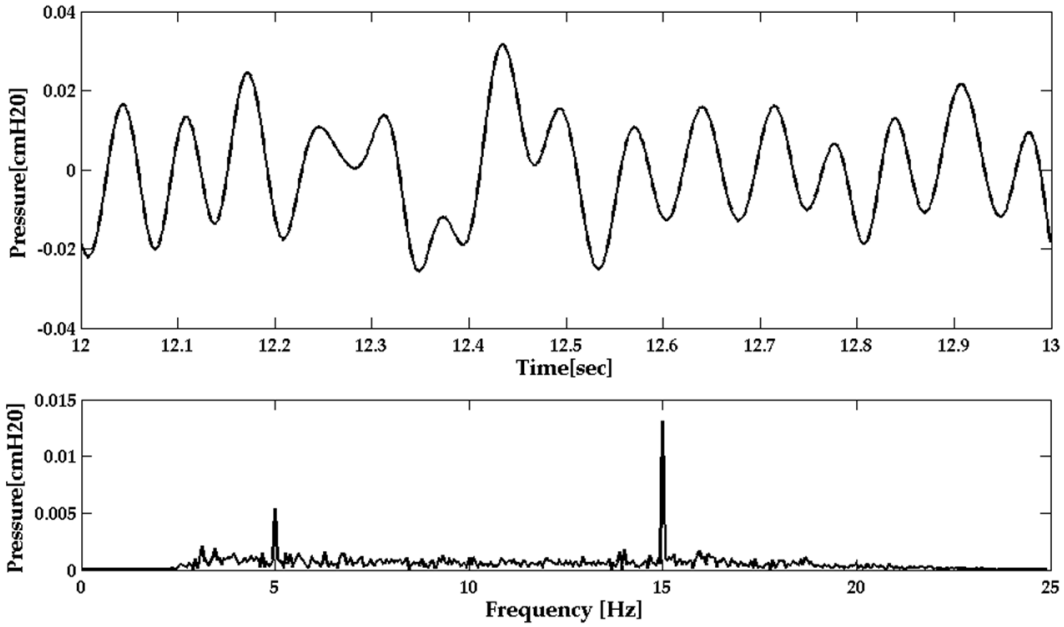

Figure 73. Multi-actuator prototype, 5-15 Hz signal pressure example.

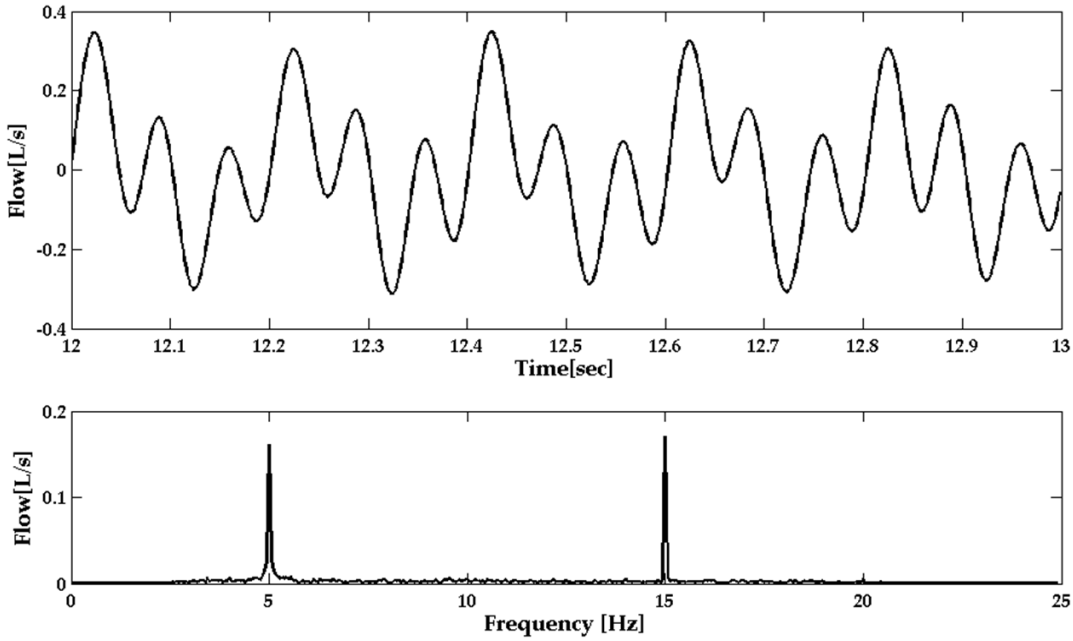

Figure 74. Multi-actuator prototype, 5-15 Hz signal flow example showing similar flow amplitudes at the different frequencies.

The maximum average amplitude for displacement, pressure and flow measured at the 2 frequencies are shown in Table 32. The average impedance values *R* and *X* and the standard deviation among the 3 tests for every TL are presented in Table 33.

Table 32. Multiple-actuator prototype performance.

Resistance [cmH_2O/l/sec]	Frq. [Hz]	Parameter	Ave. Max. Amp.	Std. Dev.	Ave. SNR [dB]	Std. Dev. SNR [dB]
0	5	Displacement[mm]	2.570	0.241	31.06	0.48
		Pressure[cmH_2O]	0.007	0.005	14.67	0.10
		Flow[l/sec]	0.162	0.043	28.87	0.23
	15	Displacement[mm]	0.773	0.064	37.65	0.51
		Pressure [cmH_2O]	0.013	0.003	25.54	0.06
		Flow [l/sec]	0.161	0.014	35.29	0.44
1	5	Displacement[mm]	1.302	0.126	33.64	0.40
		Pressure[cmH_2O]	0.021	0.007	23.59	0.25
		Flow[l/sec]	0.027	0.023	12.44	0.18
	15	Displacement[mm]	0.754	0.061	37.30	0.39
		Pressure [cmH_2O]	0.042	0.004	33.88	0.08
		Flow [l/sec]	0.040	0.016	24.48	0.74
5	5	Displacement[mm]	1.346	0.076	34.68	0.51
		Pressure[cmH_2O]	0.024	0.006	27.36	0.32
		Flow[l/sec]	0.021	0.014	8.56	0.24
	15	Displacement[mm]	0.735	0.055	37.31	0.62
		Pressure [cmH_2O]	0.049	0.005	33.10	1.21
		Flow [l/sec]	0.026	0.013	14.59	0.73

Table 33. Multi-actuator prototype. Impedance values against 1 and 5 $cmH_2O/l/sec$ TLs.

Resistance [$cmH_2O/l/sec$]	Frq. [Hz]	Parameter [$cmH_2O/l/sec$]	Average	Std. Dev.
1	5	*R*	1.34	0.13
		X	0.37	0. 07
	15	*R*	1.01	0.08
		X	0.54	0.02
5	5	R	1.71	0.33
		X	0.56	0.12
	15	R	2.39	0.11
		X	0.72	0.12

These results show the performance of the prototype is currently unacceptable, especially for the flow measurements where the SNR was as low as 14.6 dB. This can be attributed to lack of sufficient air flow resistance around the mesh-disk (leak) as mentioned in the preparation section 3.3.1. The flow measurement performance against any higher resistances would show even lower performance, even without any breathing noise.

However, the performance regarding displacement was sufficient, with SNRs higher that 30dB in all cases and achieving the required amplitude as calculated and illustrated in Figure 30. It is recommended that this design still could be considered, but the mesh-disk resistance must be increased to 0.6 cmH20/l/s, which can be achieved by narrower gap between the mesh-disk and chamber, which should be achievable with more accurate dimensioning than was achieved with machining used here. The amplitudes should be sufficient to provide adequate flow SNR if this is met, but if higher SNR is required it should be possible to increase the oscillatory amplitude even further by considering slightly higher displacement amplification. The available force

should still be sufficient however with 12 actuators, or possibly even fewer actuators.

CHAPTER 4: CONCLUSIONS

To reach the objective of this thesis I have modeled the design of two types of piezo-actuated airway oscillometers. I have built and completed extensive testing of both prototypes.

I was able to test the single-actuator device in all necessary aspects to provide a very good proof of concept for the development of Airwave Oscillometry in a compact, inexpensive, light-weight and portable device that can achieve reliable performance using piezoelectric bimorph actuators. The device should represent a less expensive to manufacture and is a much simpler mechanical actuation design than any other approach. The single frequency device could be developed for adults at 5 Hz for example, and perhaps a higher frequency device for infants or children since they breathe at higher breathing frequencies as it is known that often frequencies as high as 8 or 10 Hz are needed in these subjects. This single frequency device could be readily used for within-breath impedance tracking of the time-varying respiratory system.

If multiple frequencies are of interest in a single subject, the single-actuator device is capable of delivering impedance measurements at different frequencies independently, but only via changing the mass of the disk. Even though testing multiple frequencies with this device would thus take longer than applying a composite signal, it is still a desirable feature particularly for respiratory researchers. Perhaps automated methods to change the resonance frequency could be considered such as an adjustable mass location on the actuator, but this does increase the complexity.

The single frequency approach takes advantage of the natural resonance of the actuator and thus requires very little power for operation; it could thus be battery operated. Given its characteristics and performance, this device is particularly suited for easy assessment of airway resistance for diagnosis and disease monitoring. Of the two designs considered here, the single frequency device is very simple and represents the most likely device for further development.

The multiple-actuator prototype was capable of achieving the required displacement at low frequencies (4 to 15 Hz) using the amplification system designed. The multi-actuator prototype performance at low frequencies with a composite signal for the FOT was tested. It was found that the prototype delivered the required displacement at 5 and 15 Hz, with appropriate mass and size of moving mesh affixed to the actuator, but the low resistance presented by the gap around the mesh-disk prevented the system to achieve high SNRs of pressure and flow signals to accurately measure resistances of 5 cmH2O/l/sec or higher. To conclude, the single-actuator prototype delivered consistent impedance measurements proving the concept proposed in this thesis. The amplification method implemented on the multi-actuator version proved the possibility of a design of a prototype using composite oscillations at medium to low frequencies for FOT.

4.1. Recommendations and possible improvements

The following are possible improvements and recommendations over the design and use of the two main prototypes present in this thesis.

1. While I used off-the shelf actuators, the design of the piezo-actuated oscillometry device does not have to be constrained to these. To achieve optimal performance, it would be ideal to custom design (longer or narrower) actuators to achieve larger displacements, and in volume this could be very inexpensive. Also, I did not explore altering the electrical drive circuit for the piezoelectric actuators. The electrical characteristics of the actuator can be modified to adjust its electrical impedance which can be utilized to change its resonance frequency. As an example, consider a simple single layer piezoelectric transducer with an equivalent network representation as shown in Figure 75.

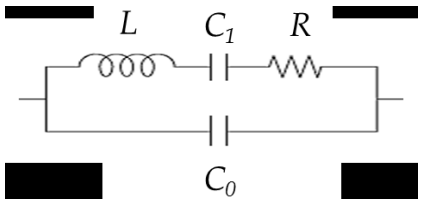

Figure 75. Equivalent circuit of transducer.

where *L is* inductance, *R* resistance, C_1 series capacitance, and C_0 is parallel capacitance. The resonance frequency would be determined by Equation 34 and the anti-resonance frequency by Equation 35 [76].

$$\omega_n = \frac{1}{2\pi}\sqrt{LC}$$

Equation 34

$$\omega_a = \frac{1}{2\pi}\sqrt{\frac{LC_0C_1}{(C_0 + C_1)}}$$

Equation 35

As can be seen in Equation 34, the resonance frequency can be changed by adjusting the inductance or the capacitance. The use of external capacitance can also be used to modify the resonance. Lowering the

resonance electrically and/or changing the actuator's dimensions (accounting for the actuators displacement and generated force trade-offs) could allow greater freedom for design of the actuator system and could possibly permit the use of less heavy mesh-disks for lower frequencies in the single-actuator design, however more detailed analysis would be required to examine if altering the resonance electroincially would have significant advantages.

Another benefit of custom made actuators is that, if enough quantities are produced, they can be more economic than standard off-the-shell ones.

2. The design of the prototypes chambers (parts surrounding the mesh-disk), as well as the mesh-disk can be made more precisely and with tighter tolerances if better 3D printing, better machining or molding technology is employed for production. This would decrease the leak (increase the leak resistance to flow), permitting greater control of the resistance via choice of mesh and mesh area. This would improve performance of both designs.
3. Regarding only the multi-actuator design, the overall size of the device is far too large for a commercially successful device and the expense of the housing would be prohibitive. The device would have to be scaled down. In order to do so, the following changes could be made:
    - The total length of rod (lever) holding the mesh-disk can be reduced by decreasing the length of input-to-pivot and keeping the same amplification ratio.

- The amplification ratio can also be increased for larger displacements requiring a smaller mesh-disk for same volume displaced.
- After increasing the amplification ratio in order to displace more volume, reducing the size and weight of both the rod and the mesh-disk, while keeping the stiffness of the rod high, or increasing it, would translate into a lever mechanism with a smaller moment of inertia which would lead to achieving a higher resonance frequency. A smaller mesh-disk would also make it easier to achieve a smaller leak around it.
- To contribute to the shift of the resonance frequency, the stiffness (and force) of system can be increased by the use of thicker actuators or a larger quantity of them.

4. In order to take the design of the prototypes towards a commercial level, the design and integration of circuit boards with the necessary components will be needed. The boards need to include miniature differential pressure transducers such as the 2" H_2O range reference DLVR-L02D-E2NS-C-NI3F [77]. The circuitry should include operational amplifiers to condition and process the signals, power management components, analog to digital converters and a microprocessor to generate the waveforms, acquire the data, and transfer it to a computer. It could also be possibly to analyse the data internally and display it on an integrated screen.
5. Finally, it should be noted that the performance of the prototypes was not tested while holding them on the hands. Holding the prototypes,

especially the single-actuator one, with the hands while using them may have some effect on the performance of the device since it is possible that this adds an additional degree of freedom, although it is highly damped. However the tremoFlo™ has much more moving mass yet there is very little detectable vibration while it is used. Owing to the very light weight of the piezo-actuator and mesh-disk it is unlikely that this will be a major effect, but it needs to be determined. If vibration is an issue, then additional static mass might be the simplest approach to improve behavior, although reducing the mass of the mesh with longer actuators, and/or electrically adjusting the resonant frequency via adjusting the piezoelectric electrical element behavior is another approach.

4.2. Statement of contributions

The following is a list of the contributions present in this thesis:

1. I developed a novel application using piezoelectric multilayered bending actuators for FOT devices.
2. I developed a simple and likely cost-effective prototype capable of functioning as an FOT device. The design has viable potential to become a commercial device at a low cost consequently increasing adoption of FOT.
3. I developed a prototype capable of amplifying the displacement at the tip of bender actuators and deliver large displacements for the application of FOT with a moving mesh. Upon correction of the resonance frequency and improvement of the design (as described in

numeral 3 of the previous section) the system is predicted to be capable of performing FOT using combined frequencies.

4. I applied the dynamic kinetic theory for the motion of the single beam piezoelectric bimorph actuator which was accurate to enable accurate design.
5. I developed the dynamic kinetic theory for the rotational motion of the lever amplified motion used in the multi-actuator multi-frequency prototype, which was sufficiently accurate for its design.
6. I contributed a full design description of the two prototypes in this thesis for their reproduction.
7. I contributed designs of test beds for testing of air flow resistance, displacement performance of piezoelectric bender actuators, and performance of moving-mesh type of FOT devices.

REFERENCES

[1] M. Ochs, J. R. Nyengaard, A. Jung, L. Knudsen, M. Voigt, T. Wahlers, J. Richter, and H. J. G. Gundersen, "The number of alveoli in the human lung.," *Am. J. Respir. Crit. Care Med.*, vol. 169, no. 1, pp. 120–4, Jan. 2004.

[2] A. C. Guyton and J. E. Hall, *Textbook of Medical Physiology, 11e (Guyton Physiology)*. Saunders, 2005.

[3] R. Pellegrino, G. Viegi, V. Brusasco, R. O. Crapo, F. Burgos, R. Casaburi, A. Coates, C. P. M. van der Grinten, P. Gustafsson, J. Hankinson, R. Jensen, D. C. Johnson, N. MacIntyre, R. McKay, M. R. Miller, D. Navajas, O. F. Pedersen, and J. Wanger, "Interpretative strategies for lung function tests.," *Eur. Respir. J.*, vol. 26, no. 5, pp. 948–68, Nov. 2005.

[4] J. H. T. Bates, *Lung Mechanics: An Inverse Modeling Approach*. Cambridge University Press, 2009.

[5] A. B. Otis, C. B. McKerrow, R. A. Bartlett, J. Mead, M. B. McIlroy, N. J. Selverstone, and E. P. . J. Radford, "Mechanical Factors in Distribution of Pulmonary Ventilation," *J Appl Physiol*, vol. 8, no. 4, pp. 427–443, Jan. 1956.

[6] C. W. Thorpe and J. H. T. Bates, "Effect of stochastic heterogeneity on lung impedance during acute bronchoconstriction: a model analysis," *J Appl Physiol*, vol. 82, no. 5, pp. 1616–1625, May 1997.

[7] D. W. Kaczka, D. N. Hager, M. L. Hawley, and B. A. Simon, "Quantifying mechanical heterogeneity in canine acute lung injury: impact of mean airway pressure.," *Anesthesiology*, vol. 103, no. 2, pp. 306–17, Aug. 2005.

[8] Q. Hamid, J. S. MD, and J. Martin, *Physiological Basis of Respiratory Disease*. pmph usa, 2005.

[9] WHO, "Asthma, Fact sheet N°307," 2011. [Online]. Available: http://www.who.int/mediacentre/factsheets/fs307/en/.

[10] "Statistics Canada, Asthma, by age group and sex (Percent)," 17-Jun-2013. [Online]. Available: http://www.statcan.gc.ca/tables-tableaux/sum-som/l01/cst01/health49b-eng.htm.

[11] R. Garner and D. Kohen, "Changes in the prevalence of asthma among Canadian children.," *Health Rep.*, vol. 19, no. 2, pp. 45–50, Jun. 2008.

[12] "Lung Facts," Ottawa, 1994.

[13] "Global Strategy for Asthma Management and Prevention, Global Initiative for Asthma (GINA) 2012," 2012. [Online]. Available: http://www.ginasthma.org/.

[14] WHO, "Chronic obstructive pulmonary disease (COPD) Fact sheet N°315," 2013. [Online]. Available: http://www.who.int/mediacentre/factsheets/fs315/en/index.html.

[15] WHO, Ed., *The global burden of disease 2004*. Switzerland: WHO Library Cataloguing-in-Publication Data, 2004.

[16] "Global Strategy for the Diagnosis, Management, and Prevention of Chronic Obstructive Pulmonary Disease," Global Initiative for Chronic Obstructive Lung Disease, 2013.

[17] RESMED, "ResMed - Enhanced AutoSet." [Online]. Available: http://www.resmed.com/us/products/s9_series/enhanced-autoset.html?nc=clinicians.

[18] "Guidelines for Methacholine and Exercise Challenge Testing—1999," *Am. J. Respir. Crit. Care Med.*, vol. 161, no. 1, pp. 309–329, Jan. 2000.

[19] L. J. Ignarro, G. M. Buga, K. S. Wood, R. E. Byrns, and G. Chaudhuri, "Endothelium-derived relaxing factor produced and released from artery and vein is nitric oxide.," *Proc. Natl. Acad. Sci.*, vol. 84, no. 24, pp. 9265–9269, Dec. 1987.

[20] R. M. Palmer, D. S. Ashton, and S. Moncada, "Vascular endothelial cells synthesize nitric oxide from L-arginine.," *Nature*, vol. 333, no. 6174, pp. 664–6, Jun. 1988.

[21] A. F. Samdani, T. M. Dawson, and V. L. Dawson, "Nitric Oxide Synthase in Models of Focal Ischemia," *Stroke*, vol. 28, no. 6, pp. 1283–1288, Jun. 1997.

[22] R. A. Dweik, S. A. Comhair, B. Gaston, F. B. Thunnissen, C. Farver, M. J. Thomassen, M. Kavuru, J. Hammel, H. M. Abu-Soud, and S. C. Erzurum, "NO chemical events in the human airway during the immediate and late antigen-induced asthmatic response.," *Proc. Natl. Acad. Sci. U. S. A.*, vol. 98, no. 5, pp. 2622–7, Feb. 2001.

[23] F. H. Guo, S. A. Comhair, S. Zheng, R. A. Dweik, N. T. Eissa, M. J. Thomassen, W. Calhoun, and S. C. Erzurum, "Molecular mechanisms of increased nitric oxide (NO) in asthma: evidence for transcriptional and post-translational regulation of NO synthesis.," *J. Immunol.*, vol. 164, no. 11, pp. 5970–80, Jun. 2000.

[24] A. D. Smith, J. O. Cowan, S. Filsell, C. McLachlan, G. Monti-Sheehan, P. Jackson, and D. R. Taylor, "Diagnosing asthma: comparisons between exhaled nitric oxide measurements and conventional tests.," *Am. J. Respir. Crit. Care Med.*, vol. 169, no. 4, pp. 473–8, Feb. 2004.

[25] L. E. Gustafsson, A. M. Leone, M. G. Persson, N. P. Wiklund, and S. Moncada, "Endogenous nitric oxide is present in the exhaled air of rabbits, guinea pigs and humans," *Biochem. Biophys. Res. Commun.*, vol. 181, no. 2, pp. 852–857, 1991.

[26] "Recommendations for standardized procedures for the on-line and off-line measurement of exhaled lower respiratory nitric oxide and nasal nitric oxide in adults and children-1999. This official statement of the American Thoracic Society was adopted by the ," *Am. J. Respir. Crit. Care Med.*, vol. 160, no. 6, pp. 2104–17, Dec. 1999.

[27] K. Von Neergaard and K. Wirz, "Die Messung der Strömungswiderstände in den Atemwegen des Menschen, insbesondere bei Asthma und Emphysem," *Z Klin Med*, 1927.

[28] M. Rosenfeld, J. Allen, B. H. G. M. Arets, P. Aurora, N. Beydon, C. Calogero, R. G. Castile, S. D. Davis, S. Fuchs, M. Gappa, P. M. Gustaffson, G. L. Hall, M. H. Jones, J. C. Kirkby, R. Kraemer, E. Lombardi, S. Lum, O. H. Mayer, P. Merkus, K. G. Nielsen, C. Oliver, E. Oostveen, S.

Ranganathan, C. L. Ren, P. D. Robinson, P. C. Seddon, P. D. Sly, M. M. Sockrider, S. Sonnappa, J. Stocks, P. Subbarao, R. S. Tepper, and D. Vilozni, "An official American Thoracic Society workshop report: optimal lung function tests for monitoring cystic fibrosis, bronchopulmonary dysplasia, and recurrent wheezing in children less than 6 years of age.," *Ann. Am. Thorac. Soc.*, vol. 10, no. 2, pp. S1–S11, Apr. 2013.

[29] M. R. Thomas, L. Marston, G. F. Rafferty, S. Calvert, N. Marlow, J. L. Peacock, and A. Greenough, "Respiratory function of very prematurely born infants at follow up: influence of sex.," *Arch. Dis. Child. Fetal Neonatal Ed.*, vol. 91, no. 3, pp. F197–201, May 2006.

[30] V. R. Kairamkonda, J. Richardson, N. Subhedar, P. D. Bridge, and N. J. Shaw, "Lung function measurement in prematurely born preschool children with and without chronic lung disease.," *J. Perinatol.*, vol. 28, no. 3, pp. 199–204, Mar. 2008.

[31] M. Oswald-Mammosser, A. Charloux, L. Donato, C. Albrech, J. P. Speich, E. Lampert, and J. Lonsdorfer, "Interrupter technique versus plethysmography for measurement of respiratory resistance in children with asthma or cystic fibrosis.," *Pediatr. Pulmonol.*, vol. 29, no. 3, pp. 213–20, Mar. 2000.

[32] Y. Guo, T. Sun, F. Herrmann, and J.-P. Janssens, "Comparison of airway resistance measurements by the forced oscillation technique and the interrupter technique for detecting chronic obstructive pulmonary disease in elderly patients.," *Chin. Med. J. (Engl).*, vol. 118, no. 22, pp. 1921–4, Nov. 2005.

[33] A. B. DuBois, A. W. Brody, D. H. Lewis, and B. F. Burgess, "Oscillation Mechanics of Lungs and Chest in Man," *J Appl Physiol*, vol. 8, no. 6, pp. 587–594, May 1956.

[34] N. B. Pride, "Forced oscillation techniques for measuring mechanical properties of the respiratory system.," *Thorax*, vol. 47, no. 4, pp. 317–20, Apr. 1992.

[35] D. Navajas and R. Farré, "Forced oscillation technique: from theory to clinical applications.," *Monaldi Arch. Chest Dis.*, vol. 56, no. 6, pp. 555–62, Dec. 2001.

[36] R. Peslin, J. Felicio da Silva, C. Duvivier, and F. Chabot, "Respiratory mechanics studied by forced oscillations during artificial ventilation," *Eur. Respir. J.*, vol. 6, no. 6, pp. 772–784, Jun. 1993.

[37] P. J. Sterk, "Detection of expiratory flow limitation in COPD using the forced oscillation technique," *Eur. Respir. J.*, vol. 24, no. 2, pp. 332–333, Aug. 2004.

[38] D. Navajas, R. Farré, M. Rotger, R. Badia, M. Puig-de-Morales, and J. M. Montserrat, "Assessment of airflow obstruction during CPAP by means of forced oscillation in patients with sleep apnea.," *Am. J. Respir. Crit. Care Med.*, vol. 157, no. 5 Pt 1, pp. 1526–30, May 1998.

[39] R. L. Dellacà, M. Rotger, a Aliverti, D. Navajas, a Pedotti, and R. Farré, "Noninvasive detection of expiratory flow limitation in COPD patients during nasal CPAP.," *Eur. Respir. J.*, vol. 27, no. 5, pp. 983–91, May 2006.

[40] R. Peslin, R. Farre, M. Rotger, and D. Navajas, "Effect of expiratory flow limitation on respiratory mechanical impedance: a model study," *J Appl Physiol*, vol. 81, no. 6, pp. 2399–2406, Dec. 1996.

[41] N. T. Tgavalekos, G. Musch, R. S. Harris, M. F. Vidal Melo, T. Winkler, T. Schroeder, R. Callahan, K. R. Lutchen, and J. G. Venegas, "Relationship between airway narrowing, patchy ventilation and lung mechanics in asthmatics.," *Eur. Respir. J.*, vol. 29, no. 6, pp. 1174–81, Jun. 2007.

[42] C. a Lall, N. Cheng, P. Hernandez, P. T. Pianosi, Z. Dali, a Abouzied, and G. N. Maksym, "Airway resistance variability and response to bronchodilator in children with asthma.," *Eur. Respir. J. Off. J. Eur. Soc. Clin. Respir. Physiol.*, vol. 30, no. 2, pp. 260–8, Aug. 2007.

[43] E. Oostveen, D. MacLeod, H. Lorino, R. Farre, Z. Hantos, K. Desager, and F. Marchal, "The forced oscillation technique in clinical practice: methodology, recommendations and future developments," *Eur. Respir. J.*, vol. 22, no. 6, pp. 1026–1041, Dec. 2003.

[44] E. J. M. Weersink, F. J. J. v.d. Elshout, C. v. Herwaarden, and H. Folgering, "Bronchial responsiveness to histamine and methacholine measured with forced expirations and with the forced oscillation technique," *Respir. Med.*, vol. 89, no. 5, pp. 351–356, 1995.

[45] N. B. Pride, “Forced oscillation techniques for measuring mechanical properties of the respiratory system,” pp. 317–320, 1992.

[46] R. Farré, M. Rotger, J. M. Montserrat, and D. Navajas, “A system to generate simultaneous forced oscillation and continuous positive airway pressure,” *Eur. Respir. J.*, vol. 10, no. 6, pp. 1349–1353, Jun. 1997.

[47] D. Navajas, R. Farre, J. Canet, M. Rotger, and J. Sanchis, “Respiratory input impedance in anesthetized paralyzed patients,” *J Appl Physiol*, vol. 69, no. 4, pp. 1372–1379, Oct. 1990.

[48] D. Navajas and R. Farré, “Forced oscillation assessment of respiratory mechanics in ventilated patients.,” *Crit. Care*, vol. 5, no. 1, pp. 3–9, Jan. 2001.

[49] J. Rigau, R. Farre, J. Roca, S. Marco, a. Herms, and D. Navajas, “A portable forced oscillation device for respiratory home monitoring,” *Eur. Respir. J.*, vol. 19, no. 1, pp. 146–150, Jan. 2002.

[50] J. Rigau, F. Burgos, C. Hernandez, J. Roca, D. Navajas, and R. Farre, “Unsupervised self-testing of airway obstruction by forced oscillation at the patient’s home,” *Eur. Respir. J.*, vol. 22, no. 4, pp. 668–671, Oct. 2003.

[51] CareFusion, “IOS Impulse Spirometry.” [Online]. Available: http://www.carefusion.com/medical-products/respiratory/cardio-pulmonary-diagnostics/pulmonary-function-testing/pft-complete-testing/ios-impulse-spirometry.aspx.

[52] Chest, “Mostgraph-01.” [Online]. Available: http://www.chest-mi.co.jp/product/mostgraph-01/.

[53] COSMED, “Quark PFT: Pulmonary Function Testing Equipment.” [Online]. Available: http://www.cosmed.com/en/products/pulmonary-function/quark-pft-pulmonary-function-testing-lab.

[54] R. Peslin, P. Jardin, C. Duvivier, and P. Begin, “In-phase rejection requirements respiratory input impedance,” pp. 804–809, 1984.

[55] B. Culshaw, *Smart Structures and Materials (Artech House Optoelectronics Library)*. Artech House, 1996.

[56] S.-E. Park and T. R. Shrout, “Ultrahigh strain and piezoelectric behavior in relaxor based ferroelectric single crystals,” *J. Appl. Phys.*, vol. 82, no. 4, p. 1804, Aug. 1997.

[57] K. Uchino, “Piezoelectric actuators 2006,” *J. Electroceramics*, vol. 20, no. 3–4, pp. 301–311, Jul. 2007.

[58] R. G. Ballas, *Piezoelectric Multilayer Beam Bending Actuators: Static and Dynamic Behavior and Aspects of Sensor Integration (Google eBook)*. Springer, 2007.

[59] A. J. Moskalik and D. Brei, “Quasi-Static Behavior of Individual C-Block Piezoelectric Actuators,” *J. Intell. Mater. Syst. Struct.*, vol. 8, no. 7, pp. 571–587, Jul. 1997.

[60] W. Xu and T. G. King, “Mechanical amplifier design for piezo-actuator applications,” *IEE Manuf. Div. Colloq. Innov. Actuators Mechatron. Syst.*, 1996.

[61] T. Lee and I. Chopra, “Design of piezostack-driven trailing-edge,” vol. 15.

[62] J. Garcia-Bonito, M. J. Brennan, S. J. Elliott, A. David, and R. J. Pinnington, “A novel high-displacement piezoelectric actuator for active vibration control,” *Smart Mater. Struct.*, vol. 7, no. 1, pp. 31–42, Feb. 1998.

[63] K. Onitsuka, A. Dogan, J. F. Tressler, Q. Xu, S. Yoshikawa, and R. E. Newnham, “Metal-Ceramic Composite Transducer, the ‘Moonie,’” *J. Intell. Mater. Syst. Struct.*, vol. 6, no. 4, pp. 447–455, Jul. 1995.

[64] C. Niezrecki, D. Brei, S. Balakrishnan, and a. Moskalik, “Piezoelectric Actuation: State of the Art,” *Shock Vib. Dig.*, vol. 33, no. 4, pp. 269–280, Jul. 2001.

[65] *Piezoelectric ceramics : principles and applications*. APC International Ltd., 2011.

[66] R. C. Juvinall and K. M. Marshek, *Fundamentals of Machine Component Design*. Wiley, 2011.

[67] Physik Instrumente (PI) GmbH & Co., *Piezoelectrics in Positioning. Tutorial on Piezotechnology in Nanopositioning Applications Contents Piezoelectrics in Positioning*. 2009.

[68] "BIPM - SI Brochure 8th ed.," 2006. [Online]. Available: http://www.bipm.org/en/publications/si-brochure/. [Accessed: 25-Jan-2015].

[69] L. Kirkup and R. B. Frenkel, *An Introduction to Uncertainty in Measurement: Using the GUM (Guide to the Expression of Uncertainty in Measurement)*. Cambridge University Press, 2006.

[70] D. J. Inman, *Engineering Vibration*, no. October. Prentice Hall, 2001.

[71] T. Irvine, "Bending frequencies of beams, rods, and pipes," *Available on the web on site: http://www. vibrationdata. …*, 2012. [Online]. Available: http://www.vibrationdata.com/tutorials2/beam.pdf.

[72] A. D. Nashif and J. P. Henderson, *Vibration Damping*. John Wiley & Sons, 1985.

[73] W. Benenson and H. Stöcker, *Handbook of Physics*. Springer Science & Business Media, 2002.

[74] S. Bhatawadekar, "Assessment of variability of airway impedance in airway hyperresponsiveness," 2008.

[75] K. N. Desager, M. Cauberghs, and K. P. Van de Woestijne, "Two-point calibration procedure of the forced oscillation technique.," *Med. Biol. Eng. Comput.*, vol. 35, no. 6, pp. 752–6, Nov. 1997.

[76] NEC-TOKIN, *Piezoelectric Ceramics Vol.05*, vol. 05. 2013.

[77] "DLVR Series Low Voltage Digital Pressure Sensors Datasheet." [Online]. Available: http://www.allsensors.com/press-releases/DS-0300_Rev_A13.pdf. [Accessed: 13-Apr-2015].